

**Computational Approaches to Improve Catalyst Design in Nickel-Catalyzed Cross-
Electrophile Coupling**

by

Michelle Elizabeth Akana

A dissertation submitted in partial fulfillment of the
requirements for the degree of

Doctor of Philosophy
(Chemistry)

at the

UNIVERSITY OF WISCONSIN-MADISON

2024

Date of final oral examination: 8/8/2023

The dissertation is approved by the following members of the Final Oral Committee:

Daniel J. Weix, Professor, Organic Chemistry

John F. Berry, Professor, Inorganic Chemistry

Andrew J. Boydston, Professor, Materials Chemistry

Jennifer M. Schomaker, Professor, Organic Chemistry

Dedication

This work is dedicated to everyone along this journey that has believed in me and kept me going. I did not have the strength to do this alone. Also, to those whose unconditional love has kept me moving forward, even when I did not know where forward was.

Table of Contents

Biographical Sketch	vii
Acknowledgements	ix
Abstract	xiii
Contributors and Funding Sources	xv
List of Tables	xvii
List of Figures	xviii
List of Schemes	xx
List of Symbols and Abbreviations	xxi
Chapter 1: An Introduction to Cross-Electrophile Coupling, Molecular Parameterization, and the Prediction of Reaction Outcomes	1
1.1 General Introduction.....	1
1.2 Nickel-Catalyzed Cross-Electrophile Coupling.....	2
1.3 Molecular Parameterization.....	4
1.4 Goals.....	5
Chapter 2: Efforts Toward Predicting Reaction Outcomes with Other Classes of Nitrogenous Ligands	7
2.1 Introduction.....	7
2.1.1 Ligand Selection.....	7

2.1.2	Computational Rationale	8
2.2	Results and Challenges in Data Science	10
2.3	Insights Gained and Improved Project Structure.....	12
2.4	Experimental.....	14
2.4.1	Ligand Key	14
2.4.2	Computational Details	20
Chapter 3: Computational Methods Enable the Prediction of Improved Catalysts for Nickel-Catalyzed Cross-Electrophile Coupling.....		21
3.1	Introduction	22
3.2	Results and Discussion.....	25
3.3	Conclusions.....	34
3.4	Experimental.....	36
3.4.1	General Information	36
3.4.1.1	Reagents	36
3.4.1.2	Methods.....	37
3.4.2	Ligand Key and Preparation of Ligands	39
3.4.2.1	Ligand Key.....	39
3.4.2.2	Preparation of Ligands.....	40
3.4.3	General Procedures.....	50

3.4.3.1	General Procedure A: Evaluation of Ligands in High-Throughput Format	50
3.4.3.2	General Procedure B: Evaluation of Ligands in 1-Dram Vials.....	51
3.4.4	Results of Ligand Screens	53
3.4.4.1	High-Throughput Ligand Screens.....	53
3.4.4.2	Focused Ligand Screens	54
3.4.5	Computational Details	60
3.4.5.1	General Computational Method.....	60
3.4.5.2	Descriptors and Guide to Parameter Spreadsheet	61
3.4.5.3	Threshold Analysis	67
3.4.5.4	Parameterization Modeling Overview	71
3.4.5.5	Univariate Correlations and Models Using High-Throughput Experimental Results.....	73
3.4.5.6	Univariate Correlations and Models Using the Focused Ligand Experimental Results.....	75
3.4.5.7	Alternative Models Using Free Ligand Parameters.....	79
 Chapter 4: Insight into the Relationship Between the Structure of Common L2 Dinitrogen Ligands and Selectivity in Cross-Electrophile Coupling.....		
4.1	Introduction	81
4.2	Results and Discussion.....	82

4.2.1	Phenanthroline (phen) Ligands	82
4.2.2	Pyridyl Carboxamidine (PyCam) Ligands.....	85
4.2.3	Pyridyl Oxazoline (PyOx) Ligands.....	87
4.2.4	Bioxazoline (BiOx) Ligands	89
4.2.5	Bisoxazoline (BOX) Ligands	90
4.3	Experimental.....	93
4.3.1	General Information, Procedure, and Computational Details	93
4.3.2	Ligand Key and Results of Ligand Screens.....	93
4.3.3	Results of Statistical Analysis.....	98
Chapter 5: Miscellaneous Computational Efforts		99
5.1	Identification of 2'2'-Bipyridine-6-Carbonitrile and Initial Efforts to Rationalize Their Experimental Outcomes	99
5.1.1	Introduction	99
5.1.2	Results and Discussion.....	99
5.1.3	Experimental.....	106
5.1.3.1	General Information	106
5.1.3.1.1	Reagents	106
5.1.3.1.2	Methods.....	107

5.1.3.1.3	General Procedure C: Evaluation of Ligands in 1-Dram Vials	108
5.1.3.2	Ligand Key and Preparation	110
5.1.3.2.1	Ligand Key	110
5.1.3.2.2	Preparation of Ligands	110
5.1.3.3	Results of Ligand Screens	117
5.1.3.4	General Computational Method	117
5.1.3.5	Computational Results	117
5.2	Initial Studies on the Impact of Ligand Structure in Decarbonylative Cross-Electrophile Coupling	118
5.2.1	Introduction	118
5.2.2	Results	118
5.2.3	Discussion and Future Work	120
5.2.4	Experimental	121
5.2.4.1	General Computational Method	121
	References	122

Biographical Sketch

Michelle E. Akana was born in 1995 and raised in San Antonio, Texas, where she later graduated from Communications Arts High School in 2013 and enrolled at St. Mary's University. There, she received a Bachelor of Science in Chemistry and a Bachelor of Arts in Mathematics in 2017, graduating cum laude with honors, and was a Welch Summer Research Fellow (2014), a MARC U*STAR Trainee (2015-2017), and a Presidential Award recipient (2017). During her undergraduate career, Michelle engaged in research across many of the chemical disciplines. She gained experience in catalysis and an interest in pursuing research with Professor Jeff R. Schoonover, where she studied the reactivity of copper–vanadium oxides as catalysts for organic dye degradation from 2014–2015. In the years that followed, she also participated in the research of colloidal materials, proteins, and organocatalysis. She conducted research with Professor Susan P. Oxley in 2017, contributing to the development of a photographic water analysis method to detect and quantitate cationic metals. In her spare time, Michelle had the privilege to serve as an organizer and demonstration leader for the biannual Fiesta of Physics and Environmental Science Extravaganza, a STEM outreach event open to elementary students in the surrounding school districts, which provides undergraduate students the opportunity to engage with the local community and hone their science communication skills. Coordinating these outreach events inspired Michelle to consider how to make scientific environments more welcoming of individuals and how to transfer scientific techniques across disciplines during her future studies.

Michelle began her graduate studies in Chemistry in 2017 at the University of Wisconsin-Madison shortly after graduating from St. Mary's University. She joined the laboratory of Professor Daniel J. Weix that fall, where she had the opportunity to develop

cross-electrophile coupling methods from the bench, but found that her interests lay more behind-the-scenes in data mining and the application of data science techniques to refine cross-electrophile coupling methods. During her time in Madison, Michelle worked to improve the social and emotional climate of the Department of Chemistry as a member of the Climate Survey team, whose data-driven efforts were crucial in shaping discussions of mental health and how the body of graduate students and postdoctoral fellows could be best supported. Michelle was the recipient of the PPG Summer Fellowship in 2021 in recognition of her research efforts and received her Master of Science degree in 2022. The following publications were a result of work conducted during her doctoral study:

1. Akana, M. E.; Tcyrulnikov, S.; Akana-Schneider, B. D.; Reyes, G. P.; Monfette, S.; Sigman, M. S.; Hansen, E. C.; Weix, D. J. "Computational Methods Enable the Prediction of Improved Catalysts for Nickel-Catalyzed Cross-Electrophile Coupling" *J. Am. Chem. Soc.* **2023**. DOI: 10.1021/jacs.3c09554.

Acknowledgements

During my time as a PhD student, I have been fortunate to meet, work, and collaborate with many people, for whose support I would like to express my gratitude.

I would first like to thank my advisor, Professor Daniel J. Weix, for molding my growth as a scientist and as an individual throughout my entire graduate school career: you pushed me to think critically and efficiently. You offered reassurance when I felt insecure transitioning from bench chemistry to data science and computational chemistry during my second year, have continued to assure me that I am a competent scientist, and challenged me to harness my full potential. Thank you for providing me with an opportunity to direct my skills in applied math, navigating with me the learning and hiccups of being a full-time computational chemist, and giving me guidance in these early years of my professional career.

To all the past and present members of the Weix group—thank you for challenging me and asking the hard questions that helped me grow as a scientist and as a member of this team. Thank you to Dr. Keywan Johnson for teaching me that doing the correct experiments is far more important than doing a lot of experiments. Thank you to Dr. Michael Gilbert for teaching me how to synthesize organometallic complexes and for our discussions about mechanistic ideas and helping me synthesize my ideas into cohesive narratives. I enjoyed game nights that Keywan, Dr. Kevin Garcia, and Daniel Enny hosted, as well as our various dinner get-togethers.

When I shifted course my second year, I had no experience as a computational chemist nor as a data scientist. I am the scientist I am because of Professor Matthew Sigman and the Sigman group. Matt, thank you for taking me under your wing. Although

I wasn't formally a member of your research group, you allowed me to join your subgroup meetings, where I learned how to communicate data science findings to other chemists, see where the current borders of our field lie, and see your group members continually expand the applications of data science in chemistry. I am grateful that you made time to mentor me and make sure my research projects ran smoothly. I would also like to thank Dr. Tobias Gensch, for the many hours of conversation we've had about computational chemistry and project design; I look to you as a role model and as an inspiration of how to think big when looking for problems to solve.

To all my teachers and professors through the years, thank you for recognizing my potential. In particular, I would like to thank Professors Dmitriy Khon and Ahmad Galaleldeen for mentoring me throughout my time at St. Mary's University. Ahmad, you taught me to set higher expectations for myself academically, and that changed the rest of my experience at St. Mary's. Dmitriy, thank you for tolerating me for that year and half that I struggled through your organic chemistry classes, giving me stern talks to reorient my growth as a student, and your persistent but patient pushes that convinced me to leave the safety of home, my family, and San Antonio, to see what adventures graduate school would hold for me.

I am indebted to my friends—especially Haley Spencer, Kimberly DeGlopper, Qi (Yukki) Li, Dr. Seoyoung Kim, Dr. Logan Vine, Samuel and Ellorah Wood, Dr. Nathan Loud, Dr. Daniel Salgueiro, and Dr. Jonas Widness—who have taught me that there is always time for humor, coffee, and friendship in the best and worst of times. I am grateful that our friendships have persisted whether we are down the road from each other or across the country. Your friendship is invaluable to me.

Finally, I would not have been able to complete my educational journey without my family, who have shaped my development and surrounded me with love since the beginning. To my parents, Marinella and Daniel Akana; thank you for believing in me. Your strength is what carries me when I have none. My father, in particular, is responsible for cultivating my curiosity in the sciences and for setting me on this trajectory—I would not be a scientist now without his influence. My mother ensured I was engaged with all my academic subjects, even sacrificing her time to serve as my sole educator for a time; she also helped nurture my creative interests to allow the scientist side of my brain to rest by taking on “sanity projects”.

In particular, I would like to thank my immediate family, Anthony, Alan and Darlene Akana, Ethan Schneider and Johnathan Hart, as well as Romeo and Kathleen Agtuca, for your confidence and unwavering support throughout this journey. I carry your love with me; wherever I go, I know you all will journey with me in spirit.

To my brother, Gabriel Agtuca: I am so grateful to have you in my life. While we may not share biological parents, having the privilege to be considered your sister makes our bond so much more special and precious to me. I am honored that you have chosen to be a fixture in my life, and I am grateful to know that you will continue to be there as we both keep growing and changing.

Para kenka a napateg a lolak, Marina Agtuca. Agyamanak iti Apo Dios ta intalekmo ti biag ken aldawmo kenkuana. Inikkan naka iti tured, pigsa ti pakinakem ken gundaway a nakaumay ditoy Estados Unidos. Naparaburanka iti nabuslon a bendisyon ket adu ti nairaman nangruna kadagiti annak ken appokom. Gapu kenka, naikkannak ti wayak a nakaadal ken nakaturpos iti napilik ken kinalikagumak a kurso. Kayatko koma a tuladen ken maaddaan iti kababalin a kas kenka; nagaget ken naanus uray no aniaman

a tuok wenno rigat ti biag a sumangbay. Sapay ta aramaten iti Apo Dios toy biagko ta maipagpanakkel nak, naregta a makatulong ken makaparegta iti adu ken sabsabali a tattao.

Finally, I would like to thank my partner, Brett Akana. Brett, you have been my lab mate through the years, but you were first and have always been my friend as we navigated our years of schooling. Knowing you are always by my side has enabled me to navigate smoothly through the rough waters, changes, and growth life has brought us this past decade, and I would not have been able to accomplish this endeavor without your support. You are my constant safe place.

Abstract

This dissertation will discuss advancements made toward understanding the intrinsic reactivity of nitrogenous ligands in nickel-catalyzed cross-electrophile coupling, as well as their impacts on reaction selectivities.

Chapter 1 will introduce cross-electrophile coupling, highlight the importance of ligands in promoting diverse elementary steps, and discuss strategies to search for, understand, and improve ligand architecture.

Chapter 2 describes our initial investigation utilizing descriptors from a diverse set of ligands and ligand-like molecules to predict reaction yield and selectivity. This investigation provided critical insight into experimental design, construction of a training set, and determining project outcomes. The results of these efforts informed our studies that are detailed in successive chapters.

Chapter 3 summarizes the application of statistical methods to develop a model for selectivity in bipyridine-nickel-catalyzed cross-electrophile coupling. The resulting model was used to rationalize experimental outcomes, develop mechanistic insight, and design improved ligands in silico.

Chapter 4 summarizes initial insights into the relationships between the structure of other classes of heterocycle-based L2 dinitrogen ligands and their corresponding experimental outcomes. These investigations provide a basis for understanding the performance of these ligands and expands on the insights described in Chapter 3. A plan for ongoing research informed by these results is proposed.

Chapter 5 describes additional computationally informed projects that were undertaken by the author. These projects utilize computed catalyst structures and

energies to rationalize the impact of ligand binding on the reactivity of novel 2,2'-bipyridine-6-carbonitrile ligands, as well as the relationship of ligand structure to selectivity in decarbonylative cross-electrophile coupling.

Contributors and Funding Sources

The author's thesis committee included Professors Daniel J. Weix, John F. Berry, Andrew J. Boydston, and Jennifer M. Schomaker from the University of Wisconsin-Madison Department of Chemistry. The author is responsible for all experimental procedures in this thesis unless specified below:

Dr. Sergei Tcyrulnikov and Giselle P. Reyes are responsible for the HTE setup, refinement, and collection of all initial high-throughput datasets whilst working under the direction of Dr. Eric C. Hansen, Dr. Sebastien Monfette, Dr. Thomas Knauber, Prof. Daniel J. Weix, and the author.

The members of the Sigman group, and in particular Prof. Matthew S. Sigman and Dr. Tobias Gensch, are responsible for shaping the author's perspectives as a computational chemist and data scientist. They are responsible for the development and provision of the scripts utilized for parameter collection and statistical analysis. While these scripts are not publicly available, molecular descriptors may be gathered directly from computational output files and statistical analysis can be performed via a variety of tools, (e.g., MATLAB, GNU Octave, Python packages for statistical analysis, R, and Excel).

Chapter 3: Brett D. Akana-Schneider is responsible for the synthesis of the non-symmetric bipyridine suite, generation of the focused screening dataset, and provided design input during the author's production of tables and figures.

Chapter 4: Prof. Daniel J. Weix provided guidance in the author's initial efforts and the overall trajectory of this work.

Chapter 5: The generation of hypotheses, design of follow-up experiments, and discussion of findings in Section 5.1 was a collaborative effort with Brett D. Akana-Schneider, who is also responsible for the synthesis of the 2,2'-bipyridine-6-carbonitrile ligand suite and generation of the corresponding experimental dataset. The development of decarbonylative alkylation of alkyl halides was conducted by Dr. Zhidao Huang. All computational efforts were performed by the author.

The author was funded by the National Science Foundation (CHE-1900366 to Daniel J. Weix), the University of Wisconsin-Madison (PPG fellowship to the author), and Pfizer.

NMR and high resolution mass spectrometry results included in this report were recorded at the Paul Bender Chemistry Instrumentation Center, a University of Wisconsin-Madison Department of Chemistry facility. NMR instruments were purchased with the support of the National Science Foundation (CHE-1048642) and a generous gift by Paul J. and Margaret M. Bender. Funds for the high resolution mass spectrometer were obtained from the National Institutes of Health award 1S10OD020022. The calculations used for modeling were performed using computational resources managed and supported by the University of Wisconsin-Madison Department of Chemistry Phoenix cluster and the National Science Foundation award CHE-0840494

List of Tables

Table 3.1 Ligands Designed in Silico Outperform State-of-the-art Bipyridines	31
Table 3.2 Benchmarking of Improved Bipyridines in the XEC of Aryl Halides	32
Table 3.3 NMe ₂ bpy Enables the Coupling of Alkyl Chlorides	32
Table 3.4 NMe ₂ bpy Increases the Efficiency of Existing Coupling and Unlocks New Substrate Pairings	33
Table 4.1 A Comparison of phens: Similar Electronics Yet Different Results	83
Table 4.2 General Electronic Trends Translate from bpy Ligands, but Reactive Functionalities Confound Analysis	84
Table 4.3 Observed Univariate Correlations for PyCam Ligands	85
Table 4.4 N-cyanated PyCams Provide Lower Yield	86
Table 4.5 Observed Univariate Correlations for PyOx Ligands	87
Table 4.6 Observed Univariate Correlations for BiOx Ligands	89
Table 4.7 Observed Univariate Correlations for BOX Ligands	91
Table 5.1 Initial Observations from High-Throughput Screening Dataset: 6-Cyanation Alters Reactivity of Analogous Ligands	100
Table 5.2 A Evaluation of bpy ^{CN} Ligands Reveals a Reversed Trend for Selectivity and Reactivity	101
Table 5.3 bpy ^{CN} Ligands Possess Unique Reactivity	103

List of Figures

Figure 2.1 Ligands and Ligand-Like Molecules from Initial Ligand Library	15
Figure 3.1 Bipyridine Ligand Key	39
Figure 3.2 Results of High Throughput Ligand Screening	53
Figure 3.3 Correlation Between Concentration of 3.3 and 3.4	53
Figure 3.4 Performance of the Training and Validation Set in the Model Reaction.....	54
Figure 3.5 Effects of Stirring and TFA Addition.....	55
Figure 3.6 Benchmarking of Improved Bipyridines in the Coupling of Aryl Halides with Alkyl Bromides.....	56
Figure 3.7 Decreasing Catalyst Loading Increases Selectivity	56
Figure 3.8 Coupling of Aryl and Alkyl Chlorides.....	58
Figure 3.9 Coupling of <i>N</i> -Alkyl 2,4,6-Triphenylpyridinium Salts with Aryl Halides.....	59
Figure 3.10 Atom Numbering Scheme for Free Ligand, (L)Ni(Ph)Br Square Planar, and (L)Ni(Ph)Br Tetrahedral DFT-Optimized Structures.....	62
Figure 3.11 Guide to Parameter Spreadsheet.....	62
Figure 3.12 Confusion Matrix Definitions	68
Figure 3.13 Threshold Analysis with Only Bipyridine-Based Ligands.....	68
Figure 3.14 Threshold Analysis with Full HTE Dataset.....	69
Figure 3.15 Threshold ΔE Decision Value and Statistical Accuracy Metrics	70
Figure 3.16 Univariate Correlations from High-Throughput Screening Results	73
Figure 3.17 Collinearity Heatmap of All Univariate Correlations from High-Throughput Screening Results	73
Figure 3.18 Best 1-Parameter Model (μ) from High-Throughput Screening Results	75
Figure 3.19 Univariate Correlations from Focused Screening Results.....	76

Figure 3.20 Best 1-Parameter Models from Focused Screening Results	77
Figure 3.21 1-Parameter Model (μ) Using Focused Screening Results	78
Figure 3.22 Predicted Selectivity of In Silico Ligands Utilizing Optimal Model with NPA _{Cipso}	79
Figure 3.23 Comparison of Univariate Correlations with Parameters from Unbound Ligand Descriptors.....	80
Figure 4.1 phen Ligand Key	93
Figure 4.2 Results with phen Ligands.....	94
Figure 4.3 PyCam Ligand Key	94
Figure 4.4 Results with PyCam Ligands.....	95
Figure 4.5 PyOx Ligand Key	95
Figure 4.6 Results with PyOx Ligands.....	96
Figure 4.7 BiOx Ligand Key.....	96
Figure 4.8 Results with BiOx Ligands.....	96
Figure 4.9 BOX Ligand Key	97
Figure 4.10 Results with BOX Ligands	97
Figure 4.11 Threshold Analysis of phen Ligands.....	98
Figure 5.1 Ligand Key	110
Figure 5.2 Evaluation of bpy, bpy ^{CN} , and tpy Ligands.....	117

List of Schemes

Scheme 2.1 Initial Ligand Library Contained a Diverse Set of L2, LX, and L3 Ligands....	7
Scheme 2.2 Comparison of Proposed Computational Model Species	8
Scheme 2.3 Geometric Considerations of Computed (L)Ni ^{II} (Ph)Br Structures ^a	10
Scheme 2.4 Obstacles of Our Initial Project Design	10
Scheme 2.5 Improved Project Structure.....	12
Scheme 3.1 Bipyridines Enable Diverse Reactivity	22
Scheme 3.2 Model Reaction and Initial Data Processing Efforts.....	25
Scheme 3.3 Collinear Variables Decrease Specificity	28
Scheme 3.4 A Tailored Dataset Enables a More Robust Model	29
Scheme 4.1 Threshold Analysis of phen Ligands Reveals a Reactivity Cliff for Steric Hindrance.....	82
Scheme 4.2 Proposed Modifications of PyOx Ligands.....	88
Scheme 4.3 Threshold Analysis of BOX Ligands from the Weighted Average of Tetrahedral and Square Planar (.boltz) Parameter Sets.....	90
Scheme 4.4 Threshold Analysis of BOX Ligands from the Square Planar (.sqpl) Parameter Set	91
Scheme 4.5 Collinearity of NMR(δ_{zz}) _{N4} with %V _{bur} , 2.0 Å	92
Scheme 5.1 Electronic Trends for bpy and bpy ^{CN} Ligands	102
Scheme 5.2 Initial Computational Studies Suggest Flexibility in Denticity	104
Scheme 5.3 Computed Structures to Investigate Possible Binding Modes of 5.L4	105
Scheme 5.4 Initial DFT Studies of Decarbonylation Equilibria	120

List of Symbols and Abbreviations

-	minus, negative, or hyphen
:	ratio
	weighted average of parameter from tetrahedral and square planar
.boltz	dataset
.free	parameter from free ligand, unbound to any metal
.lowestgeo	parameter from either the square planar or tetrahedral dataset,
m	whichever isomer is lower in energy
.sqpl	parameter from square planar dataset
.tet	parameter from tetrahedral dataset
·	radical
[]	concentration
%	percent
%V _{bur}	percent buried volume
‡	transition state
°	degrees
°C	degrees Celsius
+	plus or positive
~	about or approximately

∠	angle
≤	less than or equal to
¹³ C	carbon-13
¹³ C{ ¹ H}	proton decoupled carbon-13
¹⁹ F	fluorine-19
¹ H	hydrogen-1
Å	Angstrom(s)
Ac	acetate
ACS	American Chemical Society
Alk	alkyl
Ar	aryl
Ar-Alk	cross-product
Ar-Ar	biaryl
BiIm	1 <i>H</i> ,1' <i>H</i> -2,2'-biimidazole (or derivative thereof)
BiOx	2,2'-bis(2-oxazoline) (or derivative thereof)
Bn	benzyl
BOX	bis(4,5-dihydrooxazol-2-yl)methane (or derivative thereof)
bp	boiling point

bpp	2,6-bis(pyrazol-1-yl)pyridine (or derivative thereof)
bpy	2,2'-bipyridine (or derivative thereof)
bpyCam	2,2'-bipyridine-6-carboxamide (or derivative thereof)
bpy ^{CN}	2,2'-bipyridine-6-carbonitrile (or derivative thereof)
Br	bromine
Br ₂	bromine ligand of the computed (L)Ni ^{II} (Ph)Br complex
C	carbon or Celsius
C(sp ²)	sp ² -hybridized carbon
C(sp ³)	sp ³ -hybridized carbon
calcd	calculated
CDCl ₃	chloroform-d
C _{ipso}	<i>ipso</i> carbon of phenyl ligand of the computed (L)Ni ^{II} (Ph)Br complex
Cl	chlorine
cm	centimeter
CN	nitrile or cyano
CO ₂ Et	carboxyethyl
cod	1,5-cyclooctadiene
CV	column volume(s) or cyclic voltammetry

Cy	cyclohexyl
d	d-orbital
d	derivative or change
DCM	dichloromethane
DFT	density functional theory
DI	deionized
DIPEA	<i>N,N</i> -diisopropylethylamine
DMA	<i>N,N</i> -dimethylacetamide
dme	dimethoxyethane
DMF	<i>N,N</i> -dimethylformamide
DMSO	dimethyl sulfoxide
DOI	digital object identifier
dt	derivative or change in time
E	energy
E	times ten, raised to the power of the number that immediately follows
EDTA	ethylenediaminetetraacetic acid
equiv	equivalent(s)
ESI	electrospray ionization

Et	ethyl
EtOAc	ethyl acetate
EtOH	ethanol
F	fluorine
F1	F1 score
FID	flame ionization detection
FN	false negative
FP	false positive
G	Gibbs free energy
g	gram(s)
GC	gas chromatography
GCMS	gas chromatography-mass spectrometry
GH	Any group or hydrogen
h	hour(s)
H	hydrogen or proton
<i>H</i>	substituted position on hydrogen
Hg	mercury
HOMO	highest occupied molecular orbital

HRMS	high-resolution mass spectrometry
HTE	high-throughput experimentation
Hz	hertz
I	iodine
<i>i</i> -Pr	isopropyl
	[3aR-[2(3'aR*,8'aS*),3'aβ,8'aβ]]-(+)-2,2'-Methylenebis[3a,8a-dihydro-8H-
IndaBox	indeno[1,2-d]oxazole]
iPrOH	isopropanol
<i>J</i>	coupling constant
<i>J. Am. Chem.</i>	
<i>Soc.</i>	Journal of the American Chemical Society
K	Kelvin
k ₅ -fold	five folds of k-fold cross-validation
kcal	kilocalorie(s)
L	ligand
L2	bidentate L-type ligand
L3	tridentate L-type ligand
LFER	linear free energy relationship
Li	lithium

LOO	leave-one-out cross-validation
LUMO	lowest unoccupied molecular orbital
LX	bidentate LX type ligand
M	molar (mol/L) or metal
m	meter(s)
m/z	mass-to-charge ratio
M ⁺	mass peak from organic cation in GCMS
MAE	mean absolute error
MARC	Maximizing Access to Research Careers
MCC	Matthews correlation coefficient
Me	methyl
MeCN	acetonitrile
MeOH	methanol
Mg	magnesium
mg	milligram(s)
MHz	megahertz
min	minute(s)
mL	mililiter(s)

mM	millimolar
mm	millimeter(s)
mmol	millimole
Mn	manganese
mol	mole
MS	mass spectrometry
N	nitrogen
<i>N</i>	substituted position on nitrogen
N(Me) ₂	dimethylamino
N3	donor nitrogen of ligand trans to C _{ipso} of the computed (L)Ni ^{II} (Ph)Br complex
N4	donor nitrogen of ligand trans to Br ₂ of the computed (L)Ni ^{II} (Ph)Br complex
Na	sodium
NEt ₂	diethylamino
Ni	nickel
nm	nanometer(s)
NMe ₂ bpy	4,4'-bis(dimethylamino)-2,2'-bipyridine
NMP	<i>N</i> -methyl-2-pyrrolidone or 1-methyl-2-pyrrolidone

NMR	nuclear magnetic resonance
NPA	Natural Population Analysis
NSF	National Science Foundation
O	oxygen
O	substituted position on oxygen
OEt	ethoxy
OLEDs	organic light-emitting diodes
OMe	methoxy
p	p-orbital
P	phosphorous
pbpy	6-(1 <i>H</i> -pyrazol-1-yl)-2,2'-bipyridine (or derivative thereof)
Pd	palladium
Ph	phenyl
phen	1,10-phenanthroline (or derivative thereof)
ppm	part(s) per million
Pr	propyl
${}_{\text{pred}}R^2$	predicted R^2
${}_{\text{pred}}R^2$	predicted R^2

psi	pounds per square inch
PTFE	polytetrafluoroethylene
PyBCam	pyridine-2,6-bis(carboximidamide) (or derivative thereof)
PyCam	pyridine-2-carboximidamide (or derivative thereof)
PyOx	2-(3-pyridyl)-2-oxazoline (or derivative thereof)
Q ²	R ² for leave-one-out cross-validation
QuinOx	2-(4,5-dihydro-2-oxazolyl)quinoline (or derivative thereof)
R	organic substructure or gas constant
R ²	coefficient of determination
Rev	revision
R _f	retention factor
rpm	revolutions per minute
rt	room temperature (~25 °C)
s	s-orbital
S	sulfur or multiplicity
S	substituted position on sulfur
SET	single-electron transfer
SMD	solvation model based on density

SP	single point
STEM	Science, Technology, Engineering and Mathematics
T	temperature
<i>t</i>	<i>tert</i> or tertiary
<i>t</i> -Bu	<i>tert</i> -butyl
TFA	trifluoroacetic acid
TLC	thin layer chromatography
TMS	tetramethylsilane
TMS	tetramethylsilane
TMU	<i>N,N,N',N'</i> -tetramethylurea
TN	true negative
TP	true positive
tpy	2,2';6',2''-terpyridine (or derivative thereof)
U*STAR	Undergraduate Student Training in Academic Research
UPLC	ultra performance liquid chromatography
UV	ultraviolet
V_{bur}	buried volume
wt%	weight percent

X	halide, pseudohalide, or numerical variable
x	times or descriptor variable
x	variable
XC	cross-coupling
XEC	cross-electrophile coupling
Y	numerical variable
y	variable
Zn	zinc
β	beta
δ	delta or chemical shift
Δ	delta or difference
ΔE	difference in energies
$\Delta\Delta G^\ddagger$	difference in transition state energies
η	eta or chemical hardness
μ	mu, micro, or chemical potential
μL	microliter(s)
μm	micrometer(s)
μmol	micromole(s)

π	pi
ρ	rho
σ	sigma or Hammett parameter
σ^m	Hammett parameter for <i>meta</i> substituents
σ^p	Hammett parameter for <i>para</i> substituents
ω	omega

Chapter 1: An Introduction to Cross-Electrophile Coupling, Molecular Parameterization, and the Prediction of Reaction Outcomes

1.1 General Introduction

Nickel catalysis has emerged as a critical tool in modern synthetic organic chemistry. The suite of diverse single- and two-electron elementary steps promoted by nickel catalysts—in combination with ready tuning of reactivity—enables the substitution of nickel catalysts for precious metals and the development of novel methods.¹ This diversity in reactivity is often controlled via the use of different classes of supporting ligands. Differences in donor atom, hybridization, charge, and denticity each drive the modulation of energies encompassing the various accessible oxidation states and geometries of the nickel center. These trends—which are often distinct from other transition metals—necessitate a diverse selection of supporting ligands and an equally diverse mechanistic understanding to determine their selection and design. While advances in mechanistic understanding have enabled improved initial selection of a ligand based on general classification, rapid selection of an optimal ligand remains challenging. This thesis describes the application of statistical methods to relate computationally derived molecular descriptors to reaction outcomes to facilitate improvements in selection and design of ligands for nickel catalysis. These efforts have enabled the *in silico* design of bipyridine ligands for nickel-catalyzed cross-electrophile coupling and provided key initial insights into the performance of related heterocycle-based L2 dinitrogen ligands.

1.2 Nickel-Catalyzed Cross-Electrophile Coupling

Nickel-catalyzed cross-electrophile coupling (XEC) is a useful method for the introduction of C(sp³) character into functionalized small molecules. Enabled by a mixture of single- and two-electron steps, a single catalyst can selectively activate two electrophilic coupling partners. The result, a cross-coupling that avoids carbon nucleophiles, enables more rapid and functional-group tolerant combinatorial synthesis. In particular, C(sp²)–C(sp³) XEC between aryl and alkyl electrophiles has risen as an attractive alternative to redox-neutral cross-couplings due to its avoidance of issues concerning: (1) the rate of oxidative addition of alkyl halides to low-valent palladium, (2) the low availability and stability of alkylmetal reagents, and (3) the prevalence of β-hydride elimination from alkylpalladium complexes.²⁻⁴ These advantages have driven advances in scope to allow for the coupling of a variety of aryl (pseudo)halides with diverse alkyl radical precursors.⁵

Despite advances in scope, the identification and development of new nitrogen-based ligands for XEC is lagging relative to the diverse phosphorus-based ligands also used in XEC. As a result, prominent ligand architectures remain key features of almost all XEC reactions. Heterocycle-based L2 dinitrogen ligands such as 2,2'-bipyridines (bpy)^A—and related phenanthrolines (phen)^B—are the most common ligands employed in the XEC of aryl and alkyl electrophiles. Common mechanistic proposals suggest that bipyridine-nickel catalysts promote an aryl-first coupling in which rate-limiting alkyl

^A The abbreviation “bpy” can be used to refer either to 2,2'-bipyridine itself or other related molecules that build upon the 2,2'-bipyridine framework with substitution at one or more of the 3-, 3'-, 4-, 4'-, 5-, 5'-, 6-, or 6'-positions.

^B The abbreviation “phen” can be used to refer either to 1,10-phenanthroline itself or other related molecules that build upon the 1,10-phenanthroline framework with substitution at one or more of the 2-, 3-, 4-, 5-, 6-, 7-, 8-, or 9-positions.

radical capture and reductive elimination determines selectivity for the desired product versus the aryl homodimer.^{3,6,7} While occasionally used in XEC reactions, and particularly in the alkylation of alkyl and acyl electrophiles,⁸⁻¹⁰ higher dentate terpyridines (tpys) and related ligands—such as 2,6-bis(pyrazol-1-yl)pyridine (bpp)—are most often employed in redox-neutral cross-couplings.¹¹⁻¹³ These two classes of L2 and L3 *N*-heterocyclic ligands provide an implicit standard of reactivity by which new ligands are compared.

The discovery of improved ligands can have a substantial impact on the utility, selectivity, and translatability of cross-coupling reactions. Our group undertook a high-throughput campaign in collaboration with Pfizer to mine their heteroatom-rich compound library for new ligand classes.¹⁴ The result was the discovery of carboxamidine-based ligands—PyCam, PyBCam, and bpyCam—that enable improved experimental outcomes in many cases compared to traditional bpy, phen, and tpy ligands. In particular, these ligands have been used to couple complex *N*-heterocyclic substrates that perform poorly with bpy, phen, and tpy derivatives.¹⁴⁻¹⁸ The improved reactivity of these ligands also unlocked selective XEC of unactivated alkyl and aryl chlorides. While these ligands greatly expanded the accessible scope of XEC, a concomitant increase in mechanistic understanding and binding insight was not gained. Initial investigations show that while their reactivity often mirrors that of related bpy and tpy derivatives, the binding of pyridine carboxamidines—and particularly their *N*-cyano derivatives—is not equivalent.^{13,17} In order to better design, validate, and rationalize the reactivity of ligands for nickel catalysis, a better understanding is needed of the relationship between critical molecular features and reactivity.

1.3 Molecular Parameterization

While fragment-based molecular parameterization has been a mainstay in organic mechanistic investigations since the pioneering work of Hammett and others,¹⁹⁻²⁶ adoption to metal catalysis was slower. Work by Tolman enabled an initial understanding into the steric and electronic properties of phosphines.²⁷ Despite these advances, direct application of these parameters often lacks sufficient nuance to capture the dynamic nature of ligand binding, leading to incorrect reaction predictions. Further, such tabulated features are not common for nitrogen donors, leading to a gap in usable information, which limits the rationalization and prediction of new nitrogenous ligands.

DFT-derived molecular descriptors offer a unique, focused insight into the electronic and steric environment of well-defined molecular catalysts, and have accelerated the acquisition, specificity, and accuracy of parameters. The correlation of these descriptors to reaction outcomes enables the incorporation of nuance that is often lost using fragment-based, tabulated features, or even large scale DFT-derived features such as solid angle. As a result of this nuance, the resulting models often provide superior robustness and predictivity. The application of these correlation methods has enabled the accelerated understanding, development, and commercialization of diverse phosphines,^{28,29} leading to wide developmental gap compared to *N*-heterocycle-based ligands. For example, the Doyle group utilized multivariate linear regression to develop improved “DinoPhos” ligands for nickel catalysis that enable improved reactivity based on large distal sterics while maintaining efficient bis-ligation.^{30,31} Further, work from the Sigman and Aspuru-Guzik labs has made a large-scale library of DFT and machine-learning derived molecular features readily available for a large number of monophosphine ligands.^{32,33} While some descriptors for nitrogenous ligands have been

published, they are limited in their scope and depth.³⁴⁻³⁷ No such parameterization for bipyridines exists.

Despite the lack of a large-scale library, the application of statistical methods to inform catalyst design for L2 dinitrogen ligands in d^{10} metal catalysis has seen some success. For example, the Sigman lab has published extensive work on the correlation of ligand molecular features to enantioselectivity in PyOx-catalyzed Heck reactions.^c Further work by the Doyle lab has utilized steric and electronic descriptors to rationalize the improved performance of bisimidazoline (BiIm) ligands in comparison to related BiOx ligands.^{36,37} While these and other studies have offered insight into their unique reaction systems, their results are often only utilized to rationalize enantioselectivity or the rates of individual mechanistic steps.³⁸ Thus far, no publications have offered a general model for selectivity in nickel catalysis, nor the ability to predict the reactivity of ligand classes not present in the training set. As such, *in silico* ligand evaluation remains elusive. As a result, limited modification of existing ligand structures or material and time intensive HTE campaigns remain the state of the art in ligand development.

1.4 Goals

The goal of this work was the generation of a general model of selectivity in nickel-catalyzed cross-electrophile coupling. We sought to correlate DFT-derived molecular descriptors with a set of reaction outcomes from diverse ligands to understand the key molecular features that govern selectivity for the cross-coupled product over the two possible homodimeric products. The datasets utilized in this thesis incorporate variations

^c While this system utilizes a (PyOx)Pd catalyst and the authors considered molecular descriptors derived from palladium complexes, the computational dataset they generated for the unbound PyOx ligands is transferable to studies of systems catalyzed by other transition metals.

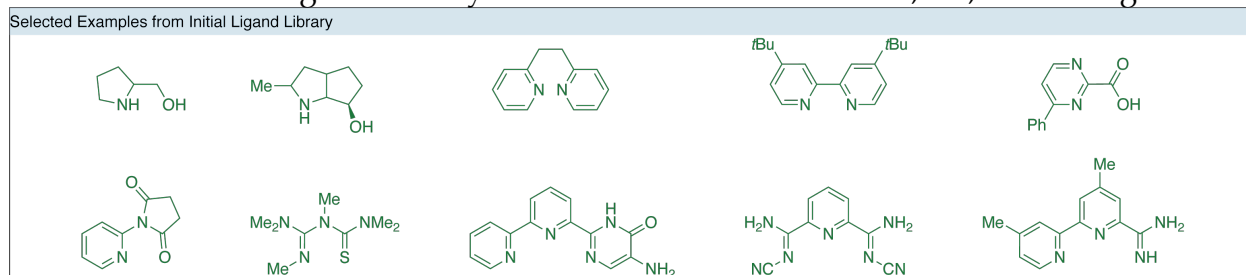
on privileged ligand classes, as well as new, untested heteroatom donors. We attempted to generate a general model that spanned multiple classes of ligands. The insight provided by such a model would enable the rapid testing of hypotheses in silico—promoting more efficient, informed ligand design in order to: (1) improve on existing classes of ligands, and (2) identify new structures that offer similar reactivity based on a conserved mechanism. Further, having a general model allows for the rapid identification of outliers, which can be further investigated experimentally and computationally to rationalize their behavior in the model reactions. A final goal was to develop a computational dataset that would be translatable to a variety of nickel-catalyzed processes, enabling more accessible statistical analyses of reaction outcomes in the future.

Chapter 2: Efforts Toward Predicting Reaction Outcomes with Other Classes of Nitrogenous Ligands

2.1 Introduction

2.1.1 Ligand Selection

Scheme 2.1 Initial Ligand Library Contained a Diverse Set of L2, LX, and L3 Ligands

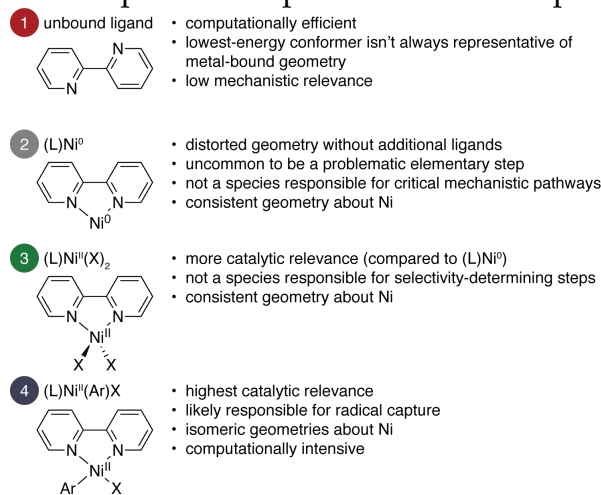


When designing an initial training set for correlations with experimental outcomes, it was unclear the extent to which observed trends would translate between molecules with different denticity, donor atoms, and hybridization. We took inspiration from existing classes of ligands and successful differentiation of reactivity to determine the classes of compounds to include (Scheme 2.1). Mixed donor-pincer ligands are common in redox-neutral cross coupling.³⁹ These ligands, along with the success of non-symmetric donor ligands such as carboxamidate-based ligands and *bpp*,^{14,18} led us to include a variety of non-symmetric donors, including mixed *N*-, *S*-, and *O*-donors. Recent work by Baran, Molander, and others have demonstrated the utility of LX donor ligands in nickel catalysis.^{40–43} These reports inspired the inclusion of LX donors based on carboxylates, thiolates, and phenoxides. Finally, conserved reactivity is often observed between ligands of different denticity.^{17,44,45} For example, both mono- and bis-ligated phosphine metal catalysts are common in redox-neutral cross coupling. Further, canonical L2 and putative L3 ligands—*bpy* and *PyBCam*—can be used in the same cross-

coupling with similar yield and distribution of side products.¹⁴ As such, we included L2 and L3 ligands, as well as compounds that may display dynamic binding modes. Given the overarching goals of the study—to gain insight into the general features of successful catalysts, classify ligands based on DFT-derived features, and generate a general model for selectivity and reactivity in XEC—we felt that this diverse dataset offered an ideal opportunity to gain top-down insight into the different types of molecules that enable selective XEC.

2.1.2 Computational Rationale

Scheme 2.2 Comparison of Proposed Computational Model Species

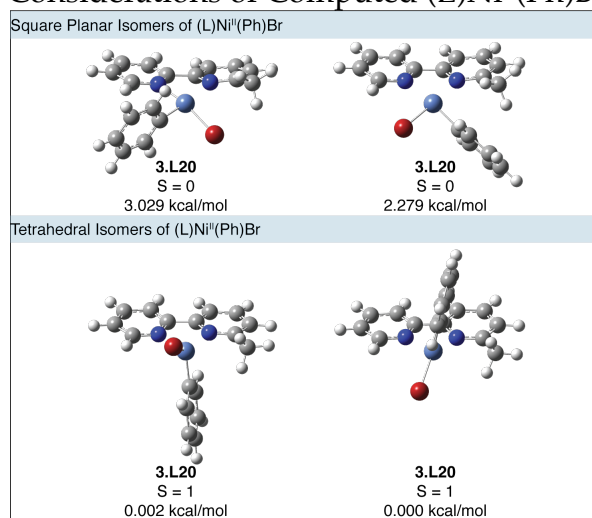


Many previous reports of statistical modelling of reaction outcomes have derived molecular features from optimized free-ligand structures.^{34–37} The exclusion of the metal center and additional ligands reduces computational intensity and enables direct observation of ligand features—donation of a lone pair can decrease the dynamic range of certain descriptors such as NPA charges. Despite these advantages, work by Doyle and coworkers demonstrated that inclusion of a metal center and even on-cycle intermediates can lead to improved predictivity and robustness.³⁷ Faced with these options, we considered four possible species to utilize as the model structure (Scheme 2.2): (1) the

unbound ligand absent any metal, (2) $(L)Ni^0$, (3) $(L)Ni^{II}(X)_2$, and (4) $(L)Ni^{II}(Ar)X$. While computations of the free ligand offer significant increases in computational efficiency, the differences in ground-state and metal-bound geometries—e.g. bpy ligands have cis nitrogens when bound to a metal center, but trans nitrogens in the free ligand geometry; contrastingly, phenanthrolines are conformationally locked—and lack of nuance dissuaded us from utilizing these as our sole source of insight. $(L)Ni^0$ structures were not utilized for two reasons: first, reactivity of the $(L)Ni^0$ intermediate is often not a limiting factor in XEC; second, computational results demonstrate significant distortion of nickel(0) complexes when additional stabilizing ligands are excluded.⁴⁶ As such, we hypothesized that additional, explicit solvent molecules would be necessary to gain a realistic insight into the structure of $(L)Ni^0$, mitigating many of the computational benefits. While Doyle found that efficient correlations of were possible using descriptors derived from $(L)Ni^{II}(X)_2$ complexes, we felt that the use of a downstream intermediate combined with the tetrahedral ground state would limit insight into the structure of the catalytic species present in the selectivity-determining step.³⁷ We chose instead to utilize $(L)Ni^{II}(Ar)Br$ complexes as our computational model. As the catalytic species that participates in the putative selectivity-determining radical capture step, we hypothesized that employing $(L)Ni^{II}(Ar)Br$ as a computational model system would provide the most in-depth insight of the structures we considered. Further, these systems provide unique insight into differences in binding modes and nickel geometry that is ablated in $(L)Ni^{II}(X)_2$, which is consistently tetrahedral. Despite these advantages, the use of this computational model system also introduced complexity, as we had to consider four possible geometries about the nickel: two isomers of square planar nickel and two non-symmetric tetrahedral geometries, as distortion of the tetrahedral nickel center leads to

non-equivalent geometries (Scheme 2.3).^D We decided that, for consistency, we would proceed to include only the lowest-energy square planar isomer and the lowest-energy tetrahedral structure.^E

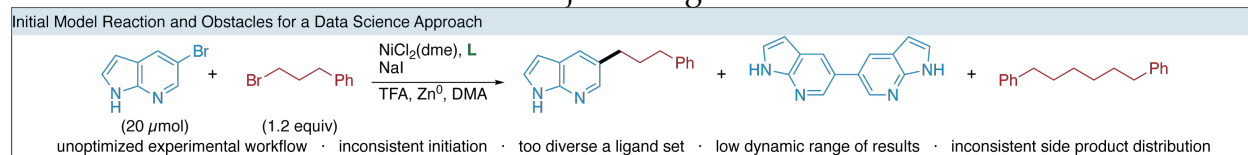
Scheme 2.3 Geometric Considerations of Computed (L)Ni^{II}(Ph)Br Structures^a



^aEnergies are solvated single points computed with the method detailed in Section 3.4.5.1 and are presented relative to the lowest-energy isomer.

2.2 Results and Challenges in Data Science

Scheme 2.4 Obstacles of Our Initial Project Design



We selected a model XEC reaction between a challenging heteroaryl halide and primary alkyl halide (Scheme 2.4). Experimental and computational workflow were fraught with subpar choices and inefficient workflows. The selection of ligands (examples

^D Additionally, this provides for an effective check that the lowest-energy optimized conformer has been computationally obtained.

^E For example, 2,2'-bipyridine favors a square planar (L)Ni^{II}(Ph)Br by 6.30 kcal/mol, whereas 6-methyl-2,2'-bipyridine and 6,6'-dimethyl-2,2'-bipyridine favor a tetrahedral (L)Ni^{II}(Ph)Br by 2.28 kcal/mol and 7.97 kcal/mol, respectively. These values are obtained from solvated SP energies; M06/cc-pVTZ,SDD(Ni) / M06/cc-PVDZ,LANL2DZ(Ni); SMD=DMA.

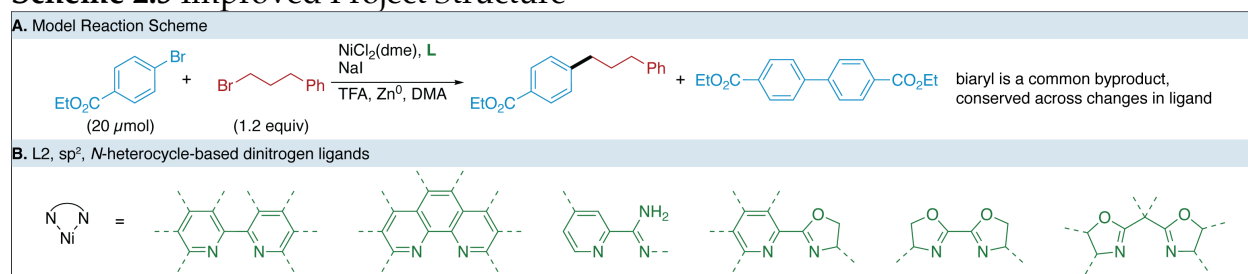
in Scheme 2.1) used to collect a dataset used as an initial survey of reactivity gave rise to a low dynamic range of results: most outcomes provided < 50% yield of the cross product. Many conditions produced no detectable cross product. Of the observations corresponding to ligands that did produce the cross product, we noticed that either our sampling or analysis methods were inconsistent, leading to a decrease in the veracity of the dataset. In the analysis of our data, we were unsure of what energetic metric would be optimal to use in our modelling efforts as our experimental observable. Much of our other issues in using this dataset for modeling arose from the dissimilarity of the ligands. Our initial goal of diversifying our ligand library in terms of donor identity, donor hybridization, denticity, and ligand type (L or X) created a series of issues. We considered selectivity for the cross product over either the aryl or alkyl homodimer, but our evaluated ligands produced an inconsistent spectrum of byproduct distribution—some ligands primarily generated the alkyl homodimer, others primarily generated primarily the aryl homodimer, and some produced a mix of both alkyl and aryl homodimers. We also considered direct analysis of rate of product formation utilizing the method of initial rates; however, this method was unsuccessful as non-selective ligands often yielded high apparent rates due to unproductive catalyst turnover. Further, the large differences in initiation time and observed reaction rates led to inconsistent measurements of rate due to difficulties in consistent sampling these reactions on a 96-well plate scale.

In retrospect, we needed to set boundaries for our ligand selection. In the intervening time, we observed that phosphine libraries such as *kracken*³² have separated true phosphines and related phosphorus-based ligands into separate categories, with further subcategories for denticity. Additionally, analyses of dinitrogen ligands often classify them into distinct classes: BiOx, BiIm, BOX, bpy, etc. While our initial efforts may

have been successful given a sufficiently large dataset with a large decision tree to partition our data into dissimilar subsets. This complexity would only mimic the intuition of practicing chemists, leading to long-form analyses that yielded answers as simple as “bipyridines do x , terpyridines do y ”. We felt that this large-scale, high-effort, top-down approach was not amenable to our limited time, resources, and expertise.

2.3 Insights Gained and Improved Project Structure

Scheme 2.5 Improved Project Structure



Given the shortcomings of our initial project structure, we decided to leverage our newfound insight to reconstruct a more achievable—yet still impactful—project design, with changes made to both the experimental and computational design. First, we simplified the model reaction to the validated coupling of ethyl 4-bromobenzoate with 1-bromo-3-phenylpropane (Scheme 2.5). While searches for new ligands that enable the coupling of difficult *N*-heterocycles have been successful in the past, the increased density of low-yielding results makes statistical measures less effective. This new model reaction has been successfully used in the translation of XEC to electrochemical systems,^{47,48} in the previous high-throughput campaign that yielded PyCam and PyBCam ligands,¹⁴ and in the discovery of heteroaryl carbonitrile ligands.⁴⁹ Notably, this reaction provides a wide range of yield and selectivity based on the ligand employed. Additionally, the consistent distribution of side products enables the addressing of individual mechanistic problems via correlation and regressive techniques.

The largest modification to the project structure focused on the selection of ligands employed in the training set. The obstacles we previously encountered due to the diversity in binding mode, hybridization, charge, and identity of donor atoms,⁵⁰ were avoided by the narrowing of focus to exclusively L2, sp²-hybridized dinitrogen donors. While less ambitious than our previous efforts, these ligands make up a majority of those commonly employed in nickel-catalyzed cross-electrophile coupling. As such, the identification of critical molecular features that govern the reactivity and selectivity promoted by these ligands would offer a significant advance in cross-electrophile and redox-neutral cross-couplings. We chose to exclude L3 ligands such as bpp, tpy, PyBCam, and bpyCam derivatives due to their tendency to promote different side product distributions, ionize halides, and support different oxidation states of nickel. With a scope of ligands defined, we searched for ligands amongst six individual classes that are validated in nickel-catalyzed XEC: (1) 2,2'-bipyridines, which often serve as a standard of reactivity, (2) 1,10-phenanthrolines, which are related to bpys but display an extended π system, (3) pyridyl carboxamidines, which have been shown to offer improved selectivity and utility over equivalent bpy ligands, (4) pyridyl oxazoline ligands which offer diverse modulation of steric and electronic properties, (5) 2,2'-bioxazoline ligands which offer a conjugated π -system and C₂ symmetry, and (6) bis(oxazoline) ligands, which are widely developed and utilized in asymmetric catalysis. Amongst these six classes, we selected ligands based on availability from commercial sources and internal inventory, making sure to gather ligands with variation in steric and electronic properties. The resulting suite of 78 ligands provides the basis for a bottom-up understanding of selectivity in nickel-catalyzed cross-electrophile coupling utilizing correlations of molecular descriptors to reaction outcomes.

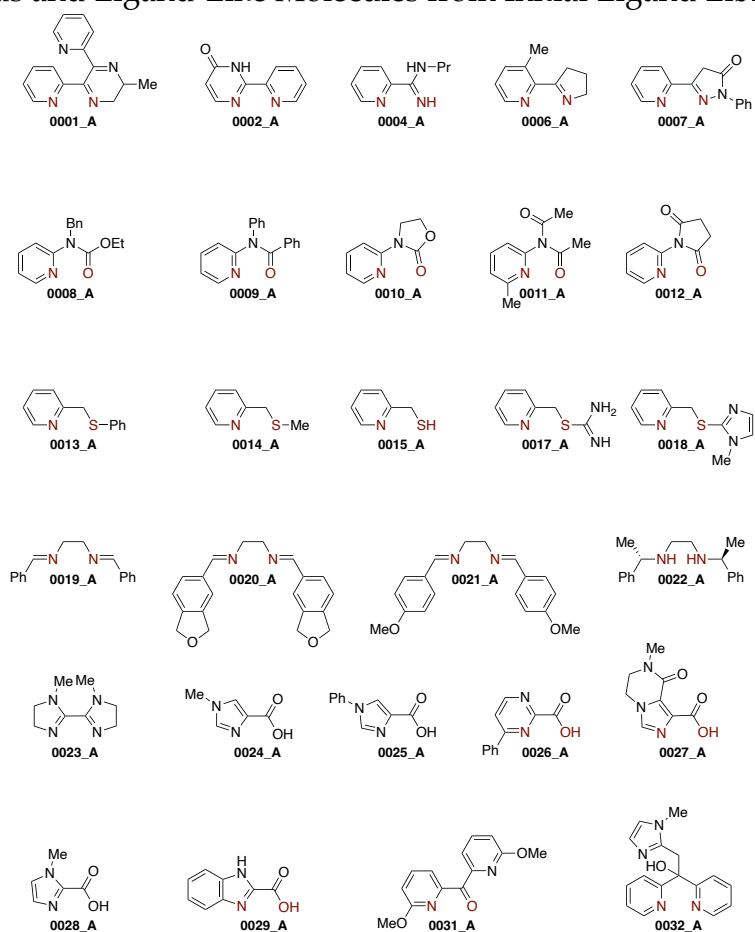
The final modification to the project structure regarded the data science and modelling goals. Whereas we had previously made attempts to generate correlations with yield or the rate of cross-product formation, these two measures are greatly complicated by the prevalence of off-cycle pathways and ligands that display little productive reactivity. Instead, the conserved distribution of side products provided by the selected suite of catalysts—most prominently the aryl homodimer—enabled the direct modelling of selectivity for the desired product vs. the aryl homodimer. This decision more closely mirrors previous studies and allows for the generation of LFERs by converting the observed selectivity to a $\Delta\Delta G^\ddagger$ via the Curtin-Hammett Equation.³⁴⁻³⁷

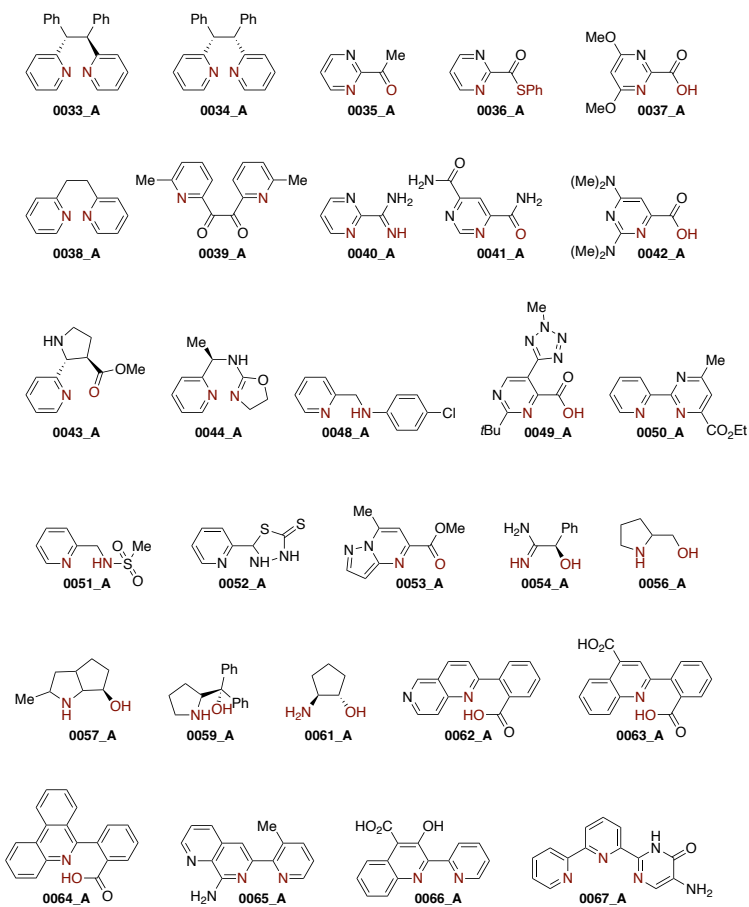
The results of this investigation are described in Chapters 3 and 4. Thus far, this narrower approach has enabled the successful generation of a model for selectivity in bipyridine-nickel catalyzed XEC, and the *in silico* design of improved ligands. Initial analysis of the additional ligand classes demonstrates promising results. We expect that continued work applying the statistical measures described here can enable a general understanding of selectivity that helps rationalize reaction outcomes amongst and between different classes of ligands.

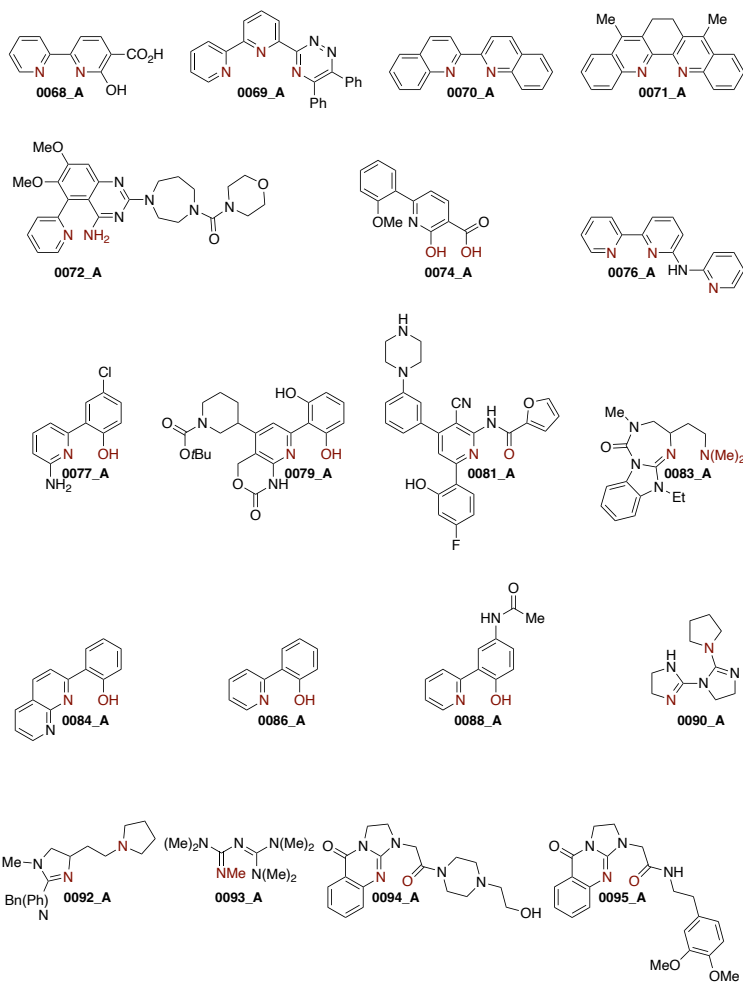
2.4 Experimental

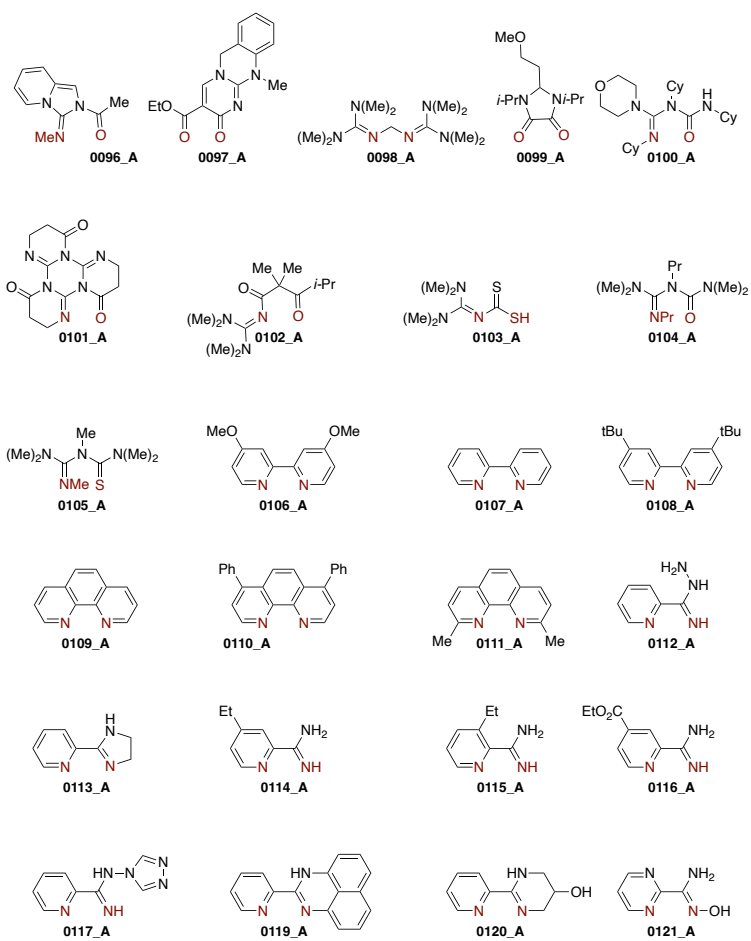
2.4.1 Ligand Key

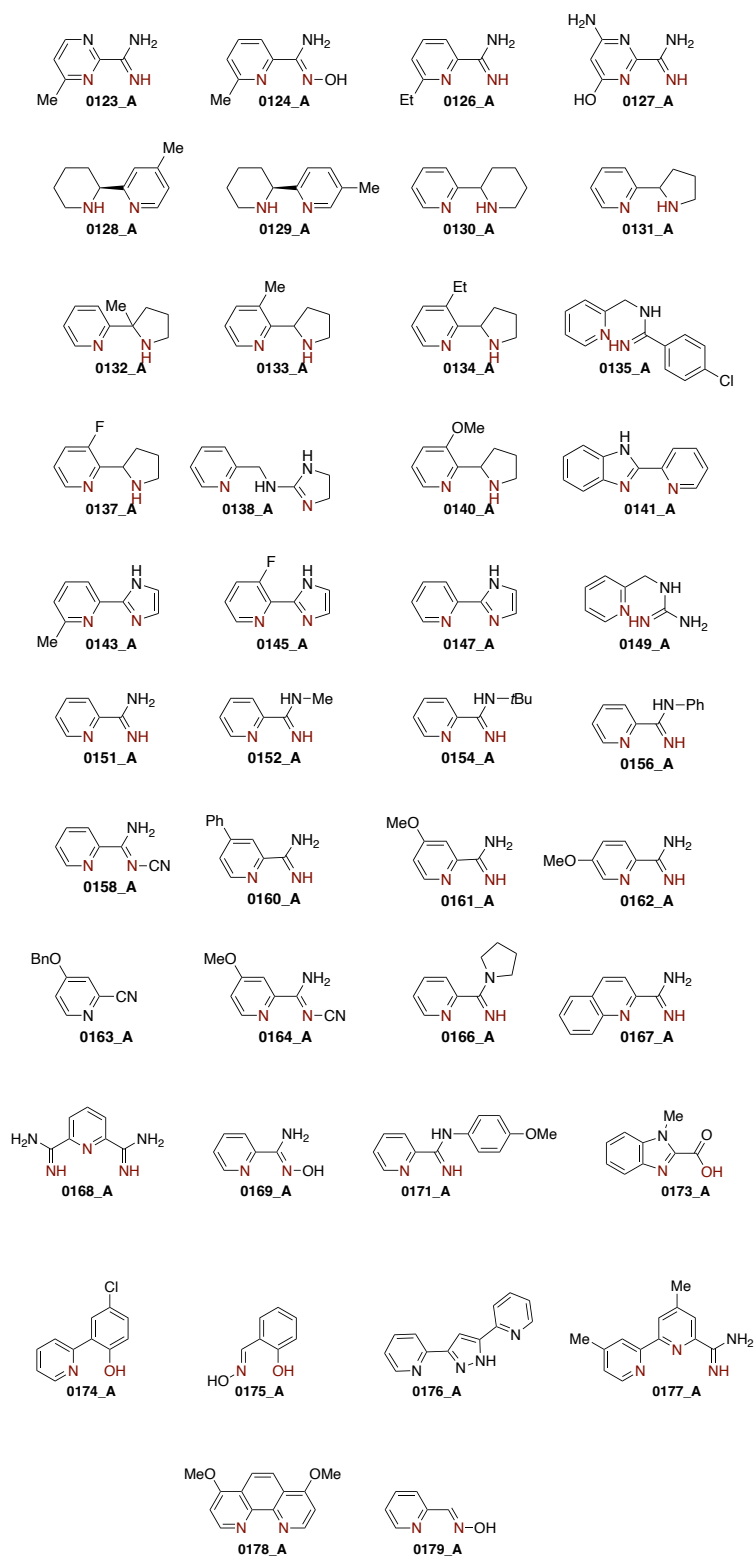
Listed below is our initial ligand library that was explored computationally and experimentally, with the experiments summarized in Section 2.2. Many of the ligands listed here are also present in subsequent chapters and are listed separately there with their associated computational and experimental datasets.

Figure 2.1 Ligands and Ligand-Like Molecules from Initial Ligand Library







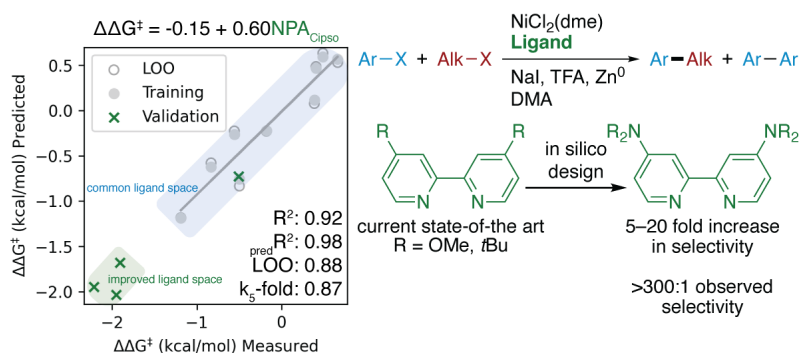


2.4.2 Computational Details

All computations were performed using the Gaussian 16, Rev. C.01 suite using defaults unless noted otherwise.⁵¹ Optimized structures are visualized using GaussView 6.0.10.⁵² The “ultrafine” integration grid setting was used in all computations. Initial optimization and parameterization⁵³ was performed at the M06/cc-pVTZ,SDD(Ni)//M06/cc-pVDZ,LANL2DZ(Ni) level of theory.⁵⁴⁻⁵⁸ The frequency keyword “noraman” was used in all frequency calculations to increase computational efficiency. Corrections for the solvation energies were obtained from the difference between single points with the SMD continuum solvation model for DMA (*N,N*-dimethylacetamide)⁵⁹ and a gas phase single point, both using M06/cc-pVTZ, SDD (Ni). Conformers of higher energy were accounted for in all cases. Stationary points were characterized as ground states by the absence of negative eigenvalues (zero imaginary frequencies) in frequency analysis at the same level of theory as the geometry optimization.

We have chosen to not include the primary data for this ligand set due to changes in the computational method and rationale to better accommodate triplet nickel(II) geometries (Section 3.4.5.1). Further, inconsistencies in charge of the calculated nickel complexes make direct comparison of many of the computational results difficult.

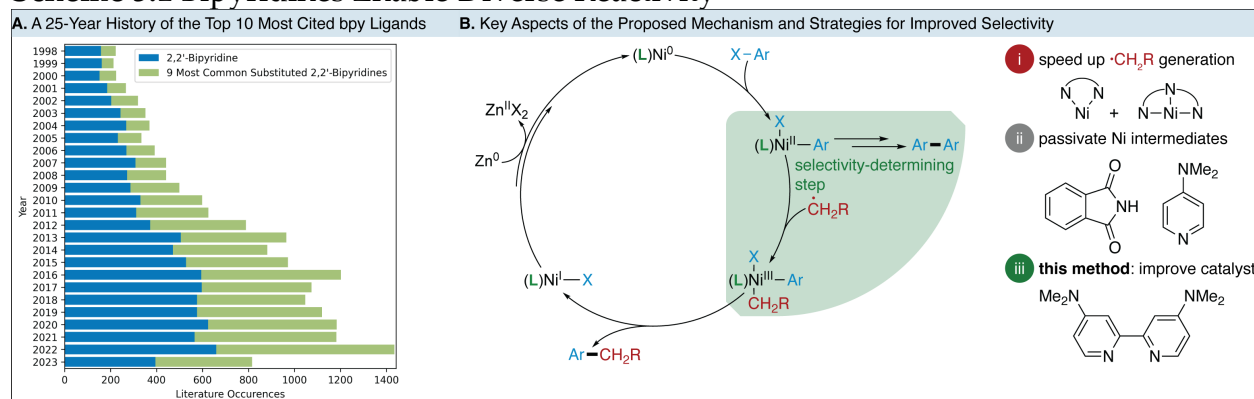
Chapter 3: Computational Methods Enable the Prediction of Improved Catalysts for Nickel-Catalyzed Cross-Electrophile Coupling



The work described in this chapter has been published and is reprinted in its adapted form with permission from Akana, M. E.; Tcyrulnikov, S.; Akana-Schneider, B. D.; Reyes, G. P.; Monfette, S.; Sigman, M. S.; Hansen, E. C.; Weix, D. J. Computational Methods Enable the Prediction of Improved Catalysts for Nickel-Catalyzed Cross-Electrophile Coupling" *J. Am. Chem. Soc.* **2023**. DOI: 10.1021/jacs.3c09554. Copyright © 2023 American Chemical Society.

3.1 Introduction

Scheme 3.1 Bipyridines Enable Diverse Reactivity^F



Heterocycle-based, L2 dinitrogen ligands are critical enabling components of many transition metal-catalyzed C–C, C–N, and C–O bond forming reactions. These ligands—typified by 2,2'-bipyridine (bpy)—enable reactivity distinct from phosphine ligands by promoting a diverse set of 1- and 2-electron-processes.^{60–63} In particular, bpy ligands have become a fixture of nickel-catalyzed cross-electrophile,⁶⁴ metallophotoredox,⁶⁵ and electrochemical^{66–68} couplings, and are often the implicit standard by which the reactivity of other ligands are gauged. The increased demand for more diverse and robust cross-coupling reactions has driven the incorporation of an increasingly modified suite of substituted bpy ligands (Scheme 3.1A). Despite this diversification and their impact on numerous fields, in-depth systematic study of the effects of critical molecular features on the reactivity of bipyridines remains limited.

Ni-catalyzed C(sp²)-C(sp³) cross-electrophile coupling XEC—an attractive method for the incorporation of C(sp³) character into a variety of molecules^{2,69,70}—is dependent on

^F All data are from Reaxys search on 6/27/23 for 2,2'-bipyridine with GH group attached to all carbons. Only data from past 25 years (1998–6/7/23) are depicted. Ligands erroneously classified as bpps (e.g. tpys) and molecules predominantly used in OLEDs or materials chemistry were excluded.

the selection of an appropriate ligand, most often a derivative of 2,2'-bipyridine (bpy). While extensive optimization and expansion of this reaction manifold has enabled the use of new substrate classes, dimerization of the C(sp²) component remains problematic. Slow radical capture and reductive elimination can allow for reductive degradation of an intermediate arylnickel(II) species (Scheme 3.1B).^{6,71} Approaches to mitigate this issue often focus on either increasing the rate of radical generation—in an effort to accelerate the productive pathway—or decreasing the rate of disproportionation of the arylnickel intermediate.

Methods from Weix,^{17,47,48} Sevov,¹⁸ and others² have demonstrated the use of a mixed-catalyst system where one catalyst is exclusively responsible for generation of an alkyl radical, and another engages the C(sp²) coupling partner and facilitates formation of the desired C–C bond. An alternative approach is the addition of stoichiometric additives—such as phthalimide or pyridine derivatives—which passivate open sites of the arylnickel intermediate, slowing the rate of deleterious disproportionation.^{2,72,73} While these and other modifications have proven effective in many cases, they also introduce complications—such as mistuned catalyst ratios and decreased atom economy, respectively. A more attractive approach would be the systematic development of a more selective catalyst, which would enable more robust, efficient, and general reactions. Further, this catalyst could be used in combination with the above methods to improve rate or engage otherwise inaccessible substrate pools.

The underlying issue in exploring this option is that bpy-based catalysts lack the extensive developmental schema possessed by phosphines. There are significantly fewer known and commercially available bipyridine ligands, which limits the rate and breadth of methodology development as new ligands must often be synthesized prior to being

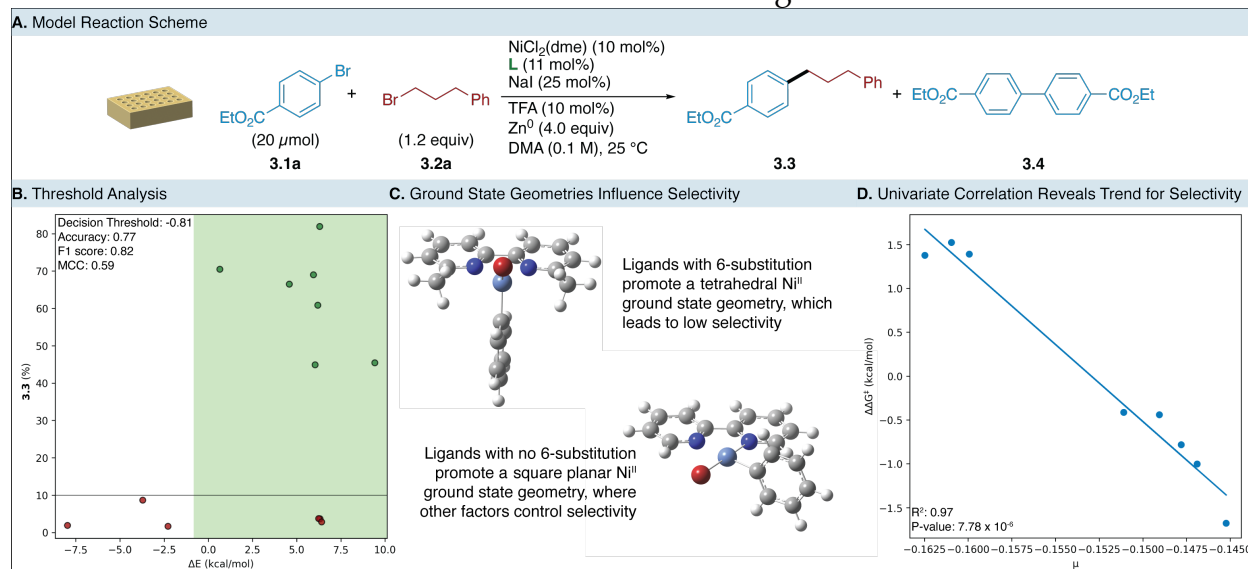
tested. Thus far, approaches to overcome this developmental gap have focused on general surveys of reactivity,^{38,61} hypothesis-driven skeletal modifications,⁷⁴ or high-throughput experimentation (HTE) campaigns to identify new classes of ligands,¹⁴ often with the goal of expanding reaction scope to access more challenging substrates. More frequently, HTE is employed to identify an optimal catalyst from a pre-existing suite of ligands with validated reactivity.^{16,75} While these methods have provided a basis of understanding for the reactivity of specific catalysts, they have yet to deliver a sufficiently detailed model of reactivity to enable the validated identification or tailored design of improved catalytic systems.

In this context, statistical methods that correlate computationally-derived molecular features to reaction outcomes have accelerated the design, selection, and commercialization of optimal phosphine-ligated catalysts.^{29,33,76} Thus far, the translation of these methods to L2 dinitrogen ligands remains limited. Most often, the resulting statistical models are utilized to rationalize enantio- or site-selectivity. For example, the Sigman group has reported the use of multivariate linear regression to rationalize and design improved 2-(2-pyridyl)oxazoline ligands in enantioselective Heck arylations.^{34,35} Additionally, Doyle and coworkers have utilized a similar workflow to explain the improved enantioselectivity provided by 2,2'-biimidazoline ligands compared to related bioxazolines—specifically exploring correlations with descriptors from (L)NiF₂ and (L)Ni(Ar)Cl complexes—where they noted improved correlations when parameters were sourced directly from the catalytic intermediate involved in the stereodetermining step.³⁷ Based on the general success of these approaches, we hypothesized that a similar data science workflow could be applied to more general obstacles of selectivity and robustness in nickel-catalyzed cross-electrophile couplings.

Herein, we describe the application of modern computational and statistical methods to construct correlations of reaction performance in cross-electrophile couplings as a function of the bipyridine ligand. The resulting models communicate two key features of a successful catalyst: a square planar (L)Ni^{II}(Ar)Br intermediate and a strongly donating ligand. This model is robust and predictive, allowing for the interpolative and extrapolative prediction of performance for untested bipyridine ligands. Additionally, we designed a suite of improved 4,4'-bis(dialkylamino)-2,2'-bipyridine ligands in silico, which were predicted to provide significant improvements in selectivity for the desired product. In action, these new ligands facilitate the high yielding coupling of a variety of alkyl and aryl electrophiles. We expect that the expanded application of the improved ligands identified in this study will enable the accelerated development of new cross-coupling reactions.

3.2 Results and Discussion

Scheme 3.2 Model Reaction and Initial Data Processing Efforts



We initially selected the cross-electrophile coupling of primary alkyl and aryl bromides as a prototypical model reaction for exploring the impact of ligand structure on

reaction performance (Scheme 3.2A). This coupling provides a consistent set of byproducts—primarily the aryl homodimer (**3.4**)—where selectivity is determined by the relative concentrations of **3.3** to **3.4** at 24 h; this ratio of product to aryl homodimer is converted to an expression of energy, $\Delta\Delta G^\ddagger$, via the Curtin-Hammett equation,

$$\Delta\Delta G^\ddagger = -RT \ln \left(\frac{[\mathbf{3.3}]}{[\mathbf{3.4}]} \right)$$

As such, negative values of $\Delta\Delta G^\ddagger$ are obtained for reactions that selectively form **3.3** over **3.4**. This validated coupling has been used as a model system in several ligand identification studies and for the translation of XEC methods to other reductive systems.^{14,49}

We gathered an initial dataset by evaluating a suite of substituted bipyridines and related ligands in 96-well plates (20 μmol scale). This ligand suite resulted in a wide dynamic range of results (2–82% yield of **3.3**^G) and confirmed that the yield of the desired product is primarily determined by the selectivity for the cross-product (**3.3**) over the aryl homodimer (**3.4**) (Figure 3.3).

Given the diversity in substitution patterns in the ligand suite (4,4'-, 5,5'-, 6-, or 6,6'-(di)substituted), it was readily apparent that tabulated molecular descriptors (i.e., Hammett or Charton values) would be insufficient for modelling selectivity. To gain insight into the intrinsic characteristics of each catalyst and adequately describe this diversity, we generated a library of DFT-optimized (L)Ni^{II}(Ph)Br catalysts from which we would derive molecular parameters.^{51,53–55,57–59,77}

^G These results span a range of 3.51 kcal/mol in $\Delta\Delta G^\ddagger$.

We hypothesized that parameters derived directly from the oxidative addition complex—the intermediate that presumably is responsible for defining selectivity—would provide unique insight into the structure of selective catalysts.³⁷ Further, the resulting dataset should be translatable to other nickel-catalyzed cross-couplings of haloarenes. We obtained a variety of electronic (e.g. NPA charges of atoms in the primary coordination sphere, nickel d-orbital energies and occupancies, etc.) and steric parameters for each catalyst in both the square planar and tetrahedral geometry.⁴² This computational dataset offers detailed insight into the electronic and steric structure of each catalyst and is provided in full as a supplementary file.

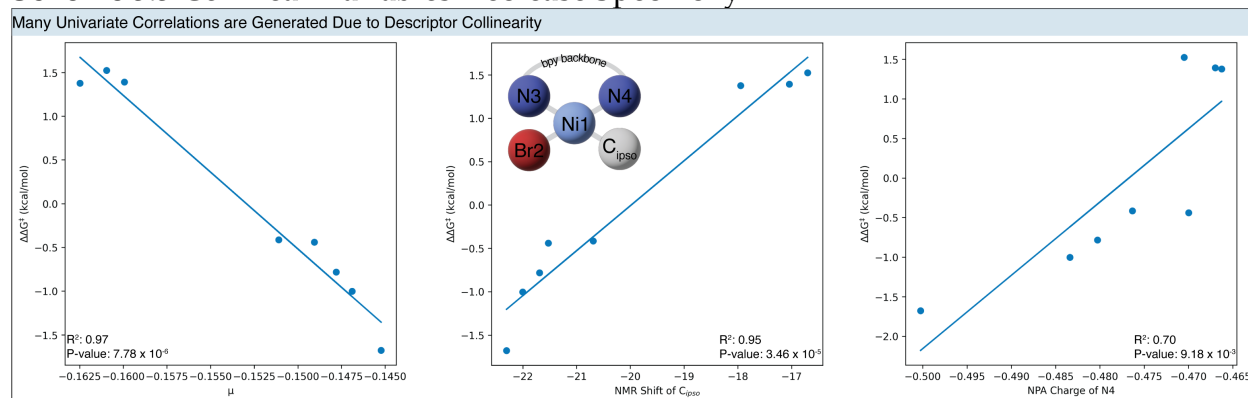
Initial linear correlations between the experimental results and computational descriptors yielded poor results that did not adequately incorporate a grouping of observations that gave $\leq 10\%$ yield of **3.3**. We hypothesized that two separate features may lead to low selectivity via distinct mechanisms. Indeed, classification of yield of **3.3** using a single node decision tree with a threshold value of 10% yield revealed a reactivity cliff based on the difference in energy between the tetrahedral and square planar geometries of the (L)Ni^{II}(Ph)Br complex (Scheme 3.2B).³¹ Sterically hindered 6- and 6,6'-(di)substituted ligands promote a tetrahedral geometry in the ground state and rapidly dimerize the aryl bromide, leading to low selectivity.⁷⁸ Contrastingly, ligands with 4,4'- or 5,5'-substitution yield (L)Ni^{II}(Ph)Br complexes with a square planar ground state and tended to result in yields $> 10\%$ of **3.3** across a range of selectivities.

Bipyridine ligands with 6,6'-disubstitution and related phenanthrolines are known to display reactivity distinct from their unhindered analogues (Scheme 3.2C).⁷⁹ While differences in speciation may play a role, large 5,5'-disubstituted ligands—which display similar reactivity to other unhindered bipyridines—suggest that reliable mono-

ligation is not the selectivity-determining factor.⁷⁴ Instead, we hypothesized that the ability of these ligands to support stable nickel(I) intermediates enables access to decomposition from (L)Ni^I(Ar).⁸⁰

Based on the results of the yield classification, we curated the scope of the training set to 4,4'- and 5,5'-disubstituted bipyridines. Using this dataset, we found several univariate correlations between molecular descriptors and selectivity (Scheme 3.2D and Figure 3.16). Amongst the best correlations, we found a robust univariate model for selectivity based on the chemical potential, μ , of the catalyst. As the average of the HOMO and LUMO energies, μ increases with increased donation of the ligand. This is reflected in the qualitative trend that ligands bearing electron-donating ligands in the 4,4'-positions yielded the highest selectivity.

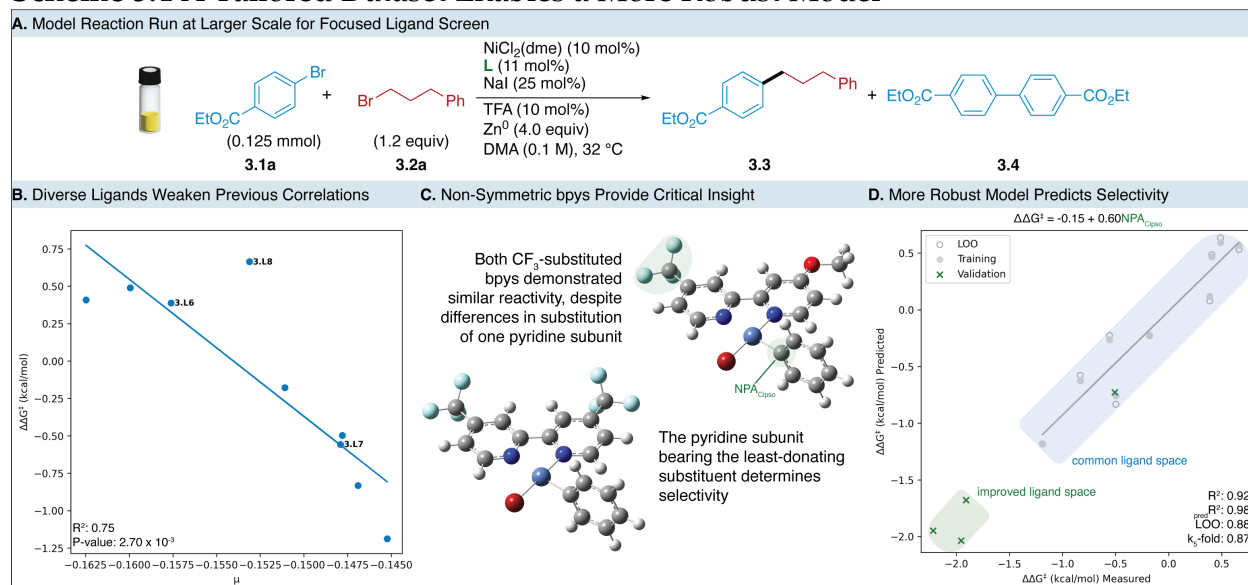
Scheme 3.3 Collinear Variables Decrease Specificity



Despite this initial success, the specificity and translatability of the model remained unclear. We found that the best univariate correlations (Scheme 3.3; 19 examples where $R^2 > 0.70$ and $p\text{-value} < 0.01$) existed between directionally oriented, highly collinear descriptors (Figure 3.17). The collinearity in the parameters caused by the symmetric bipyridine structures led to convolution of the computational dataset. As such, we hypothesized that the introduction of non-symmetrically substituted

bipyridines would serve to decrease the number of collinear directional descriptors by exaggerating the lack of electronic symmetry in the square planar (L)Ni^{II}(Ph)Br complex. Further, we hypothesized that addition of non-symmetric bipyridines would differentiate directional or atom-specific descriptors (e.g., NPA charge of a single nitrogen donor) from additive parameters (e.g., μ or d-orbital energies). To test this hypothesis, we constructed a suite of non-symmetric and select symmetrically substituted bpys, which were subsequently evaluated on a larger scale (0.125 mmol, Scheme 3.4A).

Scheme 3.4 A Tailored Dataset Enables a More Robust Model



Univariate correlations utilizing this new dataset revealed that many of the strong correlations that we had previously observed were not maintained with the introduction of non-symmetric ligands. In fact, the previous best correlation involving μ was significantly weakened (R^2 of the univariate correlation decreased from 0.97 to 0.75, Scheme 3.4B). This is due to selectivity being solely determined by the least donating pyridine unit; for example, 4-methoxy-4'-(trifluoromethyl)-2,2'-bipyridine (**3.L7**) yields selectivity similar to 4,4'-bis(trifluoromethyl)2,2'-bipyridine (**3.L9**), rather than 4,4'-

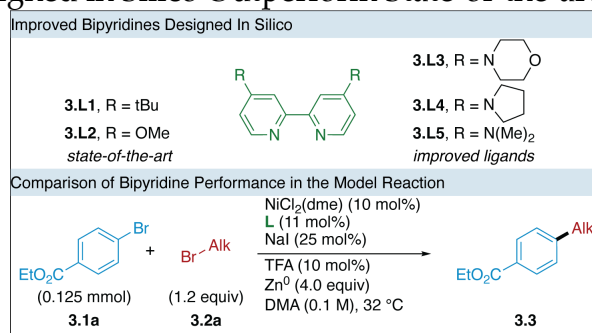
dimethoxy-2,2'-bipyridine (**3.L2**). This observation, combined with the consistent arrangement of the donor atoms in the low-energy isomer of the (L)Ni^{II}(Ph)Br complex led to delineation of the parameters (Scheme 3.4C).

Using these results, we identified a univariate correlation for selectivity of **3.3** over **3.4** in the model cross-electrophile coupling reaction (Scheme 3.4D), which relies on the NPA charge of the ipso carbon of the phenyl ligand. Using this model, a virtual screen was performed with the goal of external validation of this correlation as well as extrapolating the model for improved selectivity. Several ligands were thus synthesized and evaluated whereby the model was able to predict the performance of new bipyridine ligands. The robustness of this model in predicting of both symmetric and non-symmetric bipyridines is due to the consistent alignment of the least electron-rich pyridine ring—which determines selectivity—trans to the phenyl in the low-energy isomer. As the nitrogen trans to C_{ipso} becomes more donating, the NPA charge of C_{ipso} decreases, and selectivity rises.

This model is robust—LOO = 0.88, k₅-fold = 0.87—and predictive ($_{\text{pred}}R^2 = 0.98$) of both an interpolated and extrapolated observations. The use of computational parameters derived directly from a catalytic intermediate offers a distinct advantage over the use of tabulated descriptors—such as Hammett parameters. First, the model effectively predicts the selectivity of 5,5'-disubstituted bpy derivatives, as DFT gauges π -donation across the bpy backbone. Second, the model accurately predicted the selectivity of non-symmetrically substituted ligands without direct intervention; this is attributable to the consistent orientation of the donor atoms in the low energy isomer. Further, the specificity of DFT-derived parameters can provide more impactful mechanistic insight.

Osakada and co-workers found that the rate of disproportionation of $\text{bpyNi}^{\text{II}}(\text{Ar})\text{Br}$ was higher for electron-rich haloarenes and lower for electron-poor haloarenes.⁸¹ This would suggest that a more negative NPA charge of C_{ipso} leads to a higher rate of disproportionation.⁸² Our results suggest the opposite is true under reducing conditions. We hypothesize that under reducing conditions, direct disproportionation is not the dominant mechanism by which **3.4** forms. Instead, we propose that dimerization occurs primarily via the reduction of $(\text{L})\text{Ni}^{\text{II}}(\text{Ar})\text{Br}$ to form $(\text{L})\text{Ni}^{\text{I}}(\text{Ar})$. This is supported by the observation that 6,6'-disubstituted bipyridines—which are known to form stable nickel(I) complexes—and electron-poor bipyridines—which also have recently been shown to form $(\text{L})\text{Ni}^{\text{I}}(\text{Ar})$ complexes—both lead to rapid dimerization of **3.1a**.^{38,83} Further computational and experimental investigation is needed to investigate the mechanism by which this occurs, but is beyond the scope of this work.

Table 3.1 Ligands Designed in Silico Outperform State-of-the-art Bipyridines^a



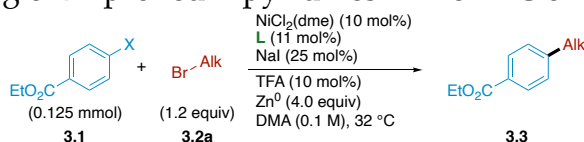
Entry	L	3.3 (%)	Selectivity (3.3:3.4)	$\Delta\Delta G^\ddagger$ (kcal/mol)
1	3.L1	49	2:1	-0.5
2	3.L2	61	7:1	-1.19
3	3.L3	82	23:1	-1.91
4	3.L4	88	25:1	-1.95
5	3.L5	79	39:1	-2.22

^aAlk = 3-Phenylpropyl. Reactions were assembled in a nitrogen filled glovebox at a 0.125 mmol scale in 1.25 mL of DMA. Yields and selectivity were determined by GC-FID.

Via extrapolation from the model, we designed a series of improved 4,4'-bis(dialkylamino)-2,2'-bipyridines in silico (Table 3.1). After synthesizing these ligands,

we found that the model had correctly predicted the over fivefold increase in selectivity that they enabled (from 7:1 to 39:1 of **3.3:3.4** for **3.L2** and **3.L5** respectively). Further, the ability to predict selectivity *in silico* eliminated unnecessary synthetic effort, as we had initially hypothesized that 4,4',5,5'-tetramethoxy-2,2'-bipyridine (**3.L31**) might offer an increase in selectivity; but the model predicted that this ligand—accessed via six steps from commercial sources—would only provide a modest improvement over the common **3.L2**. As such, we did not pursue the synthesis of **3.L31**.

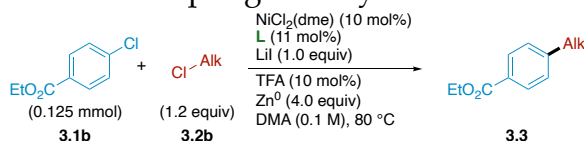
Table 3.2 Benchmarking of Improved Bipyridines in the XEC of Aryl Halides^a



Entry	X	Result with 3.L5 (3.3% , 3.3:3.4)	Result with 3.L2 (3.3% , 3.3:3.4)
1	Cl	93, 311:1	85, 17:1
2	Br	79, 39:1	61, 7:1
3	I	87, 96:1	76, 29:1

^aAlk = 3-Phenylpropyl. Reactions were assembled in a nitrogen filled glovebox at a 0.125 mmol scale in 1.25 mL of DMA. Yields and selectivity were determined by GC-FID.

Table 3.3 NMe₂bpy Enables the Coupling of Alkyl Chlorides^a



Entry	L	3.3 (%)	Selectivity (3.3:3.4)
1	3.L1	4	1:114
2	3.L2	11	1:9
3	3.L5	62	25:1

^aAlk = 3-Phenylpropyl. Reactions were assembled in a nitrogen filled glovebox at a 0.125 mmol scale in 1.25 mL of DMA. Yields and selectivity were determined by GC-FID.

To investigate the generality of these improved bipyridine ligands, we evaluated the cross-electrophile coupling of a variety of aryl and alkyl halides. We found that both the overall and relative selectivity—an almost 20-fold increase from 17:1 to 311:1 compared to **3.L2**—significantly improved when coupling less reactive and more

abundant chloroarenes (Table 3.2). Additionally, using modified conditions, we were able to leverage the stability of the (L)Ni^{II}(Ar)X intermediate to effectively couple unreactive chloroalkanes (Table 3.3), whose coupling has thus far been inaccessible utilizing bipyridine ligands.^{84,85} These results suggest that **3.L5** may be widely applicable in providing more robust couplings in known XEC systems.

Table 3.4 NMe₂bpy Increases the Efficiency of Existing Coupling and Unlocks New Substrate Pairings^a



Entry	X	3.3 (%)	Selectivity (3.3:3.4)
1	Br	98	84:1
2	Cl	55	7:1
3	Cl	86 ^b	8:1

^aAlk = 3-Phenylpropyl. Reactions were assembled in a nitrogen filled glovebox at a 0.125 mmol scale in 735 μ L of NMP. Yields and selectivity were determined by GC-FID. ^b20 mol% of NiCl₂(dme) and 22 mol% of **3.L5** were used.

We were also able to directly substitute **3.L5** for **3.L2** in the reported coupling of *N*-alkyl 2,4,6-triphenylpyridiniums with aryl bromides (Table 3.4).⁸⁶ We found that the use of this ligand yielded the desired product in 98% yield. This extended the observed trend in yield from the published optimization in the original report—**3.L1**<**3.L2**<**3.L5**. While arylation of *N*-alkylpyridiniums is well-known for bromoarenes, effective coupling of chloroarenes remains elusive. We hypothesized that the increased electron-density of **3.L5** may allow for more rapid oxidative addition into chloroarenes. We found that the equivalent chloroarene coupled in 55% yield using the same conditions and increasing the catalyst loading—leveraging the low rate of aryl dimerization afforded by this catalyst, which should be increased at higher catalyst concentrations—led to 86% yield. Together, these results demonstrate that the use of this improved ligand can be

applied to improve other XEC reactions and couple previously inaccessible combinations of substrates.

Overall, this suite of 4,4'-bis(dialkylamino)-2,2'-bipyridines offers a significant increase in selectivity over the common state-of-the-art bipyridine ligands. Despite their utility and presence in the development of novel photocatalysts, application of any of these ligands to nickel catalysis is relegated to ineffective entries in optimization tables and a single use of **3.L5** on a particularly challenging substrate.⁸⁷ We expect that the relatively modest increase in yield when using **3.L2** in lieu of **3.L1** in combination with the difficulty in synthesizing novel, electron-rich bipyridines made these ligands an unattractive target for synthetic efforts. We hope that this study will accelerate the adoption of these ligands into the canon of bpy ligands in nickel catalysis. Currently, only the highest performing catalyst, **3.L5** is commercially available for a reasonable price. While we found them to be slightly less selective, **3.L3** and **3.L4** may offer benefits in solubility or selectivity in specific applications. Thus far, we have not identified any bipyridine ligands that are predicted to provide a significant increase in selectivity over **3.L5**. While small improvements may be possible, we expect that the next frontier in ligand design for XEC lies in the identification of new classes of ligands and alternative reaction pathways that avoid existing mechanistic obstacles.

3.3 Conclusions

In conclusion, we have applied modern computational and statistical methods to develop a model for selectivity in nickel-catalyzed cross-electrophile coupling. The two resulting models—a binary classification of a ligands' applicability based on the ground state of their (L)Ni^{II}(Ph)Br complex and a linear relationship between the NPA charge of the ipso carbon of the low energy (L)Ni^{II}(Ph)Br complex—enable the prediction of the

performance of a variety of substitution patterns with diverse functionalities. This study also highlighted the importance of designing a diverse, informative training set to minimize collinearity in computational parameters, and maximize interpretability. The use of parameters derived from a representative on-cycle intermediate enable strong models and mechanistic insight. These results suggest that, in contrast to previous stoichiometric studies under redox-neutral conditions, the primary dimerization pathway in XEC may proceed via degradative reduction of $(L)Ni^{II}(Ar)X$.

Using our model, we were able to design a suite of improved 4,4'-bis(dialkylamino)-2,2'-bipyridines. These ligands display significant improvements in selectivity and yield compared to the current state-of-the-art bipyridines. Further, they can be easily substituted into other cross-electrophile couplings to increase the yield and allow access to more diverse coupling partners. We expect that adoption of these ligands—in combination with existing strategies—will enable more robust, selective, and widely applicable cross-electrophile couplings.

This study translates modern statistical techniques—which are common in the analysis of phosphines and enantioselective catalysis—to nickel-catalyzed XEC. Overall, the expanded use of diverse statistical and computational tools will bolster experimental insight and enable more efficient and impactful ligand design and selection. The dataset that we used to generate these models persists and should be applicable to a variety of nickel-catalyzed processes. We have made the entire dataset, including parameters for common bipyridines and ligands that exist only in silico available as a supplementary spreadsheet. We hope that this dataset will make application of these methods more accessible to other researchers.

3.4 Experimental

3.4.1 General Information

3.4.1.1 Reagents

Metals and Catalysts

Nickel(II) chloride dimethoxyethane, NiCl₂(dme), was purchased from Sigma-Aldrich. Zinc flake (-325 mesh) and manganese powder (-325 mesh) were purchased from Alfa Aesar. Palladium(II) acetate was purchased from Chem-Impex International. All metals and catalysts were stored in a nitrogen-filled glovebox and used without additional purification.

Ligands

4,4'-Bis(trifluoromethyl)-2,2'-bipyridine and 4,4'-bis(dimethylamino)-2,2'-bipyridine were purchased from Ambeed. 2,2'-bipyridine was purchased from Sigma-Aldrich. 4,4'-dimethoxy-2,2'-bipyridine was purchased from Ambeed or Sigma-Aldrich. Dimethyl ([2,2'-bipyridine]-4,4'-dicarboxylate) was purchased from AstaTech. 4,4'-di-*tert*-butyl-2,2'-bipyridine was purchased from Sigma-Aldrich; reactions utilizing this ligand sourced from Ambeed and TCI America provided consistently lower selectivity. Additional ligands were acquired from commercial sources or internal inventories at Pfizer or UW-Madison. Ligands were stored and handled in a nitrogen-filled glovebox and used without further purification.

Substrates

Ethyl 4-bromobenzoate was purchased from Oakwood. Ethyl 4-chlorobenzoate was purchased from Alfa Aesar. Ethyl 4-iodobenzoate was purchased from Matrix Scientific.

1-Bromo-3-phenylpropane was purchased from TCI America. 1-Chloro-3-phenylpropane was purchased from Sigma-Aldrich. Unless otherwise specified, all substrates were purchased from commercial sources, stored on the benchtop, and used without further purification.

Solvents

N,N-Dimethylacetamide (DMA), *N*-methylpyrrolidone (NMP), toluene, and DMSO were purchased from Sigma-Aldrich. All solvents were anhydrous and stored in a nitrogen-filled glovebox unless otherwise specified.

Other Reagents

Sodium iodide and trifluoroacetic acid (TFA) were purchased from Sigma-Aldrich. 4,4''-Dimethyl-1,1'-biphenyl was purchased from Thermo Fisher Scientific. Other reagents, substrates, and solvents were purchased from commercial sources, stored on the benchtop, and used without further purification unless otherwise specified.

3.4.1.2 Methods

NMR Spectroscopy

¹H, ¹³C, and ¹⁹F NMR spectra were acquired on 400 and 500 MHz Bruker Avance III NMR instruments. NMR chemical shifts are reported in ppm. ¹H chemical shifts are referenced to tetramethylsilane (TMS) in CDCl₃ ($\delta = 0.00$ ppm). ¹³C and ¹⁹F chemical shifts were absolute referenced to the accompanying ¹H spectrum. Coupling constants (*J*) are reported in Hertz.

High Resolution Mass Spectrometry

Mass spectrometry data was collected on a Thermo Scientific Q Exactive Plus Hybrid Quadrupole-Orbitrap via flow injection with electrospray ionization by the Paul Bender Chemical Instrumentation Center facility at the University of Wisconsin-Madison.

Gas Chromatography

GC analyses were performed on an Agilent 7890A GC equipped with dual DB-5 columns (20 m × 180 μm × 0.18 μm), dual FID detectors, and H₂ as the carrier gas. A sample volume of 1 μL was injected at a temperature of 300 °C and a 100:1 split ratio. The initial inlet pressure was 20.3 psi but varied as the column flow was held constant at 1.8 mL/min for the duration of the run. The initial oven temperature of 50 °C was held for 0.46 min followed by a temperature ramp of 65 °C/min up to 300 °C. The total run time was 5.0 min and the FID temperature was 325 °C.

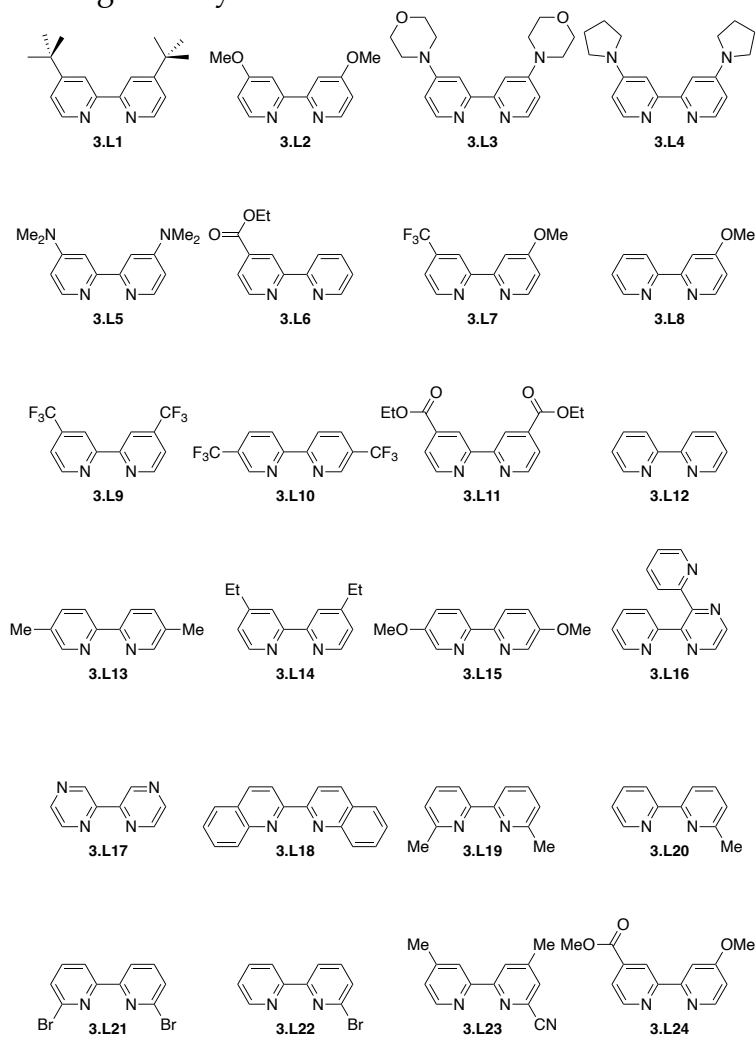
Flash Chromatography

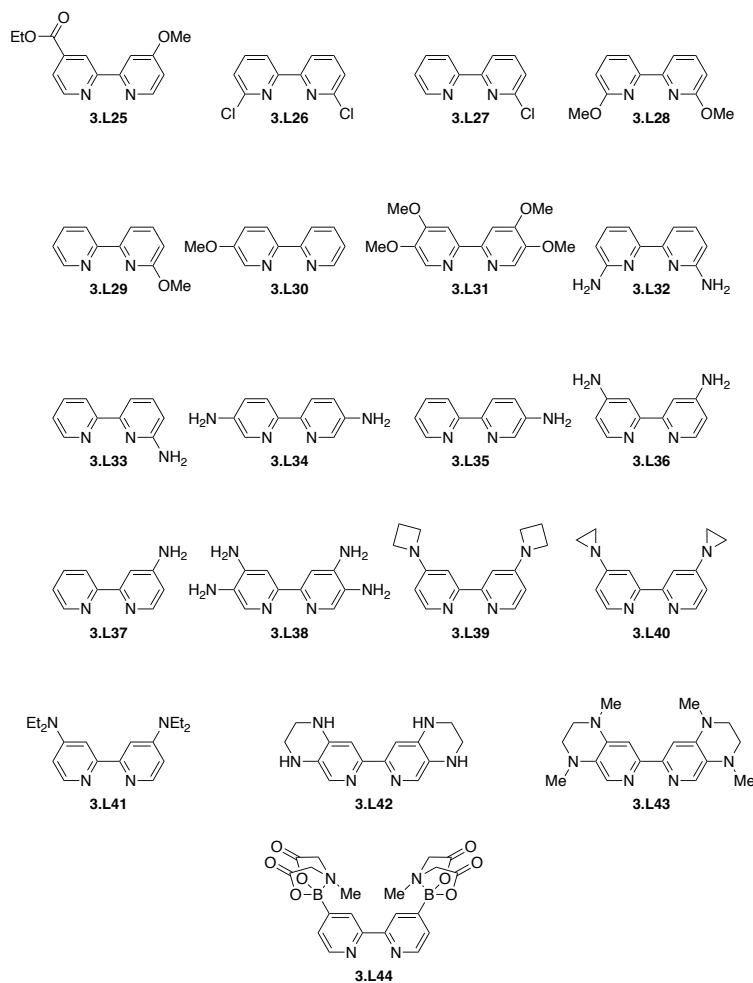
Flash chromatography was performed on a Teledyne ISCO Rf-200 (detection at 254 and 280 nm) equipped with an 80 g Teledyne ISCO Redisep Rf Gold silica gel column (20–40 μm particle size) or on a Biotage Isolera One (detection at 210 nm and 400 nm) equipped with a 25 g KPsil column (40–63 μm particle size). Products were visualized by UV.

3.4.2 Ligand Key and Preparation of Ligands

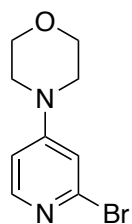
3.4.2.1 Ligand Key

Figure 3.1 Bipyridine Ligand Key





3.4.2.2 Preparation of Ligands



4-(2-bromopyridin-4-yl)morpholine (3.L3a)

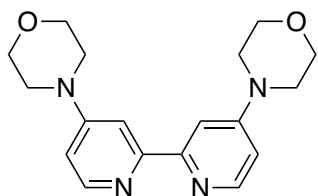
An oven-dried 1 dram vial equipped with a PTFE-coated stir bar was sealed with a phenolic screw cap bearing a PTFE-backed silicone septum. Using anhydrous technique, the vial was charged with 2-bromo-4-fluoropyridine (414.3 μ L, 704.0 mg, 4.000 mmol,

1.000 equiv), DMSO (1.5 mL), DIPEA (1034.0 mg, 8.0000 mmol, 2.0000 equiv), and morpholine (415.3 μ L, 418.2 mg, 4.800 mmol, 1.200 equiv). The reaction was stirred at 100 $^{\circ}$ C for 1 h, allowed to cool to rt, and poured over DI water (50 mL). The mixture was extracted with EtOAc (3 \times 30 mL). The combined organic layers were then washed with water (2 \times 100 mL) and brine (2 \times 100 mL) prior to being dried over Na₂SO₄, filtered, and concentrated to yield **3.L3a** (819.6 mg, 3.371 mmol, 84%) as an off-white solid.

¹H NMR (500 MHz, CDCl₃) δ 8.03 (d, *J* = 6.0 Hz, 1H), 6.82 (d, *J* = 2.4 Hz, 1H), 6.60 (dd, *J* = 6.0, 2.5 Hz, 1H), 3.86 – 3.80 (m, 4H), 3.32 – 3.26 (m, 4H).

¹³C{¹H} NMR (126 MHz, CDCl₃) δ 156.7, 150.0, 143.6, 111.2, 107.6, 77.2, 77.0, 76.7, 66.2, 46.1.

HRMS-ESI (*m/z*): [M+H]⁺ calcd for C₉H₁₂BrN₂O⁺, 243.0128; found, 243.0126.



4,4'-dimorpholino-2,2'-bipyridine (3.L3) was prepared by modification of the literature procedure.⁸⁸

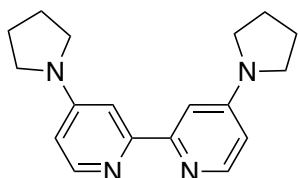
In a nitrogen-filled glovebox, an oven-dried 1 dram vial equipped with a PTFE-coated stir bar was charged with nickel(II) bromide dimethoxyethane (30.9 mg, 0.100 mmol, 0.100 equiv), 4,4'-bis(trifluoromethyl)-2,2'-bipyridine (29.2 mg, 0.100 mmol, 0.100 equiv), and DMF (1.000 mL). The vial was sealed with a phenolic screw cap bearing a PTFE-backed silicone septum and placed on a stir plate (1000 rpm, rt) for 20 min. After stirring the vial was unsealed, and 4-(2-bromopyridin-4-yl)morpholine (243.1 mg, 1.000 mmol,

1.000 equiv) was added, followed by manganese (164.8 mg, 3.000 mmol, 3.000 equiv). The vial was resealed, removed from the glovebox, and placed on a pre-heated stir plate where the contents were stirred (100 °C, 1000 rpm) for 24 h. After stirring, the reaction mixture was allowed to cool to rt and was poured over 100 mL of saturated Na₄EDTA solution. The mixture was stirred for 20 min. After stirring, the mixture was diluted with 50 mL of water and extracted with DCM (3 × 30 mL). The combined organic layers were dried over Na₂SO₄, filtered, and concentrated. The resulting residue was purified by column chromatography (80 g of silica gel, 1 CV of DCM, then 0–30% iPrOH/DCM across 25 CV) to yield **3.L3** (79.7 mg, 0.244 mmol, 49%) as a light brown solid.

¹H NMR (500 MHz, CDCl₃) δ 8.36 (d, *J* = 5.9 Hz, 1H), 7.89 (d, *J* = 2.6 Hz, 1H), 6.68 (dd, *J* = 5.9, 2.7 Hz, 1H), 3.91 – 3.79 (m, 4H), 3.41 (dd, *J* = 5.9, 4.0 Hz, 4H).

¹³C{¹H} NMR (126 MHz, CDCl₃) δ 157.1, 156.1, 149.6, 108.1, 105.6, 66.5, 46.4.

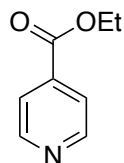
HRMS-ESI (*m/z*): [M+H]⁺ calcd for C₁₈H₂₃N₄O₂⁺, 327.1816; found, 327.1811.



4,4'-di(pyrrolidin-1-yl)-2,2'-bipyridine (3.L4) was synthesized according to the literature procedure and characterization data matched those reported in the literature.⁸⁹

¹H NMR (500 MHz, CDCl₃) δ 8.27 (d, *J* = 5.8 Hz, 2H), 7.54 (d, *J* = 2.5 Hz, 2H), 6.38 (dd, *J* = 5.8, 2.5 Hz, 2H), 3.49 – 3.30 (AA'XX', 8H), 2.07 – 1.97 (AA'XX', 8H).

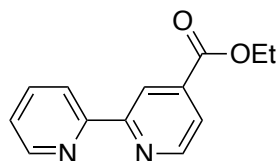
¹³C{¹H} NMR (126 MHz, CDCl₃) δ 156.9, 152.6, 148.9, 106.7, 104.3, 47.1, 25.4.



ethyl isonicotinate (3.L6a) was synthesized according to the literature procedure and characterization data matched those reported in the literature.⁹⁰

¹H NMR (500 MHz, CDCl₃) δ 8.78 (d, *J* = 4.5 Hz, 2H), 7.85 (d, *J* = 4.6 Hz, 2H), 4.42 (q, *J* = 7.2 Hz, 2H), 1.42 (t, *J* = 7.2 Hz, 2H).

¹³C{¹H} NMR (126 MHz, CDCl₃) δ 165.1, 150.6, 137.6, 122.8, 61.8, 14.2.

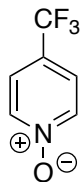


ethyl [2,2'-bipyridine]-4-carboxylate (3.L6) was synthesized according to the literature procedure and characterization data matched those reported in the literature.⁹¹

¹H NMR (500 MHz, CDCl₃) δ 8.93 (dd, *J* = 1.6, 0.9 Hz, 1H), 8.82 (dd, *J* = 4.9, 0.9 Hz, 1H), 8.73 (ddd, *J* = 4.7, 1.8, 0.9 Hz, 1H), 8.42 (dt, *J* = 8.0, 1.1 Hz, 1H), 7.88 (dd, *J* = 5.0, 1.6 Hz, 1H), 7.84 (td, *J* = 7.7, 1.8 Hz, 1H), 7.35 (ddd, *J* = 7.5, 4.8, 1.2 Hz, 1H), 4.46 (q, *J* = 7.1 Hz, 2H), 1.44 (t, *J* = 7.1 Hz, 3H).

¹³C{¹H} NMR (126 MHz, CDCl₃) δ 165.3, 157.3, 155.4, 149.9, 149.3, 138.9, 137.0, 124.1, 122.8, 121.3, 120.4, 61.8, 14.3.

HRMS-ESI (*m/z*): [M+H]⁺ calcd for C₁₃H₁₃N₂O₂⁺, 229.0972; found, 229.0969.

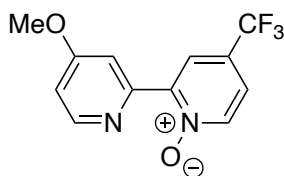


4-(trifluoromethyl)pyridine 1-oxide (3.L7a) was synthesized according to the literature procedure and characterization data matched those reported in the literature.⁹¹

¹H NMR (500 MHz, CDCl₃) δ 8.28 (d, *J* = 6.5 Hz, 2H), 7.51 (d, *J* = 6.6 Hz, 2H).

¹³C{¹H} NMR (126 MHz, CDCl₃) δ 139.8, 126.6 (q, *J* = 35.7 Hz), 123.0 (q, *J* = 3.7 Hz), 122.4 (q, *J* = 271.8 Hz).

¹⁹F{¹H} NMR (377 MHz, CDCl₃) δ -63.61.



4'-methoxy-4-(trifluoromethyl)-[2,2'-bipyridine] 1-oxide (3.L7b) was prepared by modification of the literature procedure.⁹¹

In a nitrogen-filled glovebox, 2 oven-dried 1 dram vials equipped with PTFE-coated stir bars were each charged with palladium(II) acetate (11.2 mg, 0.0500 mmol, 0.0500 equiv), 4-(trifluoromethyl)pyridine *N*-oxide (326.2 mg, 2.000 mmol, 2.000 equiv), potassium carbonate (276.4 mg, 2.000 mmol, 2.000 equiv), tri-*tert*-butylphosphine (12.1 mg, 0.0598 mmol, 0.0600 equiv, in 2 mL of toluene), and 2-bromo-4-methoxypyridine (188.0 mg, 1.000 mmol, 1.000 equiv). The vials were sealed with phenolic screw caps bearing PTFE-backed silicone septa and removed from the glovebox. The reactions were stirred at rt for 15 min, then at 100 °C overnight. The reactions were allowed to cool to rt, poured over a

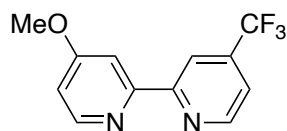
plug of Celite (pre-wetted with DCM), and further rinsed with DCM (50 mL). The combined filtrate was concentrated, and the resulting residue was purified by column chromatography (80 g of silica gel, 10% acetone/hexanes for 1 CV, then 10–40% acetone/hexanes across 20 CV) to yield **3.L7b** (262.5 mg, 0.9715 mmol, 50%) as a light tan solid.

$^1\text{H NMR}$ (500 MHz, CDCl_3) δ 8.62 (d, $J = 2.6$ Hz, 1H), 8.60 (d, $J = 2.8$ Hz, 1H), 8.55 (d, $J = 5.6$ Hz, 1H), 8.36 (d, $J = 6.9$ Hz, 1H), 7.46 (dd, $J = 6.9, 2.8$ Hz, 1H), 6.92 (dd, $J = 5.6, 2.5$ Hz, 1H), 3.93 (s, 3H).

$^{13}\text{C}\{^1\text{H}\}$ NMR (126 MHz, CDCl_3) δ 166.0, 150.4, 149.6, 147.7, 141.5, 126.8 (q, $J = 35.5$ Hz), 125.1 (q, $J = 3.9$ Hz), 122.6 (q, $J = 272.2$ Hz), 121.3 (q, $J = 3.5$ Hz), 111.4, 111.3, 55.4.

$^{19}\text{F}\{^1\text{H}\}$ NMR (377 MHz, CDCl_3) δ -63.56.

HRMS-ESI (m/z): $[\text{M}+\text{Na}]^+$ calcd for $\text{C}_{12}\text{H}_9\text{F}_3\text{N}_2\text{NaO}_2^+$, 293.0508; found, 293.0502.



4-methoxy-4'-(trifluoromethyl)-2,2'-bipyridine (3.L7) was prepared by modification of the literature procedure.⁹¹

A 100 mL three-neck flask equipped with a PTFE-coated stir bar was connected to a nitrogen manifold via a three-way adapter, the side necks were sealed with rubber septa. The flask was evacuated and backfilled with nitrogen three times. Under positive pressure of nitrogen, Pd/C (5 wt%) was added through the side neck (50.0 mg, 0.0235 mmol, 0.0470 equiv, in 15 mL of MeOH), and the vessel containing the Pd/C solution was washed with MeOH (5 mL) and the washings were added to the reaction flask. 4'-

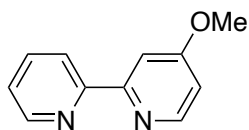
methoxy-4-(trifluoromethyl)-[2,2'-bipyridine] 1-oxide (135.1 mg, 0.5000 mmol, 1.000 equiv, in 15 mL of MeOH) was added to the flask, and a hydrogen balloon was connected to the top of the three-way adapter. The flask was evacuated and backfilled with nitrogen three times before it was evacuated once more and refilled with hydrogen from the balloon. The reaction was stirred at rt for 2 h. After the reaction was confirmed complete by TLC, the flask was evacuated and backfilled with nitrogen three times. The reaction mixture was poured over Celite—pre-wetted with MeOH—in a sintered funnel. The flask was rinsed with MeOH (2 × 50 mL), the rinse was added to the funnel, and the filter cake was rinsed with MeOH (50 mL, whilst avoiding drying the cake). The filtrate was concentrated under reduced pressure to yield **3.L7** (116.5 mg, 0.4583 mmol, 92%) as a brown solid.

¹H NMR (500 MHz, CDCl₃) δ 8.83 (d, *J* = 5.0 Hz, 1H), 8.69 (d, *J* = 2.0 Hz, 1H), 8.52 (d, *J* = 5.6 Hz, 1H), 8.02 (d, *J* = 2.6 Hz, 1H), 7.52 (dd, *J* = 5.0, 1.6 Hz, 1H), 6.89 (dd, *J* = 5.6, 2.6 Hz, 1H), 3.96 (s, 3H).

¹³C{¹H} NMR (126 MHz, CDCl₃) δ 166.8, 157.4, 156.5, 150.5, 149.9, 139.3 (q, *J* = 34.1 Hz), 123.0 (q, *J* = 273.3 Hz), 119.2 (q, *J* = 3.5 Hz), 117.1 (q, *J* = 3.7 Hz), 111.4, 106.5, 55.4.

¹⁹F{¹H} NMR (377 MHz, CDCl₃) δ -64.74.

HRMS-ESI (*m/z*): [M+H]⁺ calcd for C₁₂H₁₀F₃N₂O⁺, 255.0740; found, 255.0737.



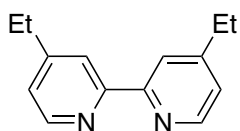
4-methoxy-2,2'-bipyridine (3.L8)

In a nitrogen-filled glovebox, an oven-dried 1 dram vial equipped with a PTFE-coated stir bar was charged with tris(dibenzylideneacetone)dipalladium(0) (27.5 mg, 0.0300 mmol, 0.0300 equiv), tri-*tert*-butylphosphine (20.2 mg, 0.100 mmol, 0.100 equiv), Tributyl(2-pyridyl)tin (405.0 mg, 1.100 mmol, 1.100 equiv), and 1,4-dioxane (3.000 mL). 2-Bromo-4-methoxypyridine (188.0 mg, 1.000 mmol, 1.000 equiv) was added to the vial prior to it being sealed with a phenolic screw cap bearing a PTFE-backed silicone septum. The vial was removed from the glovebox and placed on a pre-heated stir plate (90 °C, 1000 rpm), for 16 h. The reaction mixture was allowed to cool to rt and was poured over Celite—pre-wetted with DCM—in a sintered funnel, and the filter cake was rinsed with DCM (50 mL). The filtrate was then concentrated and purified by column chromatography (25 g of silica gel, 1 CV of 40% EtOAc/hexanes, then 40–80% EtOAc/hexanes across 20 CV) to yield **3.L8** (126.8 mg, 0.6809 mmol, 68%) as a white solid.

¹H NMR (500 MHz, CDCl₃) δ 8.68 (ddd, *J* = 4.9, 1.8, 1.0 Hz, 1H), 8.49 (d, *J* = 5.7 Hz, 1H), 8.40 (dt, *J* = 8.0, 1.1 Hz, 1H), 7.98 (d, *J* = 2.6 Hz, 1H), 7.81 (td, *J* = 7.7, 1.8 Hz, 1H), 7.31 (ddd, *J* = 7.5, 4.8, 1.2 Hz, 1H), 6.85 (dd, *J* = 5.6, 2.6 Hz, 1H), 3.96 (s, 3H).

¹³C{¹H} NMR (126 MHz, CDCl₃) δ 166.7, 158.1, 156.0, 150.3, 149.0, 136.9, 123.8, 121.3, 110.9, 106.0, 55.3.

HRMS-ESI (*m/z*): [M+H]⁺ calcd for C₁₁H₁₁N₂O⁺, 187.0866; found, 187.066.



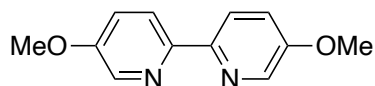
4,4'-diethyl-2,2'-bipyridine (3.L14) was obtained as a byproduct of the oxidative coupling of 4-ethylpyridine to form 4,4',4''-triethyl-2,2':6',2''-terpyridine. We recommend synthesis of **3.L14** via dimerization of 2-bromo-4-ethylpyridine.⁸⁸

In a nitrogen-filled glovebox, an oven-dried, 1 L, three-neck flask was charged with freshly distilled 4-ethylpyridine (40.00 g, 373.3 mmol, 1.000 equiv) and anhydrous DMA (200 mL). 10% Pd/C was added to the flask (5.36 g, 5.04 mmol, 0.0135 equiv), followed by manganese(IV) oxide (41.00 g, 471.6 mmol, 1.260 equiv). The flask was sealed and removed from the glovebox. On the bench, the flask was equipped with a reflux condenser, an internal thermometer, and an overhead stirrer via the three necks. The contents were placed under an argon atmosphere via an inlet at the top of the condenser. The contents were heated to reflux (162 °C) for 8 days. After the reaction was determined complete by TLC, the reaction mixture was allowed to cool to rt, diluted in DCM, and passed twice through a sintered glass funnel. The residue was washed with additional DCM until the washings were colorless. The filtrate and washings were combined, washed with DI water (2 × 400 mL), dried over MgSO₄, filtered, and concentrated. The resulting mixture was separated by vacuum distillation to yield 4-ethylpyridine (19 g, 177 mmol, bp 56 °C at 15 mmHg) and 4,4'-diethyl-2,2'-bipyridine (4.6 g, 22 mmol, obtained as a low-melting, light yellow solid, bp 130 °C at 0.5 mmHg). The pot residue was purified by sublimation (170–180 °C at 2.5 mmHg) to yield 4,4',4''-triethyl-2,2':6',2''-terpyridine.

¹H NMR (500 MHz, CDCl₃) δ 8.56 (dd, J = 4.9, 0.8 Hz, 2H), 8.25 (dd, J = 1.7, 0.8 Hz, 2H), 7.14 (dd, J = 5.0, 1.7 Hz, 2H), 2.73 (q, J = 7.6 Hz, 4H), 1.30 (t, J = 7.7 Hz, 6H).

¹³C{¹H} NMR (126 MHz, CDCl₃) δ 156.2, 154.0, 149.0, 123.3, 120.8, 28.4, 14.4.

HRMS-ESI (m/z): [M+H]⁺ calcd for C₁₄H₁₇N₂⁺, 213.1386; found, 213.1383.



5,5'-dimethoxy-2,2'-bipyridine (3.L15) was prepared by modification of the literature procedure.⁸⁸

In a nitrogen-filled glovebox, an oven-dried 1 dram vial equipped with a PTFE-coated stir bar was charged with nickel(II) chloride dimethoxyethane (30.0 mg, 0.137 mmol, 0.0500 equiv), 4,4'-bis(trifluoromethyl)-2,2'-bipyridine (47.9 mg, 0.164 mmol, 0.0600 equiv) and DMF (1.000 mL). The vial was sealed with a phenolic screw cap bearing a PTFE-backed silicone septum and placed on a stir plate, where it was stirred at rt for 20 min. After this time, the cap was removed and 2-bromo-5-methoxypyridine (510.4 mg, 0.2730 mmol, 1.000 equiv, in 800 μ L of DMF) was added, followed by manganese powder (300.0 mg, 5.460 mmol, 2.000 equiv). The vial was resealed with the screw cap and placed on a pre-heated stir plate (60 $^{\circ}$ C, 1000 rpm), where it was stirred overnight.

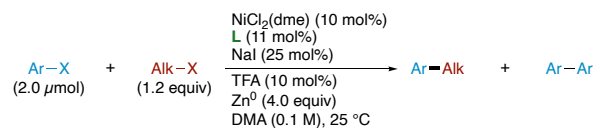
After stirring, the reaction mixture was transferred to an Erlenmeyer flask and diluted with a saturated solution of tetrasodium EDTA (100 mL). The mixture was stirred for 20 min before being transferred to a separatory funnel containing water (50 mL). The mixture was extracted with DCM (3 \times 50 mL). The combined organic layers were dried over Na₂SO₄, filtered, concentrated, and the resulting residue was purified by column chromatography (25 g of silica gel, 1 CV of 40% EtOAc/hexanes, then 40–80% EtOAc/hexanes across 15 CV) to yield **3.L15** (196.8 mg, 0.9101 mmol, 67%) as a white solid.

¹H NMR (500 MHz, CDCl₃) δ 8.33 (d, J = 2.9 Hz, 1H), 8.25 (d, J = 8.7 Hz, 1H), 7.30 (dd, J = 8.8, 3.0 Hz, 1H), 3.91 (s, 3H).

¹³C{¹H} NMR (126 MHz, CDCl₃) δ 155.5, 149.0, 136.6, 121.1, 120.9, 55.7.

3.4.3 General Procedures

3.4.3.1 General Procedure A: Evaluation of Ligands in High-Throughput Format



Stock solutions were prepared and stored in a nitrogen-filled glovebox. Separate stock solutions of nickel(II) chloride dimethoxyethane (48.3 mg, 0.220 mmol) and NaI (82.4 mg, 0.550 mmol) were each prepared in 5.5 mL of EtOH. A stock solution of aryl halide (0.200 M, 1.00 equiv), alkyl halide (0.240 M, 1.20 equiv), and 2,2'-dimethylbiphenyl (as an internal standard; 0.050 M, 0.25 equiv) were prepared in DMA. A 20.0 mM stock solution of TFA was prepared in DMA.

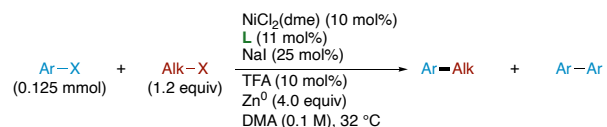
Stock ligand screening plates were prepared in a nitrogen-filled glovebox. A slurry of each ligand (110 μmol) was prepared in 2.5 mL of MeOH. While stirring, 50 μL (2.2 μmol) aliquots of each ligand slurry were taken and dispensed into the 1 mL wells of 96-well plates. The contents were heated uncovered overnight at 40 $^\circ\text{C}$ to evaporate the solvent. After this time, the plates were sealed and stored in a desiccator under inert atmosphere until needed for screening.

For screening, in a nitrogen-filled glovebox, each well of a pre-prepared 96-well plate—containing 2.2 μmol of the desired ligand—was charged with nickel(II) chloride dimethoxyethane (2.0 μmol , 0.10 equiv, in 50 μL of EtOH) and NaI (5.0 μmol , 0.25 equiv, in 50 μL of EtOH), evaporating the solvent after each addition. Zinc flake (5.2 mg, 80 μmol , 4.0 equiv) was dispensed into each well via a Mettler-Toledo QX96 solid handling robot, followed by a magnetic stir bar. Aryl halide (20.0 μmol , 1.00 equiv), alkyl halide

(24.0 μmol , 1.20 equiv), and 2,2'-dimethylbiphenyl (5.0 μmol , 0.25 equiv) were added as a solution in DMA (100 μL). Finally, TFA (2.0 μmol , 0.10 equiv, in 100 μL of DMA) was added to each vial. The plate was left uncovered and placed into a tumble stirrer, where it was stirred (250 rpm) at rt.

Aliquots were taken at 15, 30, 45, 60, 75, and 195 min to determine the concentrations of the product and side products, and at 24 h to establish the final yield. Each aliquot (15 μL) was obtained by sampling the stirring reactions of the 96-well plate with a 12-channel autopipette. Each aliquot was diluted into 750 μL of MeCN /DMSO (3:1), removed from the glovebox, and analyzed by UPLC. The concentrations of the starting materials, desired product, and aryl homodimer were determined as calibrated ratios of absorbances against the internal standard.

3.4.3.2 General Procedure B: Evaluation of Ligands in 1-Dram Vials



Stock solutions were prepared in a nitrogen-filled glovebox. A stock solution of nickel(II) chloride dimethoxyethane (274.6 mg, 1.250 mmol) in DMA was prepared in an oven-dried 25 mL volumetric flask. This solution was stored in a sealed 20 mL vial in the glovebox and stirred immediately prior to use. A stock solution of 4,4'-dimethylbiphenyl (1500.0 mg, 8.2300 mmol), aryl halide (12.500 mmol), and alkyl halide (15.000 mmol) in DMA was prepared in an oven-dried 25 mL volumetric flask. This solution was stored in a sealed 20 mL vial in the glovebox and stirred immediately prior to use. Additionally, separate stock solutions of sodium iodide (183.6 mg, 1.225 mmol) and TFA (57.0 mg, 0.500

mmol) in DMA were prepared in oven-dried 5 mL volumetric flasks. These solutions were prepared fresh each time screening was performed.

In a nitrogen-filled glovebox, an oven-dried 1 dram vial equipped with a PTFE-coated stir bar was charged with the ligand (0.014 mmol, 0.11 equiv), nickel(II) chloride dimethoxyethane (2.70 mg, 0.0125 mmol, 0.100 equiv, in 250 μ L DMA), and DMA (500 μ L). The vial was then sealed with a phenolic screw cap bearing a PTFE-backed silicone septum and placed on a stir plate, where it was stirred (1000 rpm) at 30 $^{\circ}$ C for 30 min. After this time, the cap was removed and sodium iodide (4.70 mg, 0.0313 mmol, 0.250 equiv, in 125 μ L of DMA) was added, followed by a mixture of: aryl halide (0.125 mmol, 1.00 equiv); alkyl halide (0.150 mmol, 1.20 equiv); and 4,4'-dimethylbiphenyl (as an internal standard; 15.0 mg, 0.0823 mmol, 0.658 equiv, in 250 μ L of DMA). Zinc flake (32.7 mg, 0.500 mmol, 4.00 equiv) was added to the vial. The contents of the vial were briefly swirled to incorporate the zinc and TFA (1.40 mg, 0.0125 mmol, 0.100 equiv, in 125 μ L of DMA) was added. The vial was resealed with the screw cap and placed on a pre-heated stir plate, where it was stirred (1000 rpm) at 32 $^{\circ}$ C.

Aliquots were taken at 0, 15, 30, 45, 60, 75, 90, 120, and 180 min to determine the concentrations of the product and side products, and at 24 h to establish the final yield. The aliquot (20 μ L) was obtained by removing the screw cap and sampling the stirring reaction with an autopipette. The aliquot was diluted into 1000 μ L of ethyl acetate, removed from the glovebox, and quenched with 1 mL of deionized water. The organic layer was then passed through a short (1.5 cm in a pipette) silica plug and analyzed by GC-FID. Concentrations of the reactants, desired product, and side products were determined as calibrated ratios of the area of the analyte peak compared to the area of the internal standard peak.

3.4.4 Results of Ligand Screens

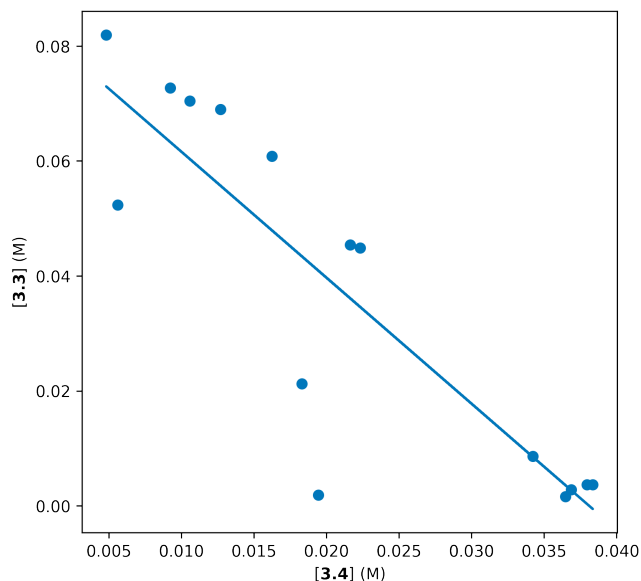
3.4.4.1 High-Throughput Ligand Screens

Figure 3.2 Results of High Throughput Ligand Screening^{ab}

Ligand	3.3 (%)	3.4 (%)	$\Delta\Delta G^\ddagger$
3.L1	61	16	-0.78
3.L2	82	5	-1.68
3.L9	4	38	1.39
3.L10	3	37	1.52
3.L11	4	38	1.38
3.L12	45	22	-0.41
3.L13	45	22	-0.44
3.L14	69	13	-1.00
3.L16	73	9	-1.22
3.L17	52	6	-1.32
3.L18	21	18	-0.09
3.L19	2	19	1.38
3.L20	2	36	1.84
3.L22	9	34	0.82
3.L23	70	11	-1.12

^aGeneral Procedure A was followed using ethyl 4-bromobenzoate and 1-bromo-3-phenylpropane.

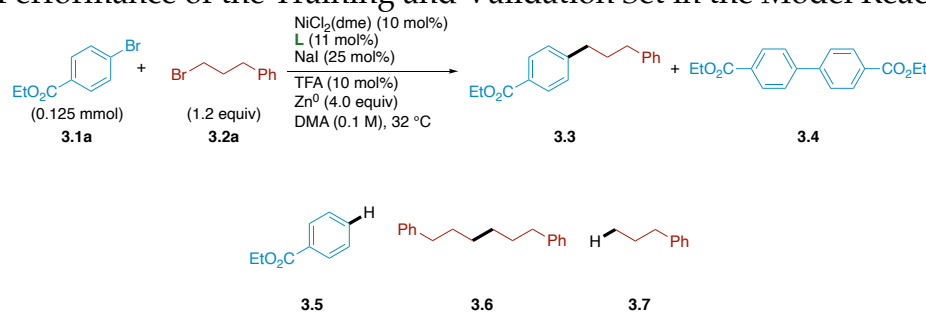
Figure 3.3 Correlation Between Concentration of 3.3 and 3.4



The yield of the desired product, **3.3**, is determined primarily by the selectivity for **3.3** over the aryl homodimer **3.4**. Notable exceptions include **3.L19**, which experienced catalyst deactivation—we observed remaining **3.1a**—and ligands based on *N*-heterocycles other than pyridine (**3.L18**, *vide supra*). Together, these results demonstrate that modelling for selectivity of **3.3** over **3.4** is a valid way to improve the efficiency and utility of C(sp²)-C(sp³) cross-electrophile coupling.

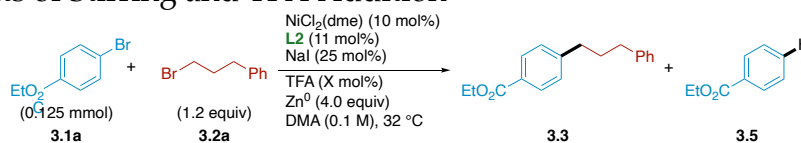
3.4.4.2 Focused Ligand Screens

Figure 3.4 Performance of the Training and Validation Set in the Model Reaction^{ab}



Ligand	3.3 (%)	3.4 (%)	$\Delta\Delta G^\ddagger$
3.L1	49	21	-0.50
3.L2	61	9	-1.19
3.L3	82	4	<i>-1.91</i>
3.L4	88	4	<i>-1.95</i>
3.L5	79	2	<i>-2.22</i>
3.L6	13	25	0.39
3.L7	13	38	0.66
3.L8	40	16	-0.56
3.L9	11	25	0.49
3.L11	14	27	0.41
3.L12	34	25	-0.18
3.L14	53	14	-0.83
3.L15	47	20	<i>-0.51</i>

^aReactions were set up according to General Procedure B using ethyl 4-bromobenzoate (28.6 mg, 0.125 mmol, 1.00 equiv) and 1-bromo-3-phenylpropane (30.0 mg, 0.150 mmol, 1.20 equiv). ^bNumbers in boldface were used for model training and numbers in italics were used for model validation.

Figure 3.5 Effects of Stirring and TFA Addition^a

Entry	X	Stir Rate (rpm)	3.3 (%)	3.5 (%)
1	10	1000	68	7
2	5	1000	63	10
3	0	1000	69	7
4	10	300	65	15
5	5	300	66	13
6	0	300	36	12

^aReactions were set up according by modification of General Procedure B using ethyl 4-bromobenzoate (28.6 mg, 0.125 mmol, 1.00 equiv), 1-bromo-3-phenylpropane (30.0 mg, 0.150 mmol, 1.20 equiv), and 4,4'-dimethoxybipyridine (**3.L2**) (3.0 mg, 0.014 mmol, 0.11 equiv). For reactions using 5 or 0 mol% of TFA, additional DMA was added to maintain a consistent reaction volume.

The differences in selectivity and yield between the high-throughput and focused ligand screens are due to formation of the dibrominated product (**3.5**) in the focused ligand screens. We considered that the change in stirring method—from tumble stirring to traditional magnetic stir bars—may mechanically activate the zinc, encouraging the formation of an organozinc. While less likely, we also considered direct protodemetalation of (L)Ni^{II}(Ar)Br by residual TFA. We found that slower stir rates had little effect on either the rate or yield of the model reaction with **3.L2** in the presence of TFA. Only when TFA was omitted did the stir rate impact the rate and yield of the reaction. These results suggest that another mechanism is responsible for the formation of **3.5**. Notably, we found that the majority of **3.5** forms between the 3 and 24 h timepoints, when the majority of the productive coupling has already taken place.

Figure 3.6 Benchmarking of Improved Bipyridines in the Coupling of Aryl Halides with Alkyl Bromides^a



Entry	X	L	3.3 (%)	Selectivity (3.3:3.4)
1	Cl	3.L2	85	17:1
2	Cl	3.L5	93	311:1
3	Br	3.L2	61	7:1
4	Br	3.L5	79	39:1
5	I	3.L2	76	29:1
6	I	3.L5	87	96:1

^aGeneral Procedure B was followed using: ethyl 4-chlorobenzoate (23.1 mg, 0.125 mmol, 1.00 equiv, Entries 1 and 2), ethyl 4-bromobenzoate (28.6 mg, 0.125 mmol, 1.00 equiv, Entries 3 and 4), or ethyl 4-iodobenzoate (34.5 mg, 0.125 mmol, 1.00 equiv, Entries 5 and 6); 1-bromo-3-phenylpropane (30.0 mg, 0.150 mmol, 1.20 equiv); and 4,4'-dimethoxybipyridine (**3.L2**) (3.0 mg, 0.014 mmol, 0.11 equiv, Entries 1, 3, and 5) or 4,4'-bis(dimethylamino)-2,2'-bipyridine (**3.L5**), (3.3 mg, 0.014 mmol, 0.11 equiv, Entries 2, 4, and 6). Reactions were stirred for 24 h prior to sampling.

These results demonstrate a general increase in selectivity when employing **3.L5** in place of **3.L2**. The shift in selectivity trends when coupling ethyl 4-iodobenzoate may be due to a shift in mechanism or due to significant acceleration of alkyl radical formation in the presence of stoichiometric iodide salt byproducts.

Figure 3.7 Decreasing Catalyst Loading Increases Selectivity^a



Entry	X mol%	L	3.3 (%)	Selectivity (3.3: 3.4)
1	10	3.L2	85	17:1
2	10	3.L5	93	311:1
3	5	3.L2	89	25:1
4	5	3.L5	96	364:1

^aReactions were performed by modification of General Procedure B, using ethyl 4-chlorobenzoate (23.1 mg, 0.125 mmol, 1.00 equiv), 1-bromo-3-phenylpropane (30.0 mg, 0.150 mmol, 1.20 equiv), and either 4,4'-dimethoxybipyridine (**3.L2**)—(3.0 mg, 0.014 mmol, 0.11 equiv, Entry 1) or (1.5 mg, 6.9 μmol, 0.055 equiv, Entry 3)—or 4,4'-bis(dimethylamino)-2,2'-bipyridine (**3.L5**)—(3.3 mg, 0.014 mmol, 0.11 equiv, Entry 2) or (1.8 mg, 6.9 μmol, 0.055 equiv, Entry 4). For reactions with 5 mol% loading of NiCl₂(dme) (Entries 3 and 4), 125 μL of NiCl₂(dme) stock solution was used and an additional 125 μL of DMA was added to maintain a consistent reaction volume. Reactions were stirred for 24 h prior to sampling.

These results demonstrate that further improvements in selectivity and efficiency may be achieved by decreasing the concentration of the catalyst. This improvement is consistent with similar observations in the coupling of (*Z*)-vinyl bromides and supports a mechanism of biaryl formation involving either disproportionation or ligand transfer between two nickel centers.⁹² Based on other observed electronic and steric trends, we hypothesize that aryl homodimerization occurs via disproportionation of (L)Ni^I(Ar) or ligand transfer between (L)Ni^I(Ar) and (L)Ni^{II}(Ar)Br.

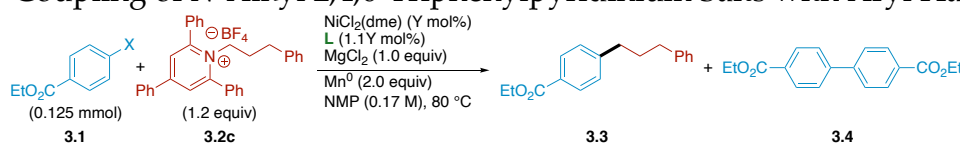
Reactions set up with significantly lower catalyst loadings (<1 mol%) gave low conversion of the aryl halide. We hypothesize that issues with catalyst speciation and initiation, or competitive zinc insertion may be the cause. Previous reports employing pre-ligated (L)Ni^{II}I₂ and manganese did not appear to encounter these issues.⁹² We hypothesize that these solutions could be combined with application of **3.L5** to yield further increases in selectivity.

Figure 3.8 Coupling of Aryl and Alkyl Chlorides^a

Entry	L	Salt	X mol%	3.3 (%)	Selectivity (3.3 : 3.4)
1	3.L2	NaI	25	11	0.5:1
2	3.L5	NaI	25	25	2:1
3	3.L5	NaI	50	40	7:1
4	3.L1	NaI	100	2	0.003:1
5	3.L2	NaI	100	16	0.2:1
6	3.L5	NaI	100	52	14:1
7	3.L1	NaI	200	3	0.007:1
8	3.L2	NaI	200	21	0.5:1
9	3.L5	NaI	200	55	19:1
10	3.L5	LiI	50	52	12:1
11	3.L1	LiI	100	4	0.009:1
12	3.L2	LiI	100	11	0.1:1
13	3.L5	LiI	100	62	25:1
14	3.L1	LiI	200	3	0.006:1
15	3.L2	LiI	200	30	1:1
16	3.L5	LiI	200	51	15:1

^aReactions were set up by modification of General Procedure B using ethyl 4-chlorobenzoate (23.1 mg, 0.125 mmol, 1.00 equiv), 1-chloro-3-phenylpropane (23.2 mg, 0.150 mmol, 1.20 equiv), and either, 4,4'-di-*tert*-butyl-2,2'-bipyridine (**3.L1**) (3.7 mg, 0.014 mmol, 0.11 equiv, Entries 4, 7, 11, and 14), 4,4'-dimethoxybipyridine (**3.L2**) (3.0 mg, 0.014 mmol, 0.11 equiv, Entries 1, 5, 8, 12, and 15) or 4,4'-bis(dimethylamino)-2,2'-bipyridine (**3.L5**) (3.3 mg, 0.014 mmol, 0.11 equiv, Entries 2, 3, 6, 9, 10, 13, and 16). All reactions were set up by adding solid LiI or NaI directly to the precatalyst solution along with an additional 125 μ L of DMA. The mixture was then stirred at rt until the salt was dissolved prior to starting materials being added. Reactions were stirred for 24 h prior to sampling.

These results demonstrate that when alkyl radical formation is slow, **3.L5** offers improvements in selectivity over the previous state-of-the-art ligand **3.L3**. The increased stability of (**3.L5**)Ni^{II}(Ar)Cl provides sufficient intermediate lifetime to enable generally selective reactions without the formation of significant amounts of **3.4**. While the use of increased amounts of LiI (>2.00 equiv) may enable the use of **3.L3** with similar yields and selectivity, this would decrease the overall mass efficiency of the reaction.

Figure 3.9 Coupling of *N*-Alkyl 2,4,6-Triphenylpyridinium Salts with Aryl Halides

Entry	L	X	Y mol%	3.3 (%)	Selectivity (3.3:3.4)
1	3.L5	Br	10	98	84:1
2	3.L5	Cl	10	55	7:1
3	3.L5	Cl	20	86	8:1
4	3.L1	Cl	20	65	5:1
5	3.L2	Cl	20	49	3:1

Reactions were set up by modification of the literature procedure.⁸⁶ In a nitrogen-filled glovebox, 5 oven-dried 1 dram vials equipped with PTFE-coated stir bars were charged with 4,4'-bis(dimethylamino)-2,2'-bipyridine (**3.L5**)—(3.3 mg, 0.014 mmol, 0.11 equiv, Entries 1 and 2) or (6.7 mg, 0.028 mmol, 0.22 equiv, Entry 3)—4,4'-di-*tert*-butyl-2,2'-bipyridine (**3.L1**) (7.4 mg, 0.028 mmol, 0.22 equiv, Entry 4), or 4,4'-dimethoxybipyridine (**3.L2**) (6.0 mg, 0.028 mmol, 0.22 equiv, Entry 5); nickel(II) chloride dimethoxyethane—(2.7 mg, 0.0125 mmol, 0.10 equiv, Entries 1 and 2) or (5.5 mg, 0.025 mmol, 0.20 equiv, Entries 3–5)—4,4'-dimethylbiphenyl (as an internal standard; 15.0 mg, 0.0823 mmol, 0.658 equiv), magnesium(II) chloride (11.9 mg, .125 mmol, 1.00 equiv), manganese powder (13.7 mg, 0.250 mmol, 2.00 equiv), and 2,4,6-triphenyl-1-(3-phenylpropyl)-pyridin-1-ium tetrafluoroborate (77.0 mg, .150 mmol, 1.20 equiv). NMP (735 μ L) was added to each vial, followed by the appropriate aryl halide—either ethyl 4-bromobenzoate (28.6 mg, 0.125 mmol, 1.00 equiv, Entry 1) or ethyl 4-chlorobenzoate (23.1 mg, 0.125 mmol, 1.00 equiv, Entries 2 and 3). The vials were sealed with phenolic screw caps bearing PTFE-backed silicone septa, removed from the glovebox, and placed on a pre-heated stir plate (80 °C, 1000 rpm) for 24 h. An aliquot (20 μ L) was taken from each reaction via gas-tight syringe. The aliquots were diluted into 1000 μ L of ethyl acetate and quenched with 1 mL of deionized water. The organic layers were then passed through

short (1.5 cm in a pipette) silica plugs and analyzed by GC-FID. Concentrations of the reactants, desired product, and side products were determined as calibrated ratios of the area of the analyte peak compared to the area of the internal standard peak.

These results demonstrate that **3.L5** also offers benefits in existing reactions (Entry 1) and new combinations of substrates (Entries 2 and 3). The observed improvements when increasing the catalyst loading from 10 to 20 mol% suggest that selectivity and yield are governed by the rate of oxidative addition to the chloroarene. Radical formation from **3.2c** most likely proceeds via direct reduction by manganese and fragmentation of the resulting radical anion.⁹³ As such, the stability of (L)Ni^{II}(Ar)X most likely plays a small role in the overall selectivity of the reaction compared to the rate of formation of (L)Ni^{II}(Ar)X. Compared to the other reactions in our work, the alkyl radical precursor is the more reactive of the two substrates and generating sufficient (L)Ni^{II}(Ar)X to capture the resulting alkyl radical is critical to providing high yield and selectivity. We hypothesize that the formation of **3.4** occurs after the complete consumption of **3.1**.

3.4.5 Computational Details

3.4.5.1 General Computational Method

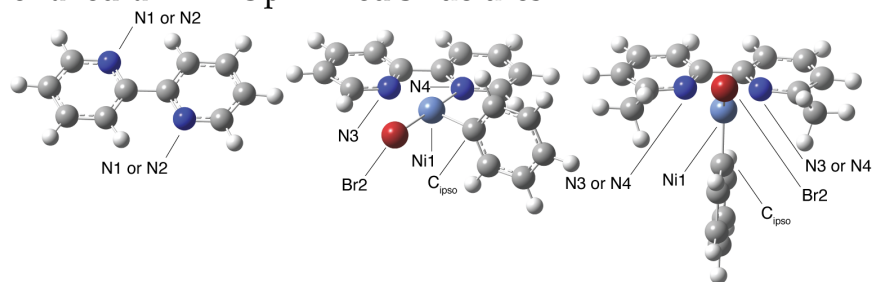
All computations were performed using the Gaussian 16, Rev. C.01 suite using defaults unless noted otherwise.⁵¹ Optimized structures are visualized using GaussView 6.0.10.⁵² The “ultrafine” integration grid setting was used in all computations. Each structure was calculated by performing geometry optimizations with the unrestricted M06 functional⁵⁴ and the cc-pVDZ basis set,^{55,56} as well as the LANL2DZ effective core potential⁵⁷ for Ni. The frequency keyword “noraman” was used in all frequency calculations to increase computational efficiency. Gas phase single point energies were obtained using UM06/cc-

pVTZ, SDD (Ni).⁵⁸ Corrections for the solvation energies were obtained from the difference between single points with the SMD continuum solvation model for DMA (*N,N*-dimethylacetamide)⁵⁹ and a gas phase single point, both using UM06/cc-pVTZ, SDD (Ni). Conformers of higher energy were accounted for in all cases and are not included in the discussion. Stationary points were characterized as ground states by the absence of negative eigenvalues (zero imaginary frequencies) in frequency analysis at the same level of theory as the geometry optimization.

3.4.5.2 Descriptors and Guide to Parameter Spreadsheet

Descriptors were collected from DFT output files using Python scripts created by the Sigman Group (University of Utah). An explanation of each of the descriptor categories is enumerated below. To account for common nickel(II) coordination geometries, square planar singlet and tetrahedral triplet geometries were considered, as well as the unbound ligand in the absence of a metal. We performed a manual conformational search to identify the lowest energy structure, and descriptor values for each of the coordination geometries and free ligand were generated. Descriptors associated with the square planar (L)Ni^{II}(Ph)Br structures are denoted with the suffix “.sqpl”, and those associated with the tetrahedral structures have the suffix “.tet” appended. We also considered using parameters from the overall lowest energy conformer, denoted “.lowestgeom”, a weighted average of the two conformers based on the energies of the square planar singlet and tetrahedral triplet geometries at 25 °C, denoted “.boltz”, and unbound ligand optimizations, denoted with the suffix “.free”. All computed data is associated with the parent ligand common in each structure. For a full list of computed parameter values, see the Excel spreadsheet included in the supplemental information. A guide to the parameter list is included below, with column references to the parameter library.

Figure 3.10 Atom Numbering Scheme for Free Ligand, (L)Ni(Ph)Br Square Planar, and (L)Ni(Ph)Br Tetrahedral DFT-Optimized Structures



Atom numbering was conserved for atoms common and relevant to all square planar structures, namely Ni1, Br2, N3 (binding nitrogen always trans to the phenyl ligand), N4 (binding nitrogen always trans to the bromine ligand), and C5 (C_{ipso} of the phenyl ligand). For tetrahedral geometries, Ni1, Br2, and C5 were conserved across all structures, and an attempt was made to maintain consistency in the numbering scheme (relative to the analogous square planar geometries) for N3 and N4, especially for the non-symmetric bipyridine ligands. For the unbound ligand, the donor nitrogens are numbered N1 and N2; no attempt was made to standardize atom numbering beyond the donor atoms, as we did not have a numbering schema in place at the time these geometries were computed.

Figure 3.11 Guide to Parameter Spreadsheet

Descriptor	Column
<i>General Information</i>	
Manuscript ligand label (L)	A
Internal ligand number (for authors' use)	B
Ligand name	C
CAS registry number	D
Net charge	E
<i>Structural Information</i>	
Substitution pattern	F
LXZ notation	G
<i>Thermochemistry</i>	
Free ligand thermochemistry in Hartrees	H-Q
Square planar thermochemistry in Hartrees	AT-BC
Tetrahedral thermochemistry in Hartrees	DU-ED

Difference in TZ solvated SP energies of (L)Ni(Ph)Br complexes, AS
E(Tetrahedral) – E(Square Planar) in kcal/mol

Computed Structural Information

Relevant distances for catalyst structural features of interest common to every computed catalyst structure were gathered from the Gaussian output and are provided in Angstroms (Å) or degrees (°).

Ni1–Br2 distance	BQ, ER, HI, JZ
Ni1–N3 distance	BR, ES, HJ, KA
Ni1–N4 distance	BS, ET, HK, KB
Ni1–C _{ipso} distance	BT, EU, HL, KC
N3–Ni1–N4 bite angle	BU, EV, HM, KD
Br2–Ni1–C _{ipso} ancillary ligand angle	BV, EW, HN, KE
Plane angle between the planes defined by N3–Ni1–N4 and Br2–Ni1–C _{ipso}	BW, EX, HO, KF

Descriptors

Dipole moment	R, BD, EE, GV, JM
Energy of the HOMO in Hartrees	S, BE, EF, GW, JN
Energy of the LUMO in Hartrees	T, BF, EG, GX, JO
Difference between HOMO and LUMO energies in Hartrees	U, BG, EH, GY, JP
μ (μ) is the average of the HOMO and LUMO energies, and describes the chemical potential ⁹⁴	V, BH, EI, GZ, JQ
η (η) is half of the difference between the HOMO and LUMO energies, and provides information about the hardness of a molecule ⁹⁵	W, BI, EJ, HA, JR
ω (ω) is the square of μ divided by two times η , and describes the electrophilicity index ⁹⁵	X, BJ, EK, HB, JS
The quadrupole moment is a tensor, whereas the amplitude is a scalar value. xx component of quadrupole moment	Y, BK, EL, HC, JT

yy component of quadrupole moment	Z, BL, EM, HD, JU
zz component of quadrupole moment quadrupole amplitude	AB, BN, EO, HF, JW
Isotropic polarizability in Debye	AC, BO, EP, HG, JX
Anisotropic polarizability in Debye	AD, BP, EQ, HH, JY
The energies and occupancies of the d-orbitals of nickel are provided for each d-orbital.	
d_{xy} occupancy	BX, EY, HP, KG
d_{xy} energy	BY, EZ, HQ, KH
d_{xz} occupancy	BZ, FA, HR, KI
d_{xz} energy	CA, FB, HS, KJ
d_{yz} occupancy	CB, FC, HT, KK
d_{yz} energy	CC, FD, HU, KL
$d_{x^2-y^2}$ occupancy	CD, FE, HV, KM
$d_{x^2-y^2}$ energy	CE, FF, HW, KN
d_{z^2} occupancy	CF, FG, HX, KO
d_{z^2} energy	CG, FH, HY, KP
Partial charges according to natural population analysis (NPA) were obtained with the NBO 7.0 ⁵³ module within Gaussian. To obtain a more holistic picture of the ligand impact on the nickel center, the average, minimum, maximum, and range of the NPA charges for the two ligated nitrogens (N3 and N4) were also tabulated.	
NPA _{N1} (free ligand)	AE
NPA _{N2} (free ligand)	AF
Average of the charges of NPA _{N1} and NPA _{N2} (free ligand)	AG
Minimum of the charges of NPA _{N1} and NPA _{N2} (free ligand)	AH
Maximum of the charges of NPA _{N1} and NPA _{N2} (free ligand)	AI
Range of the charges of NPA _{N1} and NPA _{N2} (free ligand)	AJ
NPA _{Ni1}	CH, FI, HZ, KQ

NPA_{Br2}	CI, FJ, IA, KR
NPA_{N3}	CJ, FK, IB, KS
NPA_{N4}	CK, FL, IC, KT
$NPA_{C_{ipso}}$	CL, FM, ID, KU
Average of the charges of NPA_{N3} and NPA_{N4}	CM, FN, IE, KV
Minimum of the charges of NPA_{N3} and NPA_{N4}	CN, FO, IF, KW
Maximum of the charges of NPA_{N3} and NPA_{N4}	CO, FP, IG, KX
Range of the charges of NPA_{N3} and NPA_{N4}	CP, FQ, IH, KY
NMR shifts are commonly represented isotropically, but can also be represented as the eigenvalues of the NMR anisotropic shielding tensor. Both the isotropic and anisotropic NMR shifts for nickel are omitted due to the use of an effective core potential.	
Isotropic NMR shift of N1 (free ligand)	AK
Isotropic NMR shift of N2 (free ligand)	AL
xx component of anisotropic NMR shift of N1 (free ligand)	AM
yy component of anisotropic NMR shift of N1 (free ligand)	AN
zz component of anisotropic NMR shift of N1 (free ligand)	AO
xx component of anisotropic NMR shift of N2 (free ligand)	AP
yy component of anisotropic NMR shift of N2 (free ligand)	AQ
zz component of anisotropic NMR shift of N2 (free ligand)	AR
Isotropic NMR shift of Br2	CQ, FR, II, KZ
Isotropic NMR shift of N3	CR, FS, IJ, LA
Isotropic NMR shift of N4	CS, FT, IK, LB
Isotropic NMR shift of C_{ipso}	CT, FU, IL, LC
xx component of anisotropic NMR shift of Br2	CU, FV, IM, LC
yy component of anisotropic NMR shift of Br2	CV, FW, IN, LE
zz component of anisotropic NMR shift of Br2	CW, FX, IO, LF
xx component of anisotropic NMR shift of N3	CX, FY, IP, LG
yy component of anisotropic NMR shift of N3	CY, FZ, IQ, LH

zz component of anisotropic NMR shift of N3	CZ, GA, IR, LI
xx component of anisotropic NMR shift of N4	DA, GB, IS, LJ
yy component of anisotropic NMR shift of N4	DB, GC, IT, LK
zz component of anisotropic NMR shift of N4	DC, GD, IU, LL
xx component of anisotropic NMR shift of C _{ipso}	DD, GE, IV, LM
yy component of anisotropic NMR shift of C _{ipso}	DE, GF, IW, LN
zz component of anisotropic NMR shift of C _{ipso}	DF, GG, IX, LO

We hypothesized that the capture of an alkyl radical by (L)Ni^{II}(Ph)Br—the presumed selectivity determining step—may be impacted by the steric confinement of the primary coordination sphere of the nickel. As such, we collected percent buried volume (%V_{bur}) values at a range of 2.0–5.0 Å in 0.5 Å steps, to describe the steric confinement of the coordination sphere about nickel.^{96–98} The buried volume quantifies the occupation of a sphere of a set radius. %V_{bur} was determined for the [(L)Ni^{II}(Ph)Br] complex and for [(L)Ni^{II}]⁺²—generated by deletion of the Ph- and Br- ligands from the optimized structure.

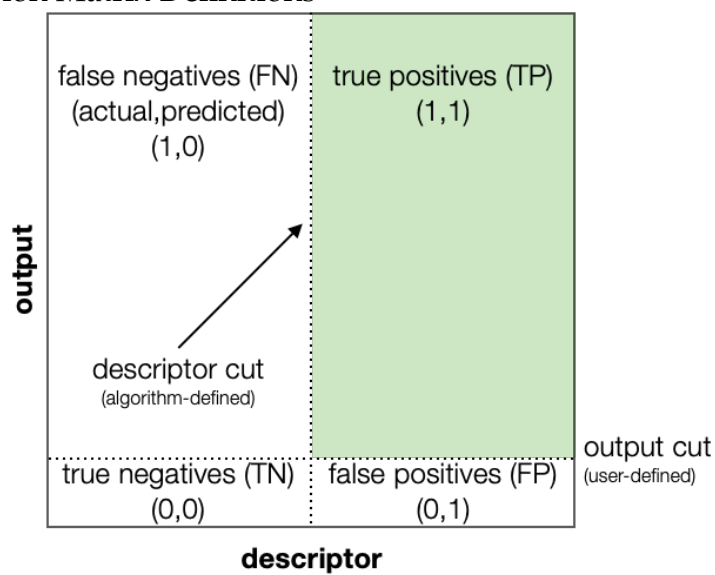
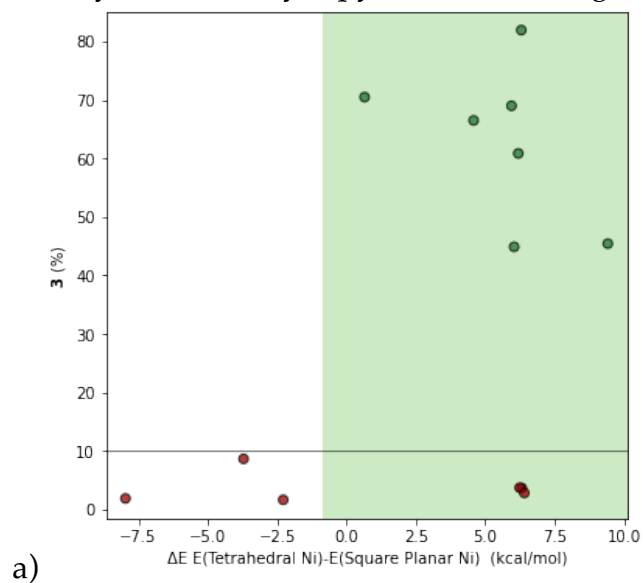
%V _{bur} with a 2.0 Å radius	DG, DN, GH, GO, IY, JF, LP, LW
%V _{bur} with a 2.5 Å radius	DH, DO, GI, GP, IZ, JG, LQ, LX
%V _{bur} with a 3.0 Å radius	DI, DP, GJ, GQ, JA, JH, LR, LY
%V _{bur} with a 3.5 Å radius	DJ, DQ, GK, GR, JB, JL, LS, LZ
%V _{bur} with a 4.0 Å radius	DK, DR, GL, GS, JC, JJ, LT, MA
%V _{bur} with a 4.5 Å radius	DL, DS, GM,

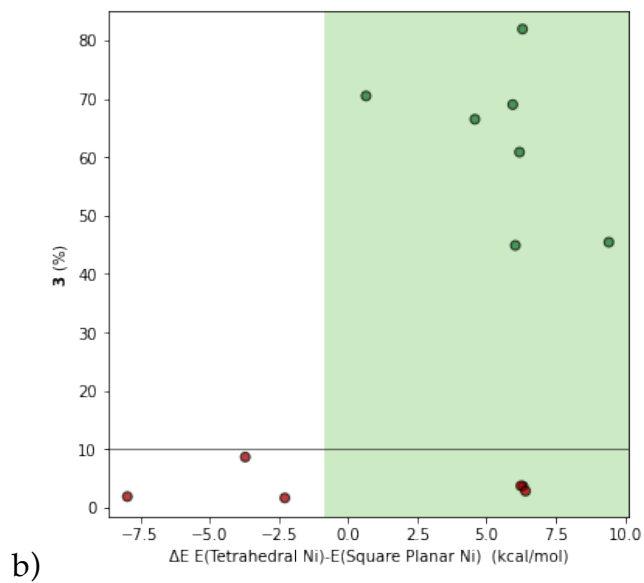
$\%V_{\text{bur}}$ with a 5.0 Å radius

GT, JD,
JK, LU,
MB
DM,
DT,
GN,
GU, JE,
JL, LV,
MC

3.4.5.3 Threshold Analysis

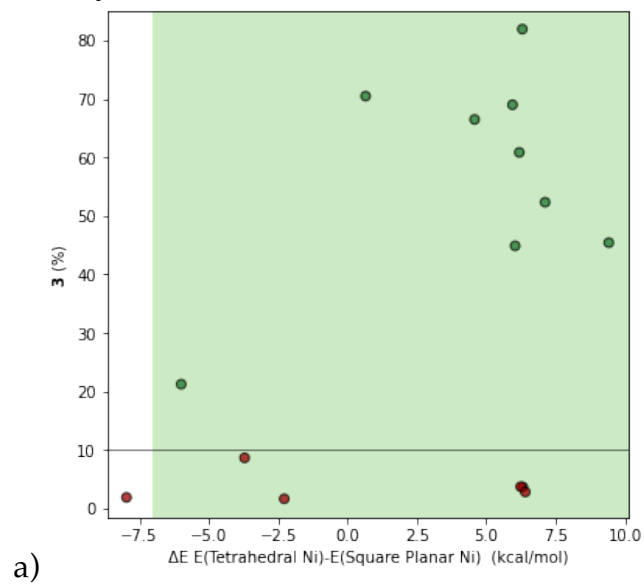
Threshold analysis was performed using the workflow and scripts and developed by the Sigman and Doyle groups.³¹ This method utilizes a single node decision tree to identify which, if any, descriptor value(s) that will accurately categorize outputs. The descriptors used for these analyses are those discussed in Section 3.4.5.2. The algorithm was performed using a plot step size of 0.02 and a y_{cut} of 10. The y_{cut} , or yield cutoff, was set based on the yield of one catalytic turnover for our system, which would be ~10% yield. From this y_{cut} , we are designating outputs below y_{cut} as having “inactive” catalysts, whilst outputs greater than y_{cut} will be considered to have “active” catalysts. Outputs are plotted in a 2x2 confusion matrix with the quadrants divided into true and false categorizations of positives and negatives, with the quadrant assignments taking the form of (actual, predicted). Outputs corresponding to yields < 10% (< y_{cut}) are depicted in red; conversely, outputs corresponding to yields \geq 10% ($\geq y_{\text{cut}}$) are depicted in green.

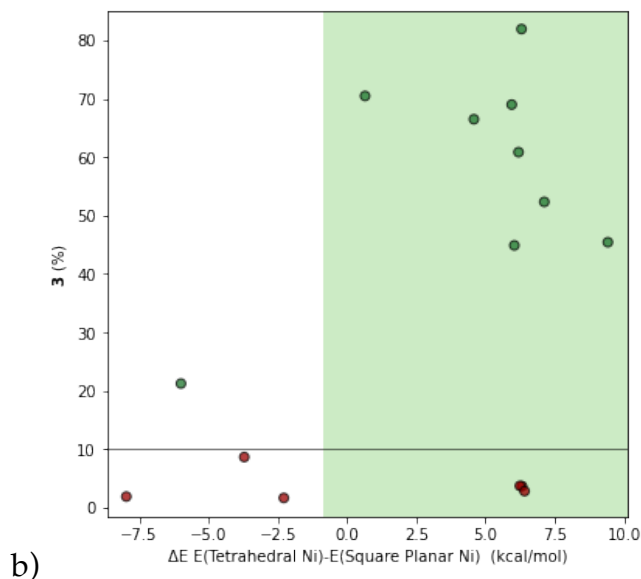
Figure 3.12 Confusion Matrix Definitions**Figure 3.13** Threshold Analysis with Only Bipyridine-Based Ligands



a) Threshold with `class_weight = {0:1,1:20}`. b) Threshold with `class_weight = 'balanced'`.

Figure 3.14 Threshold Analysis with Full HTE Dataset





a) Threshold with class_weight = {0:1,1:20}. b) Threshold with class_weight = 'balanced'.

Figure 3.15 Threshold ΔE Decision Value and Statistical Accuracy Metrics

Figure	Y_cut (% Yield)	Class Weight	Threshold (ΔE Tet-SqPl)	Accuracy	F1	MCC
3.12a	10	{0:1,1:20}	-0.81	0.77	0.82	0.59
3.12b	10	'balanced'	-0.81	0.77	0.82	0.59
3.13a	10	{0:1,1:20}	-6.98	0.67	0.78	0.33
3.13b	10	'balanced'	-0.81	0.73	0.80	0.43

Distortion in the square planar geometry leads to poor yield classification results for 6- and 6,6'-(di)substituted bipyridine derivatives using descriptors gathered from the square planar geometry. While occasional effective classification was observed—e.g., Ni-N3 square planar bond distance—these provide less direct mechanistic insight than ΔE (the tetrahedral/square planar energy gap).

For the ΔE descriptor, the use of 'balanced' class weighting in Figure 3.14b allows for a better threshold—at the same descriptor cutoff as in Figure 3.13a, as we have one observation classified as a false negative (cuproine, **3.L18**). The behavior of cuproine in this analysis prompted us to take a closer look at the timecourse data, where we observed that the aryl halide is being consumed in the first 75 min, but no product is formed. At

some point after the first 75 min, product is formed, but not with a commensurate amount of aryl homodimer. These observations suggest that this ligand promotes a different mechanism for the desired bond formation. We hypothesize that the extended π system promotes the formation of an arylzinc reagent, which then undergoes in situ Negishi cross-coupling with the alkyl halide. Based on these observations, we chose to remove this ligand from further analyses, along with 2,2'-bipyrazine—as it is also not a true 2,2'-bipyridine—for the sake of internal consistency.

The various confusion matrices with ΔE tell the same story, namely that substitution in the 6-position enforces a tetrahedral ground state and rapid dimerization of the aryl halide.

3.4.5.4 Parameterization Modeling Overview

In the parameterization modeling, variations of bidentate nitrogenous ligands, L, were considered in two formats: as the unbound ligand in the absence of a metal, and as a subset of the catalyst as the nickel(II) oxidative addition complex, (L)Ni(Ph)Br (see Figure 3.10 for representative computed structures that were parameterized for modeling). For the nickel complexes, the simplified aryl halide—bromobenzene—was utilized for consistency and breadth of applicability to other aryl halide systems whilst being representative of the model reaction system.

Reactions were run in duplicate, and the reported values are the average of the two runs at 24 h elapsed time.

Model Target

Selectivity was defined as the ratio of the averaged concentrations of cross-coupled product, [3.3], to aryl homodimer, [3.4], at 24 h, where each reaction was performed in

quadruplicate (high-throughput dataset) or duplicate (focused ligand screen dataset). The observed selectivity of each catalyst (Figure 3.2, Figure 3.4) was converted to relative free energies (with gas constant $R = 1.98588 \cdot 10^{-3}$ kcal/mol and temperature $T = 298.15$ K—for high-throughput ligand screens—or $T = 305.15$ K—for focused ligand screens) and used as the target in the subsequent modeling.

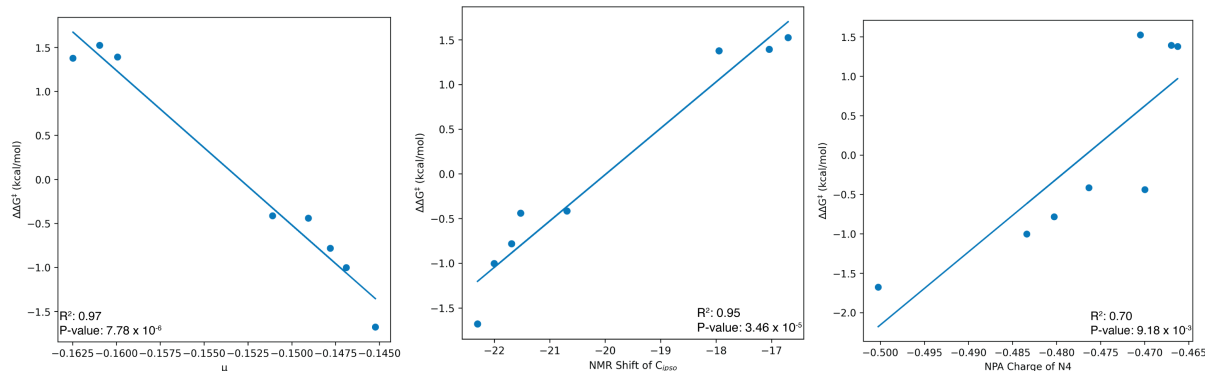
$$\Delta\Delta G^\ddagger = -RT \ln \left(\frac{[\mathbf{3.3}]}{[\mathbf{3.4}]} \right)$$

Modeling Workflow

Linear regression model development was performed using Python based on observations found from analysis of univariate correlations. Due to apparent changes in mechanism and byproduct distribution, ligands based on *N*-heterocycles other than pyridine were removed. The 1-parameter models were internally validated with leave-one-out (LOO) and *k*-fold ($k = 5$) cross-validation. The number of resulting univariate correlations was pruned to only consider significant correlations (p -value < 0.01). Each of the resulting correlations were used to predict the selectivity of 4 ligands (4,4'-dimorpholino-2,2'-bipyridine **3.L3**, 4,4'-di(pyrrolidin-1-yl)-2,2'-bipyridine **3.L4**, 4,4'-bis(dimethylamino)-2,2'-bipyridine **3.L5**, and 5,5'-dimethoxy-2,2'-bipyridine **3.L15**) for which we did not have any prior experimental observations; these four validation samples served as an external validation of our predictions. Moving into modeling, the training set for model development was comprised of a set of 4-, 4,4'-, and 5,5'-substituted-2,2'-bipyridines (5 and 9 training samples for modelling of the high-throughput and focused screening datasets, respectively). 6-, and 6,6'-substituted ligands were removed based on the results of threshold analysis (vide supra, Section 3.4.5.3).

3.4.5.5 Univariate Correlations and Models Using High-Throughput Experimental Results

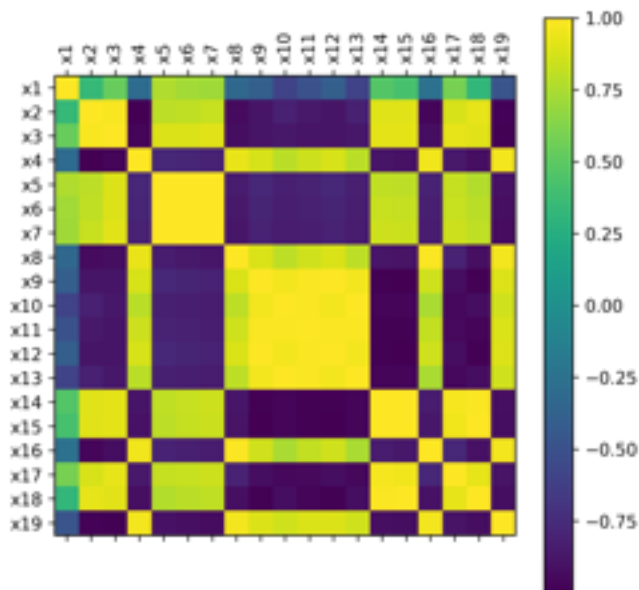
Figure 3.16 Univariate Correlations from High-Throughput Screening Results



We observed a variety of strong univariate correlations from this dataset; however, many of the descriptors that were examined were collinear (vide infra, Figure 3.17). As such, the top three univariate correlations are listed here.

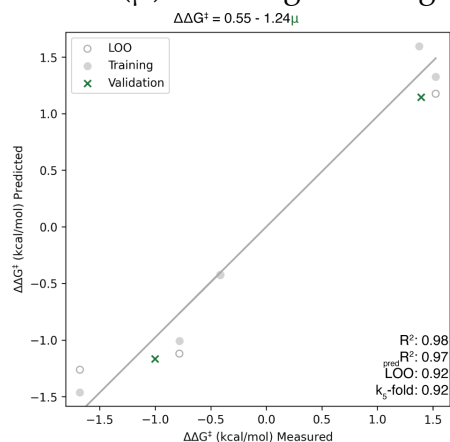
Figure 3.17 Collinearity Heatmap of All Univariate Correlations from High-Throughput Screening Results

x	Descriptor	R ²	p-value
1	E(HOMO)	0.78	3.46E-03
2	E(LUMO)	0.92	1.41E-04
3	μ	0.92	1.41E-04
4	ω	0.75	5.46E-03
5	E(d _{xz})	0.92	1.68E-04
6	E(d _{yz})	0.91	2.32E-04
7	E(d _{z2})	0.93	1.10E-04
8	NPA _{Br2}	0.74	5.91E-03
9	NPA _{N3}	0.74	5.82E-03
10	NPA _{N4}	0.82	1.99E-03
11	NPA _{avg(N3,N4)}	0.79	3.00E-03
12	NPA _{min(N3,N4)}	0.74	5.82E-03
13	NPA _{max(N3,N4)}	0.82	1.99E-03
14	NMR(δ_{iso}) _{N3}	0.8	2.66E-03
15	NMR(δ_{iso}) _{N4}	0.78	3.60E-03
16	NMR(δ_{iso}) _{Cipso}	0.7	9.67E-03
17	NMR(δ_{yy}) _{Br2}	0.85	1.12E-03
18	NMR(δ_{xx}) _{N3}	0.73	7.13E-03
19	NMR(δ_{xx}) _{Cipso}	0.89	4.13E-04



Provided in this table are all the univariate correlations from this dataset where $R^2 > 0.70$ and $p\text{-value} < 0.01$. In the collinearity heatmap, the diagonal represents a descriptor's collinearity with itself; off-diagonal correlations represent the collinearity of one parameter with another. We noted that these best univariate correlations demonstrated a high degree of collinearity (both proportionally and inversely collinear).

Models generated for this high-throughput screening dataset utilized a 0.3 equidistant split, where 70% of the input observations—that evenly span the output variable, $\Delta\Delta G^\ddagger$ —are assigned to the training set, whilst the remaining observations are assigned to the validation set. The algorithm used to select and partition observations into the training and validation sets is defined such that the highest and lowest values are partitioned into the training set rather than the validation set.

Figure 3.18 Best 1-Parameter Model (μ) from High-Throughput Screening Results

Our strongest model with this dataset was a 1-parameter model with μ (chemical potential), which is approximately the average of the HOMO and LUMO orbital energies.⁹⁴ This model was trained on commonly employed common 4,4'-disubstituted-2,2'-bipyridines. However, we were dissatisfied with the specificity it provided. We felt that designing a more tailored dataset would enable more insight into the catalytic system and lead to more effective predictions of reaction outcomes.

3.4.5.6 Univariate Correlations and Models Using the Focused Ligand Experimental Results

The training set consists of commonly employed common 4,4'-disubstituted-2,2'-bipyridines, and a suite of non-symmetric 4- and 4,4'-substituted-2,2'-bipyridines. When designing non-symmetric ligands, an effort was made to cover a range and combination of electron-donating and -withdrawing characteristics.

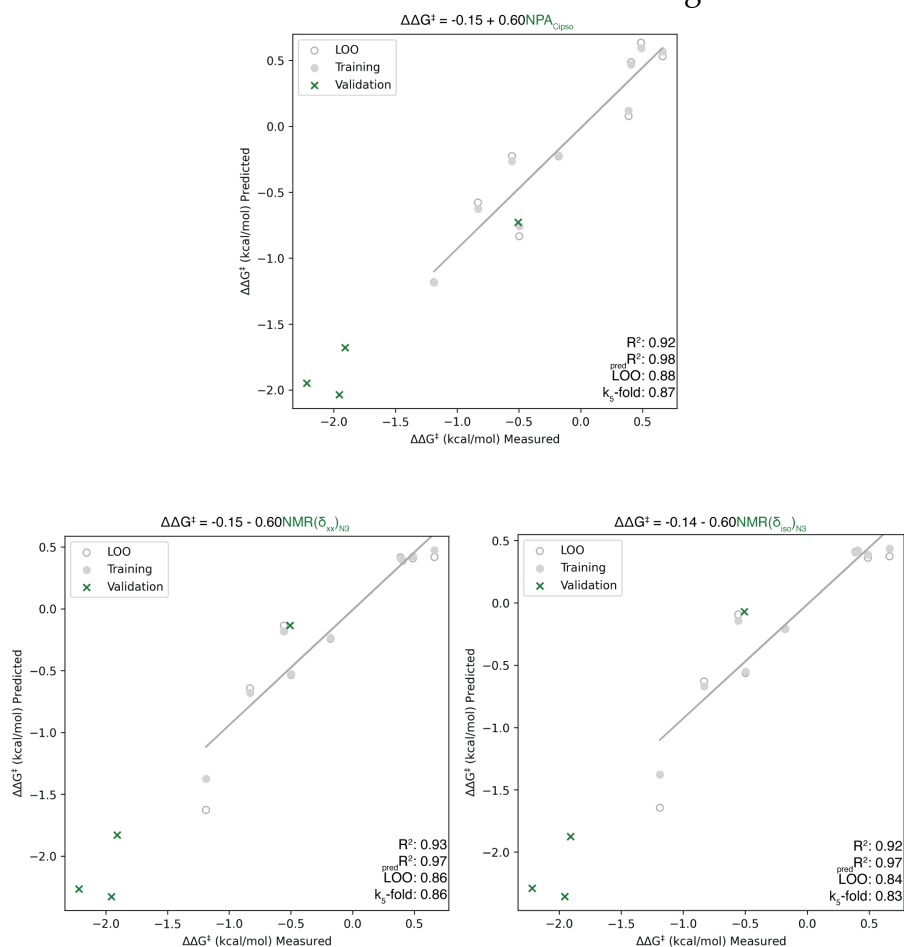
Figure 3.19 Univariate Correlations from Focused Screening Results^a

Descriptor	R ²	p-value
NMR(δ_{xx}) _{N3}	0.93	2.61E-05
NPA _{Cipso}	0.92	5.19E-05
NMR(δ_{iso}) _{N3}	0.91	5.43E-05
NPA _{N3}	0.88	1.96E-04
NMR(δ_{yy}) _{N3}	0.85	4.08E-04
NMR(δ_{zz}) _{Cipso}	0.81	9.65E-04
E(HOMO)	0.76	2.29E-03
NMR(δ_{xx}) _{Cipso}	0.76	2.25E-03
μ	0.75	2.70E-03
E(LUMO)	0.73	3.25E-03
E(d_{z2})	0.73	3.52E-03
NMR(δ_{iso}) _{Cipso}	0.73	3.44E-03
E(d_{yz})	0.72	3.82E-03
NMR(δ_{yy}) _{Cipso}	0.72	3.85E-03
E(LUMO) - E(HOMO)	0.71	4.43E-03
η	0.71	4.43E-03
E(d_{xz})	0.71	4.16E-03

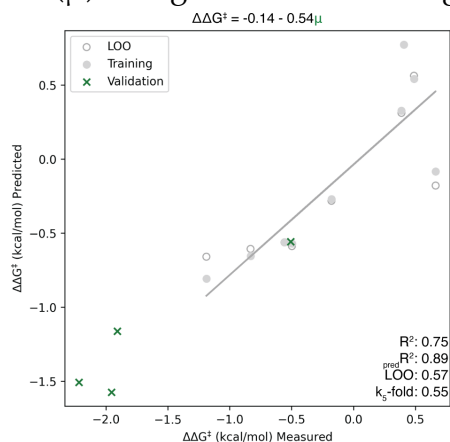
^aOnly descriptors from the square planar (.sqpl) computed dataset with univariate correlations where R² > 0.70 and p-value < 0.01 are listed here. Correlations with descriptors from the tetrahedral (.tet) dataset were not considered due to lack of catalytic relevance based on threshold analysis (vide supra, Section 3.4.5.3).

Univariate correlations, initial modelling efforts, and prediction of selectivities of the ligands in the validation set were performed prior to the synthesis and testing of ligands in the validation set. We chose to employ an external validation set consisting of three extrapolated points (**3.L3–3.L5**) and a single interpolated point (**3.L15**). Notably, we chose to employ 5,5'-dimethoxy-2,2'-bipyridine **3.L15** as the interpolation point due to large differences in the predicted selectivity using the strongest univariate correlations.

Figure 3.20 Best 1-Parameter Models from Focused Screening Results



We narrowed down our 1-parameter models with the focused screening experimental results to one each: with NPA_{Cipso} , the xx component of the anisotropic NMR shift of N3 ($NMR(\delta_{xx})_{N3}$), and the isotropic NMR shift of N3 ($NMR(\delta_{iso})_{N3}$). From these three models, we selected our best model from that which had the highest predicted R^2 ($_{pred}R^2$) and the lowest associated mean absolute error: MAE = 0.200 for the NPA_{Cipso} model, 0.219 for the $NMR(\delta_{xx})_{N3}$ model, and 0.237 for the $NMR(\delta_{iso})_{N3}$ model. Given that the training set did not include any 5,5'-disubstituted ligands, this finding also demonstrates transferability of this model to other substitution patterns present in the bpy class of ligands (exclusive of 6- or 6,6'-substitution).

Figure 3.21 1-Parameter Model (μ) Using Focused Screening Results

When we revisited the descriptor used to generate the best 1-parameter model for the high-throughput screening results (vide supra, Figure 3.18), we noticed that this descriptor failed to appropriately account for non-symmetric ligands. This supports our hypothesis that the collinearity of descriptors within the initial dataset was limiting specificity and translatability of the model.

Figure 3.22 Predicted Selectivity of In Silico Ligands Utilizing Optimal Model with $\text{NPA}_{\text{Cipso}}^{ab}$

Ligand	$\text{NPA}_{\text{Cipso}}$	Predicted $\Delta\Delta G^\ddagger$ (kcal/mol)
L24	-0.14914	0.27
L25	-0.14949	0.14
L26	-0.12209	10.53 ^a
L27	-0.11857	11.87 ^a
L28	-0.11859	11.86 ^a
L29	-0.13008	7.50 ^a
L30	-0.15232	-0.94
L31	-0.15321	-1.27
L32	-0.17014	-7.70 ^a
L33	-0.13452	5.82 ^a
L34	-0.15111	-0.48
L35	-0.15025	-0.15
L36	-0.15438	-1.72
L37	-0.14987	-0.01
L38	-0.15415	-1.63
L39	-0.15456	-1.79
L40	-0.15278	-1.11
L41	-0.15503	-1.96
L42	-0.15407	-1.60
L43	-0.15441	-1.73
L44	-0.15042	-0.21

^aThese ligands are 6- or 6,6'-(di)substituted. ^bPredictions are made via the equation for the univariate correlation with descriptor $\text{NPA}_{\text{Cipso}}$: $\Delta\Delta G^\ddagger = 56.85698 + 379.41561 \text{NPA}_{\text{Cipso}}$.

The predicted selectivity was acquired from the equation resulting from a linear regression of the focused ligand screen training set without normalization of the descriptor. It is evident that this model of selectivity does not appropriately handle sterically constrained ligands. As such, for predicting the selectivity of new ligands, we first recommend removal of 6- or 6,6'-(di)substituted ligands, then applying this model.

3.4.5.7 Alternative Models Using Free Ligand Parameters

The training set is the same as in Section 3.4.5.6. Note that the numbering of atoms is not consistent between the free ligands and the nickel complexes (vide supra, Figure 3.10). As such, relative values of parameters provide stronger correlations than absolute parameters based on atom number. For example, the maximum NPA charge (NPA_{max}) provides a stronger correlation than the NPA charge of a specific nitrogen donor (NPA_{N1}).

When comparing to models and correlations based on parameters sourced from nickel complexes, NPA_{\max} would be equivalent to NPA_{N3} due to the numbering scheme in the nickel complex.

Figure 3.23 Comparison of Univariate Correlations with Parameters from Unbound Ligand Descriptors

Descriptor	R ²	p-value
NPA_{\max}	0.91	5.05E-07
$NMR(\delta_{xx})_{N1}$	0.91	3.73E-07
$NMR(\delta_{iso})_{N1}$	0.90	6.42E-07
$NMR(\delta_{yy})_{N1}$	0.90	8.24E-07
NPA_{N1}	0.83	1.64E-05
NPA_{average}	0.79	4.44E-05
μ	0.72	2.37E-04
ω	0.70	3.62E-04

While reasonable, these correlations lose some nuance compared to the best models using parameters sourced from the nickel complex. In particular, the strongest model based on free ligands was unable to accurately predict the selectivity of the interpolated 5,5'-dimethoxy-2,2'-bipyridine (**3.L15**).

Chapter 4: Insight into the Relationship Between the Structure of Common L2 Dinitrogen Ligands and Selectivity in Cross-Electrophile Coupling

4.1 Introduction

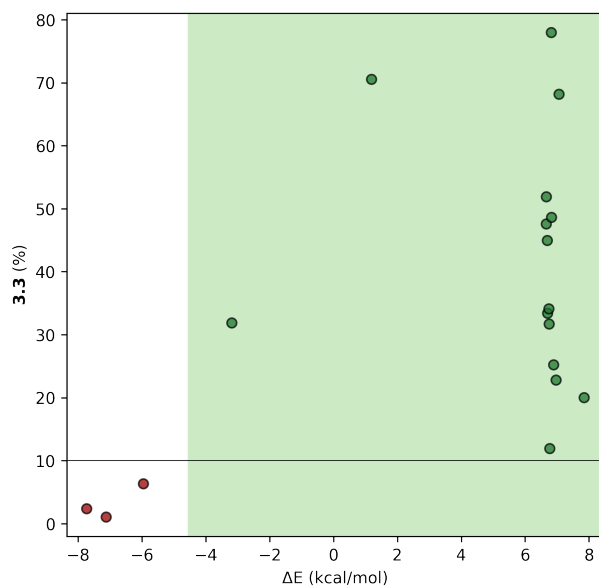
The successes described in Chapter 3 provide a roadmap for the development of models for selectivity provided by other common classes of L2 dinitrogen ligands. We evaluated the reactivity of common phen, PyCam, PyOx, BiOx, and BOX ligands utilizing the same model reaction (Scheme 3.2A) and high-throughput workflow employed for bpy ligands (*vide supra*, Section 3.4.3.1). The initial results provided by these studies provide a consistent picture of reactivity via class-specific correlations. While low dynamic ranges of data—both in computed descriptors and observed experimental outcomes—limit the full generation of strong statistical models of selectivity, certain trends remain consistent. The goal of this work was to generate a set of class-specific models to inform a more general picture of reactivity for these critical ligands. While direct extension of the trends observed does not necessarily translate between classes, this is to be expected. In related work by the Doyle group, strong inter-class correlations were observed within BiOx and BiIm ligands, but translation between classes led to less strong and informative results.³⁷ Rather, the correlation and subsequent principal component analyses helped distinguish between the more successful BiIm ligands and related BiOx ligands. We hypothesized that application of the same data science workflow that was successful for bpy ligands (Chapter 3) may help draw key distinctions between the remaining classes.

4.2 Results and Discussion

4.2.1 Phenanthroline (phen) Ligands

Due to similarities in structure and binding, phen ligands offer the simplest opportunity to translate the methods that were successful in bpys. Further, phen ligands are commonly used in a variety of base- and precious-metal catalysis. It is currently unclear what impact the extension of the π -system in the ligand backbone has on selectivity in XEC, and as such, we chose to begin our studies by treating phens as a separate class entirely.

Scheme 4.1 Threshold Analysis of phen Ligands Reveals a Reactivity Cliff for Steric Hindrance^a

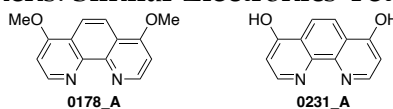


^aThreshold generated with $y_cut = 10$ and $class_weight = 'balanced'$. Decision threshold = -4.57, accuracy = 1.00, F1 score = 1.00, MCC = 1.00.

We began by utilizing binary classification of yields to categorize catalysts based on yield (Section 3.4.5.3). As in the related bpy system (Scheme 3.2A), we found a set of strong reactivity cliffs that suggest that sterically confined 2- and 2,9-(di)substituted phens promote a triplet, tetrahedral geometry in the (L)Ni^{II}(Ar)Br complex, and thus provide low selectivity (Scheme 4.1). An appropriate action moving forward would be to

remove sterically constrained ligands as we did in Chapter 3 or evaluate the use of computed metrics that take into account tetrahedral character (e.g., .boltz or .lowestgeom subsets of the computed library) when employing steric or electronic descriptors for classification. However, the success of classification utilizing the energy difference between the tetrahedral and square planar geometries makes the latter a less attractive option. Based on this result, we curated the training set to exclude ligands with substitution in the 2- and 9-positions. Utilizing the resulting dataset, we found no statistically sound correlations between computed features and experimental outcomes. There are two possible reasons for this lack of correlation: (1) we have not gathered the correct molecular descriptor(s) to describe the reactivity of phen ligands or (2) the experimental dataset either lacks sufficient dynamic range or is polluted with noise. We hypothesize that the latter effect (noise) is causing the lack of significant correlations based on the inclusion of both ligands with reactive functionalities and an over-representation of related phen derivatives.

Table 4.1 A Comparison of phens: Similar Electronics Yet Different Results



Ligand	3.3 (%)	$\Delta\Delta G^\ddagger$ (kcal/mol)	NPA_{N3}
0178_A	78	-1.20	-0.50920
0231_A	25	0.07	-0.50904

The correlations observed using this dataset are significantly weaker due to a number of confounding factors. First, reactive functionalities such as halides and alcohols are present on many of the ligands. For example, the most selective ligand **0178_A** and the equivalent 4,7-dihydroxy-1,10-phenanthroline **0231_A** provided significantly different yield and selectivity, despite possessing almost identical electronic characteristics (Table 4.2). Further, halogenated ligands provided a wide range of

observed yields that often did not follow the observed trends (Figure 4.2). Finally, the low dynamic range in electronic character of the tested ligands led to an overrepresentation of ligands in the center of the calculated parameter set. These ligands, mainly mono- and polymethylated phenanthrolines led to a cluster of datapoints that spread out the observed dataset and mitigated the impact of points near the top and bottom of selectivity, leading to overall worse trends.

Despite these shortcomings, qualitative analysis of the dataset suggests that similar trends are present compared to bpy ligands—more electron-rich ligands promote higher selectivity. For example, both the best evaluated bpy (**3.L2**) and phen (**0178_A**) ligands in the initial dataset incorporated electron-donating methoxy groups and yielded similar yields and selectivities (Table 4.2).

Table 4.2 General Electronic Trends Translate from bpy Ligands, but Reactive Functionalities Confound Analysis

Entry	Ligand	3.3 (%)	$\Delta\Delta G^\ddagger$ (kcal/mol)	$NPA_{C_{ipso}}$
1	3.L2	82	-1.68	-0.15298
2	0178_A	78	-1.20	-0.50920

To proceed with modelling of the reactivity of phen ligands, a more evenly dispersed, electronically diverse dataset is needed. We suggest that a specific training set be constructed to incorporate strongly and weakly donating ligands. Ligands with substitution in the 2- and 9- positions should be excluded based on the results of threshold analysis. Substitution on the 5- and 6- positions may be avoided, as modification of these positions is often synthetically difficult. Finally, the overrepresentation of common functionalities—mainly alkyl substituents—should be reduced. In order to more accurately evaluate the effects of substitution and electronic structure on the selectivity of phen ligands, a more even distribution of ligands bearing electron-donating and -withdrawing groups in the 3-, 4-, 7-, and 8- positions should be

employed. Surveys of such ligands have been performed in other catalytic systems and phen equivalents of the improved bipyridine suite—**3.L3**, **3.L4**, and **3.L5**—have been previously reported to provide improved performance over **0178_A**.^{99,100} We hypothesize that construction of such a dataset would enable the extension of the workflow that was successful in bpy ligands to phens.

4.2.2 Pyridyl Carboxamidine (PyCam) Ligands

PyCam ligands have been shown to provide improved selectivity and generality over related bipyridines or phenanthrolines. Despite these successes, the source of their improved selectivity is still unknown. We evaluated a series of PyCam and related ligands in the model reaction to identify trends in reactivity in the hope that distinguishing characteristics may arise that inform further structural and mechanistic hypotheses.

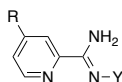
Table 4.3 Observed Univariate Correlations for PyCam Ligands

Descriptor Source	Descriptor	R ²	p-value
Square planar (.sqpl)	d _{x²-y²} energy	0.63	1.96E-03
Square planar (.sqpl)	NPA _{N3}	0.53	7.47E-03
Square planar (.sqpl)	NMR(δ_{xx}) _{N3}	0.55	5.81E-03
Tetrahedral (.tet)	NMR(δ_{xx}) _{N3}	0.73	4.18E-04
Weighted (.boltz)	NMR(δ_{xx}) _{N3}	0.55	5.80E-03

Unlike bpy and phen ligands, we did not perform threshold analysis on the PyCam dataset. None of the tested ligands performed below the threshold defined for the bpy and phen class ($y_{\text{cut}} = 10$, corresponding to 10 % yield and one turnover of cross-product). Thus, all members of the PyCam class would be classified as active. Further, we found that all of the tested PyCam ligands yielded square planar ground state geometries. We chose to search for correlations directly between the yield of the desired product rather than $\Delta\Delta G^\ddagger$, as the dynamic range was wider. We found only weak correlations (Table 4.3) between the computed descriptors and experimental outcomes.

These correlations suggest that as with the ligands described above, more electron-rich PyCam donors provide improved reaction outcomes. However, the dataset is more difficult to derive meaningful trends from, as all the tested PyCam ligands were selective for **3.3** over **3.4**. Even the electron-poor PyCam **0254_A** (32% yield, $\Delta\Delta G^\ddagger = -1.27$) provided significantly better results than the equivalent bpy (**3.L9**, 4% yield, $\Delta\Delta G^\ddagger = 1.39$). While beneficial from a catalytic standpoint, these results led to a distribution of yields and selectivity where a lack of differentiation of datapoints at the top of the dataset leads to low interpretability, and other off-cycle pathways may convolute the experimental dataset at high observed selectivity.

Table 4.4 *N*-cyanated PyCams Provide Lower Yield



Entry	R	3.3 (%)	$\Delta\Delta G^\ddagger$ (kcal/mol)	3.3 (%)	$\Delta\Delta G^\ddagger$ (kcal/mol)
		Y = H	Y = H	Y = CN	Y = CN
1	H	91	-2.18	74	-1.70
2	Et	84	-1.88	77	-2.01
3	<i>t</i> Bu	98	-2.73	83	-2.05
4	OMe	93	-2.19	68	-2.56

Despite these difficulties, several meaningful trends were observed. First, PyCam ligands based on heterocycles other than pyridine provided significantly reduced yield. For example, the lowest yielding PyCam derivatives, **0257_A** and **0260_A** are both based on diazines rather than pyridine. Additionally, in contrast to their successful application in other systems,^{17,84} we found that *N*-cyanated carboxamide derivatives provided lower yields of **3** than their non-cyanated analogues in all cases (Table 4.4). It is still unclear if this effect is due to modulation of the donation of the carboxamide subunit, or subtle withdrawing of electron-density from the pyridine.

These results provide initial insight into the role of electronic parameters on the selectivity provided by PyCam ligands. While the overall high yield of these ligands

limited interpretability, general observations suggest that ligands utilizing electron-poor diazine cores and all forms of carboxamidine *N*-functionalization lead to decreases in selectivity and yield. Future work should employ a wider range of *N*-functionalized catalyst—ideally each heteroarene unit should be represented by both an *N*-cyanated and non-cyanated entry—and a more challenging substrate pair in the model reaction. These combined modifications should enable more insight into the role of the carboxamidine subunit in promoting selectivity and provide a wider dynamic range of experimental results.

4.2.3 Pyridyl Oxazoline (PyOx) Ligands

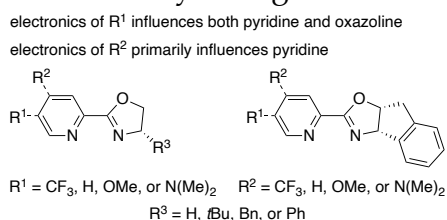
Table 4.5 Observed Univariate Correlations for PyOx Ligands

Descriptor Source	Descriptor	R ²	p-value
Square planar (.sqpl)	μ	0.87	6.87E-03
Weighted (.boltz)	μ	0.87	6.87E-03
Weighted (.boltz)	E(LUMO)	0.87	6.48E-03
Tetrahedral (.tet)	d _{xy} energy	0.92	2.48E-03

PyOx ligands are commonly used in palladium-catalyzed asymmetric heck reactions and offer a reliable introduction of chirality when utilized in nickel-catalyzed XEC reactions, enabling the translation of previously racemic functionalizations.^{101–103} While many studies focus mainly on enantioinduction when employing PyOx ligands, we sought to determine if our methods could accurately predict selectivity for off-cycle pathways. As such, we tested a small number of PyOx ligands with variations in steric and electronic structure in our model reactions. We chose to forego formal threshold analysis, as the steric environment about PyOx ligands are integral to their utility in asymmetric coupling. However, we did observe that the two ligands that promoted a ground state tetrahedral geometry—both QuinOx ligands—provided low yields of **3.3**. We searched for correlations utilizing yield in place of $\Delta\Delta G^\ddagger$, as the two are highly correlated. We found a strong univariate correlation between μ and the observed yield of

3.3 (Table 4.5). We hypothesized that distortion of the square planar geometry of ligands based on QuinOx may lead to a decrease in the robustness of the correlation. To test this, we also searched for a correlation between the observed yield and a weighted average of μ for the square planar and tetrahedral (L)Ni^{II}(Ar)Br complexes. However, we found no improvements. Despite this, the strength of the correlation between either μ parameter and the experimental outcome, in combination with the similarities in electronic structure between bpy and PyOx ligands,¹⁰⁴ suggest that significant improvements in the generality of PyOx ligands in XEC may be accomplished via the introduction of strong electron-donating groups in the 4- or 5-positions of the pyridine subunit. Moving forward, we suggest that a dataset containing more diverse electronic variations in the pyridine backbone be constructed in order to better determine the effects of electronic modulation of both the pyridine and oxazoline subunits (Scheme 4.2). Further, other notable oxazoline derivatives such as 8*H*-Indeno[1,2-*d*]oxazole, should be included. This ligand set could be benchmarked in the enantioselective cross-electrophile coupling of aryl halides with secondary alkyl electrophiles.

Scheme 4.2 Proposed Modifications of PyOx Ligands



4.2.4 Bioxazoline (BiOx) Ligands

Table 4.6 Observed Univariate Correlations for BiOx Ligands

Descriptor Source	Descriptor	R ²	p-value
Weighted (.boltz)	E(LUMO)	0.91	0.01
Weighted (.boltz)	μ	0.92	9.45E-03
Tetrahedral (.tet)	η	0.90	0.01
Square planar (.sqpl)	NMR(δ_{zz}) _{Br2}	0.91	0.01
Weighted (.boltz)	d _{xy} occupancy	0.93	8.53E-03

Bioxazoline (BiOx) ligands are commonly employed in asymmetric nickel catalysis.¹⁰⁵ In particular, these—and related BiIm—ligands have been utilized in the enantioselective arylation of epoxides and aziridines. However, the difficulty in functionalization of the oxazoline core limits the scope of electronic variation accessible using these ligands. As such, much of the electronic and steric modulation is due to the 4-substituent. We evaluated a small set of BiOx ligands in the model reaction. We found strong correlations between molecular orbital descriptors such as μ or η and the observed yield of **3.3** (Table 4.6). Additionally, strong correlations were found using more localized descriptors, such as the occupancy of the d_{xy} orbital of the nickel and an NMR tensor of the bromine.

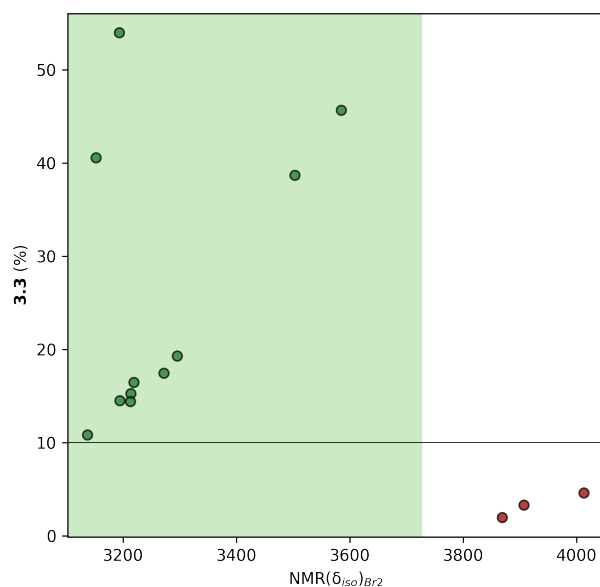
Despite the limited scope of the ligand set, the strength of the observed correlations indicates that the 4-substituents in BiOx ligands can have a large impact on activity and selectivity. Notably, the lack of any significant steric correlations (e.g. %V_{bur}) suggests that the critical effect of the 4-substituent is electronic in nature (although enantioselectivity is often governed by steric factors). Indeed, the least sterically confined BiOx ligand **0236_A** provided a relatively low yield of **3.3**. The highest yielding ligands bore a benzyl or phenyl substituent (**0239_A** and **0240_A**, respectively). Given the strong correlation with μ , we hypothesize that the addition of electron density to these rings may increase selectivity for **3.3** over **3.4**. Further investigations into the application of

these ligands in XEC should focus more closely on these benzyl and phenyl BiOx ligands, as they offer more facile modulation of the electronic character of the ligands. Additionally, introduction of related BiIm ligands to the test set may expand the pool of available ligands and expand the range of accessible electronic character.

4.2.5 Bisoxazoline (BOX) Ligands

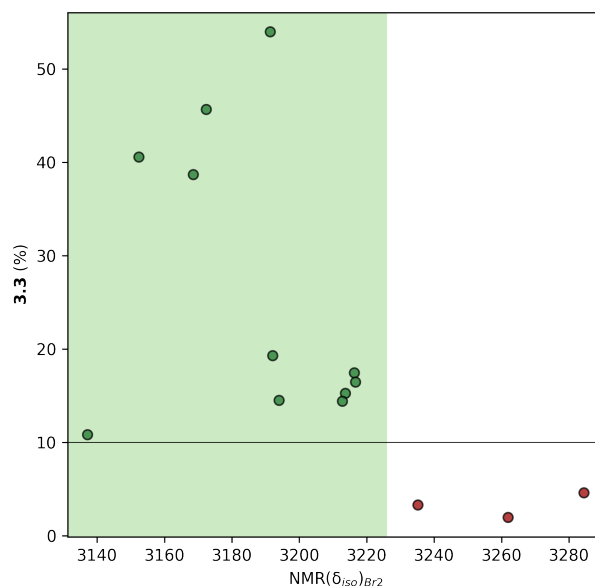
While common in a first-row transition metal catalyzed reactions, BOX ligands have seen limited application in XEC. The Reisman group has widely utilized IndaBox ligands in asymmetric XEC involving activated alkyl halides, but other applications of Box ligands for arylation of alkyl halides remains limited.¹⁰⁵ A general survey of BOX ligands to account for trends in selectivity may enable further development of asymmetric XEC. As such, we surveyed a range of BOX ligands in the model reaction to evaluate their selectivity for **3.3** over **3.4**.

Scheme 4.3 Threshold Analysis of BOX Ligands from the Weighted Average of Tetrahedral and Square Planar (.boltz) Parameter Sets^a



^aThreshold generated with $y_{cut} = 10$ and $class_weight = 'balanced'$. Decision threshold = 3726.90, accuracy = 1.00, F1 score = 1.00, MCC = 1.00.

Scheme 4.4 Threshold Analysis of BOX Ligands from the Square Planar (.sqpl) Parameter Set^a



^aThreshold generated with $y_cut = 10$ and $class_weight = 'balanced'$. Decision threshold = 3225.97, accuracy = 1.00, F1 score = 1.00, MCC = 1.00.

Given the ease of accessibility of a tetrahedral geometry for many (BOX)Ni^{II}(Ar)Br complexes, we performed a yield classification utilizing either a weighted average of parameters sourced from the square planar and tetrahedral complexes (.boltz, vide supra Section 3.4.5.2) or using the square planar parameter dataset (.sqpl). We found a strong reactivity cliff based on the NMR shift of the bromine atom, which accurately classified the least active and selective ligands (Scheme 4.3 for threshold generated from the weighted average parameters, for the threshold generated from the square planar parameters). These results suggest that utilizing weighted averages of parameters can provide insight into these catalyst systems that are more geometrically flexible.

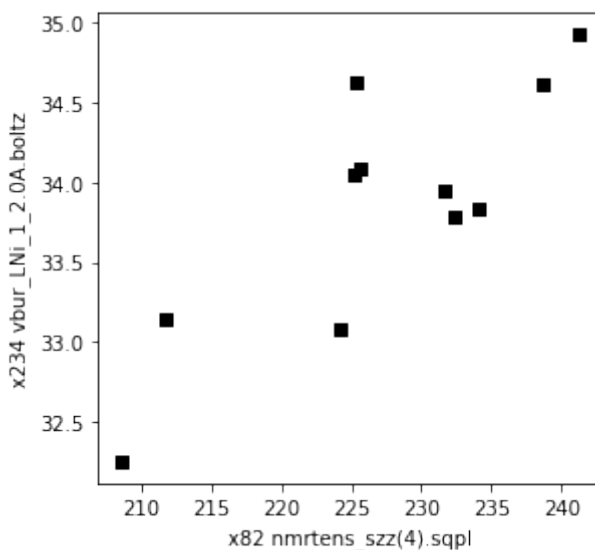
Table 4.7 Observed Univariate Correlations for BOX Ligands

Descriptor Source	Descriptor	R ²	p-value
Square planar (.sqpl)	NMR(δ_{zz}) _{N4}	0.55	8.97E-03
Weighted (.boltz)	%V _{bur} 2.0 Å	0.56	8.46E-03

Using a curated dataset of ligands that were classified as active, we found two weak correlations ($R^2 > 0.5$, $p\text{-value} < 0.01$; Table 4.7): (1) the weighted average of %

buried volume at 2.0 Å taken from the tetrahedral and square planar complexes, and (2) the zz -component of the anisotropic NMR tensor for N4, taken from the square planar complex. While neither of these correlations are sufficient to explain the selectivity promoted by BOX ligands, the observation that the two parameters are not highly colinear (Scheme 4.5) suggests that both steric and electronic factors may play a role determining selectivity. Given these results, we suggest that further work be performed utilizing a more diverse suite of BOX ligands. Given the robust reactivity cliff that we observed, virtual screening can be employed to avoid the inclusion of ligands that will be inactive, reducing the resources necessary to construct an additional experimental dataset. Given sufficient experimental results, we expect that a better understanding of BOX ligands in XEC may be achieved.

Scheme 4.5 Collinearity of $\text{NMR}(\delta_{zz})_{\text{N4}}$ with $\%V_{\text{bur}}, 2.0 \text{ \AA}^a$



$^aR^2 = 0.67$, $p\text{-value} = 0.002$.

4.3 Experimental

4.3.1 General Information, Procedure, and Computational Details

Please refer to the general information in Section 3.4.1, the general procedure in Section 3.4.3.1, and the computational details in Section 3.4.5. All procedures are as referenced unless otherwise specified.

4.3.2.1 Ligand Key and Results of Ligand Screens

Figure 4.1 phen Ligand Key

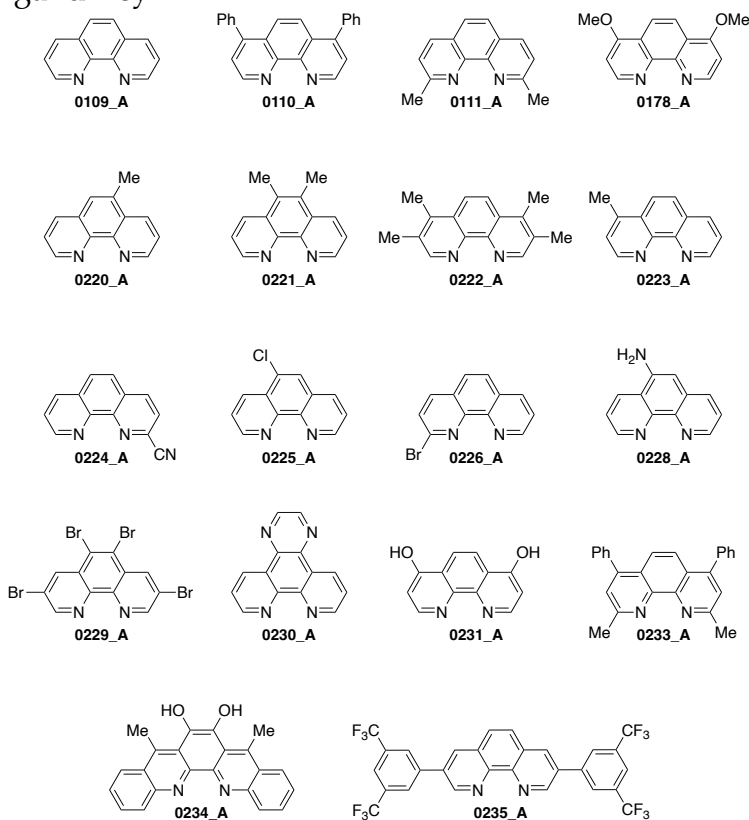
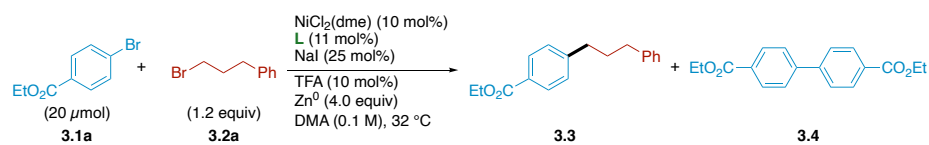


Figure 4.2 Results with phen Ligands^a

Ligand	3.3 (%)	3.4 (%)	$\Delta\Delta G^\ddagger$
0109_A	32	29	-0.06
0110_A	23	33	0.23
0111_A	2	22	1.32
0178_A	78	10	-1.20
0220_A	33	28	-0.11
0221_A	48	21	-0.48
0222_A	34	28	-0.12
0223_A	49	21	-0.49
0224_A	71	9	-1.21
0225_A	12	33	0.60
0226_A	32	25	-0.16
0228_A	52	20	-0.55
0229_A	68	2	-2.19
0230_A	45	23	-0.39
0231_A	25	28	0.07
0233_A	1	25	1.89
0234_A	6	19	0.64
0235_A	20	29	0.21

^aGeneral Procedure A was followed using ethyl 4-bromobenzoate and 1-bromo-3-phenylpropane.

Figure 4.3 PyCam Ligand Key

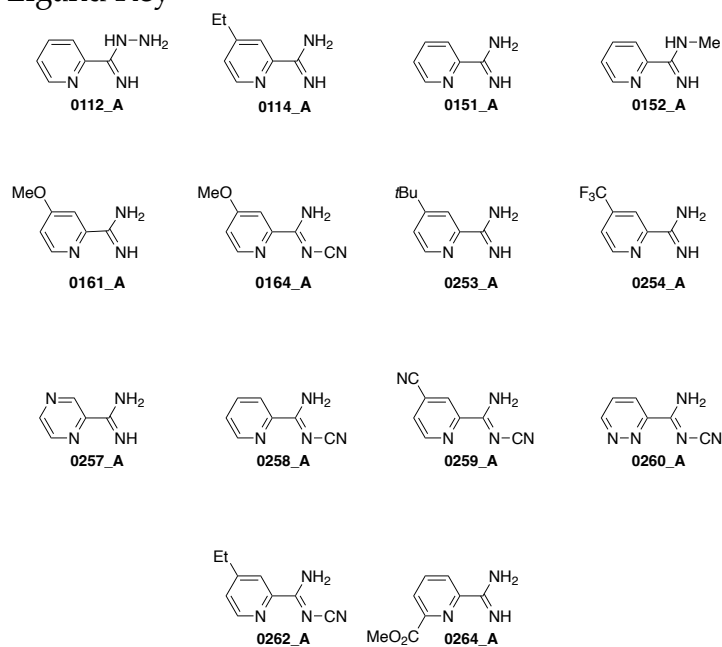


Figure 4.4 Results with PyCam Ligands^a

Ligand	3.3 (%)	3.4 (%)	$\Delta\Delta G^\ddagger$
0112_A	63	1	-2.58
0114_A	84	4	-1.88
0151_A	91	2	-2.18
0152_A	74	8	-1.33
0161_A	93	2	-2.19
0164_A	68	1	-2.56
0253_A	98	1	-2.73
0254_A	45	21	-0.46
0257_A	31	4	-1.27
0258_A	74	4	-1.70
0259_A	83	3	-2.05
0260_A	19	0	-2.67
0262_A	77	3	-2.01
0264_A	40	17	-0.52

^aGeneral Procedure A was followed using ethyl 4-bromobenzoate and 1-bromo-3-phenylpropane.

Figure 4.5 PyOx Ligand Key

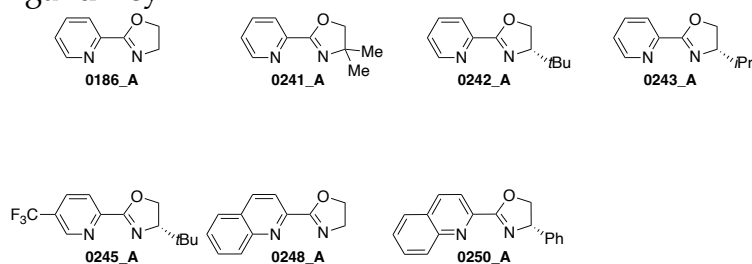
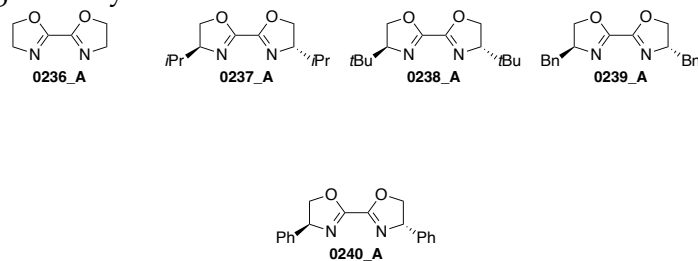


Figure 4.6 Results with PyOx Ligands^a

Ligand	3.3 (%)	3.4 (%)	$\Delta\Delta G^\ddagger$
0186_A	45	23	-0.40
0241_A	48	15	-0.70
0242_A	34	20	-0.32
0243_A	43	19	-0.49
0245_A	5	38	1.21
0248_A	23	21	-0.06
0250_A	5	35	1.16

^aGeneral Procedure A was followed using ethyl 4-bromobenzoate and 1-bromo-3-phenylpropane.

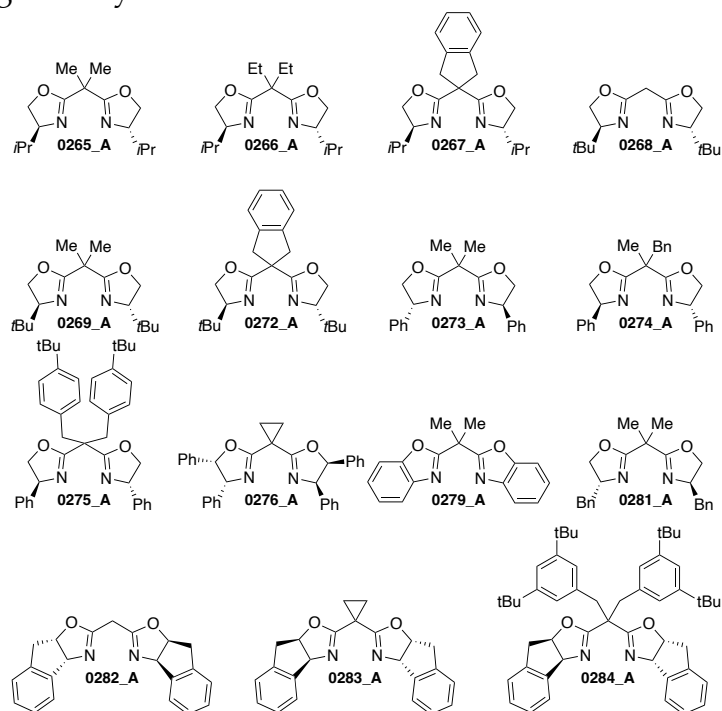
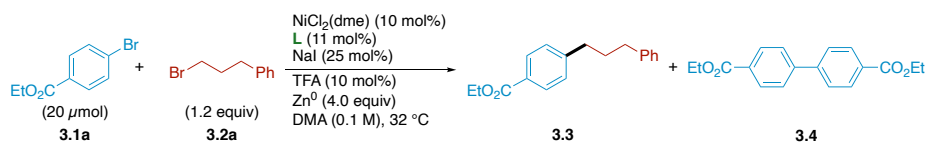
Figure 4.7 BiOx Ligand Key

Figure 4.8 Results with BiOx Ligands^a

Ligand	3.3 (%)	3.4 (%)	$\Delta\Delta G^\ddagger$
0236_A	24	32	0.17
0237_A	30	10	-0.65
0238_A	17	10	-0.31
0239_A	44	20	-0.46
0240_A	41	17	-0.51

^aGeneral Procedure A was followed using ethyl 4-bromobenzoate and 1-bromo-3-phenylpropane.

Figure 4.9 BOX Ligand Key

Figure 4.10 Results with BOX Ligands^a

Ligand	3.3 (%)	3.4 (%)	$\Delta\Delta G^\ddagger$
0265_A	17	20	0.08
0266_A	16	11	-0.26
0267_A	19	18	-0.04
0268_A	3	6	0.33
0269_A	5	19	0.83
0272_A	2	2	0.04
0273_A	54	8	-1.11
0274_A	46	8	-1.02
0275_A	39	3	-1.58
0276_A	33	3	-1.45
0279_A	15	9	-0.34
0281_A	41	9	-0.87
0282_A	14	3	-0.85
0283_A	14	17	0.11
0284_A	11	14	0.17

^aGeneral Procedure A was followed using ethyl 4-bromobenzoate and 1-bromo-3-phenylpropane.

4.3.3 Results of Statistical Analysis

Figure 4.11 Threshold Analysis of phen Ligands^a

Parameter	Decision Threshold	Accuracy	F1	MCC
d _{xz} Occupancy	1.94	0.78	0.85	0.56
NMR(δ_{zz}) _{Br2}	4193.54	0.94	0.97	0.79
NMR(δ_{iso}) _{Cipso}	-17.64	0.89	0.93	0.72
NMR(δ_{iso}) _{Br2}	3255.33	0.94	0.97	0.79
Δ in \angle N3–Ni–N4 and \angle Br2–Ni–C _{ipso}	11.65	0.94	0.97	0.84
NMR(δ_{zz}) _{Cipso}	188.44	0.94	0.97	0.84
NMR(δ_{zz}) _{N3}	269.21	0.94	0.97	0.84
NPA _{Cipso}	-0.14	0.94	0.97	0.84
NPA _{Ni}	0.68	0.94	0.97	0.84
E(HOMO)	-0.22	0.94	0.97	0.84
d _{z2} Occupancy	1.95	0.94	0.97	0.84
d _{yz} Occupancy	1.92	0.94	0.97	0.84
Ni–N4 Distance	1.96	0.94	0.97	0.84
Ni–N3 Distance	2.04	0.94	0.97	0.84
\angle N3–Ni–N4	81.92	0.94	0.97	0.84
ΔE (Tetrahedral – Square Planar)	-4.57	1.00	1.00	1.00
NMR(δ_{zz}) _{N4}	269.32	1.00	1.00	1.00
NMR(δ_{yy}) _{Cipso}	-93.12	1.00	1.00	1.00
Ni–Br2 Distance	2.29	1.00	1.00	1.00
\angle Br2–Ni–C _{ipso}	86.35	1.00	1.00	1.00

^aThreshold analysis performed with y_cut = 10 (corresponding to a % yield cutoff of 10%, or one turnover), 'balanced' class weight, and square planar subset of descriptor library.

Chapter 5: Miscellaneous Computational Efforts

5.1 Identification of 2,2'-Bipyridine-6-Carbonitrile and Initial Efforts to Rationalize Their Experimental Outcomes

5.1.1 Introduction

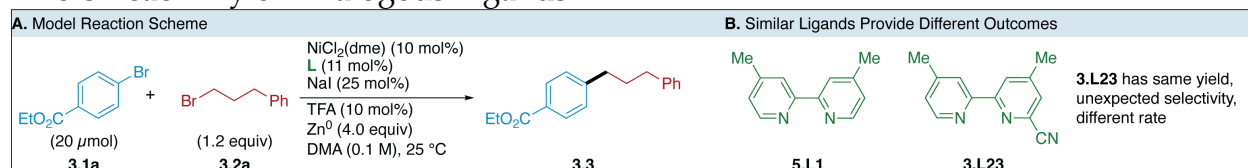
In depth understanding of ligand reactivity and geometry offers distinct benefits in the prediction and design of new ligands that improve reaction outcomes. A less obvious benefit is the ability to rapidly identify experimental observations that contrast with the current model of selectivity and reactivity. When faced with these outliers, chemists must either reevaluate their logic and models or establish the molecular feature that differentiates the observed outlier. These discoveries, while serendipitous in their origin can yield new understandings of reactivity given careful investigation. Herein, we describe the identification of 2,2'-bipyridine-6-carbonitrile ligands, which display reactivity distinct from their parent bipyridines and provide a new point of modulation of reactivity in bipyridine-nickel catalyzed cross electrophile coupling.^{92,106}

5.1.2 Results and Discussion

While classifying bpy ligands based on yield, we identified a single entry that displayed reactivity distinct from other entries. This ligand, **3.L23**, was calculated to have an accessible tetrahedral state, which should promote low selectivity for the cross-product. Additionally, the introduction of an electron-withdrawing nitrile group is predicted to reduce the NPA charge on C_{ipso}, also decreasing selectivity. As such, **3.L23** displays reactivity in contrast with both nodes of the decision tree described in Chapter 3. Notably, the nitrile group had no effect on the yield compared to the equivalent

bipyridine **5.L1**. This observation led us to reevaluate the reactivity of these ligands and investigate the effects of cyanation of common bipyridines.

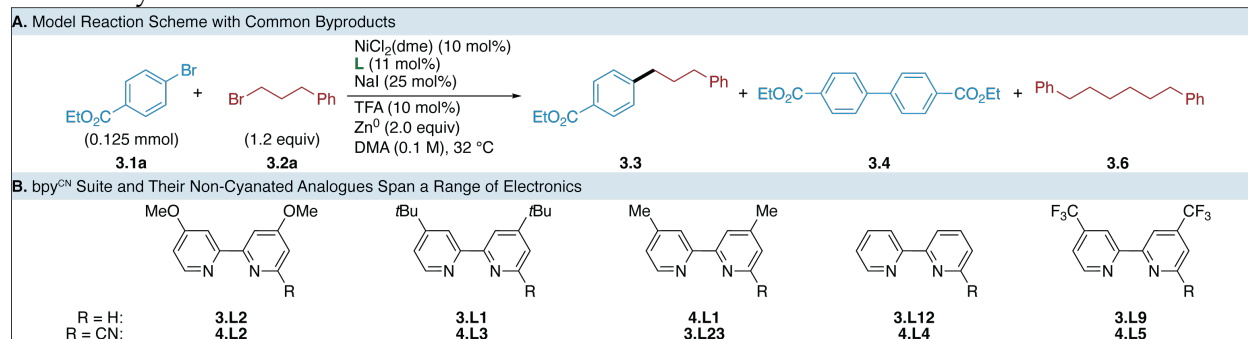
Table 5.1 Initial Observations from High-Throughput Screening Dataset: 6-Cyanation Alters Reactivity of Analogous Ligands^a



Entry	L	3.3 (%)	Selectivity (3.3 : 3.4)	Rate (M/min) ^b
1	5.L1	70	5.8:1	1.1E-04
2	3.L23	70	6.7:1	3.4E-04

^aReactions were set up following General Procedure A outlined in Section 3.4.3.1, with data for **3.L23** taken from Figure 3.2. Yields and selectivity were determined by UPLC-MS. ^bRate was determined from 15–75 min to account for any induction period.

We synthesized a suite of 2,2'-bipyridine-6-carbonitrile ligands with a variety of electron-donating and -withdrawing groups in the 4,4'-positions. When we evaluated these ligands in a modified version of the model reaction to determine if the conserved reactivity between **5.L1** and **3.L23** was general (Table 5.2). We observed that the identical yield of these two ligands was serendipitous, as there was a significant shift in the yield of **3.3** for electron-rich and -poor bpy and bpy^{CN} ligands. Interestingly, we saw an inversion of the electronic trends described previously in Chapter 3. While electron-rich bpy ligands yield the highest selectivity, electron-poor bpy^{CN} ligands provide the highest yield of **3.3**. Along with this shift in electronic trends, we observed a shift in the side product distribution. All bpy^{CN} ligands yielded low amounts of **3.4** and instead yielded the alkyl homodimer **3.6** as the major side product. While we had previously observed this side product in other couplings, it only formed after the complete consumption of **3.1a**.

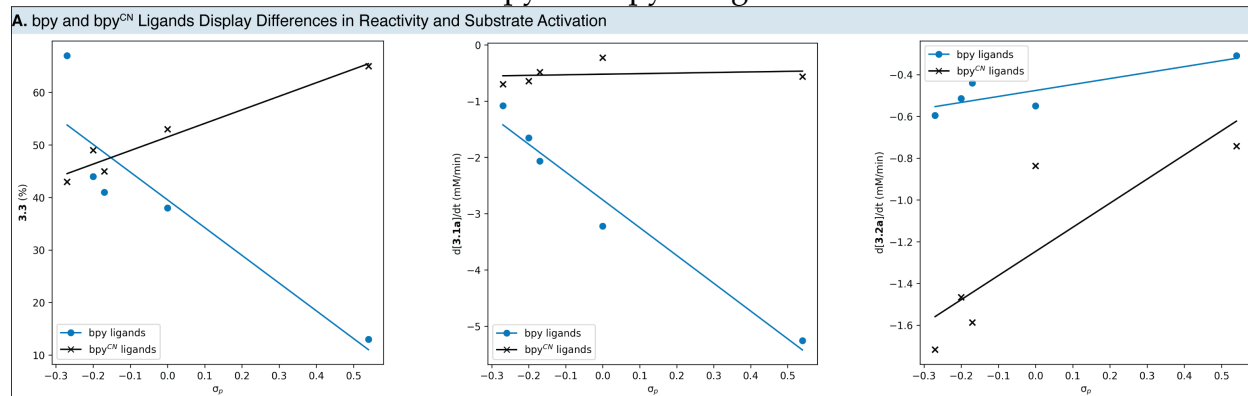
Table 5.2 A Evaluation of bpy^{CN} Ligands Reveals a Reversed Trend for Selectivity and Reactivity^a

Entry	Ligand Number	R	Y	3.3 (%)	3.4 (%)	3.6 (%)	Selectivity (3.3:3.4)	Selectivity (3.3:3.6)
1	3.L2	OMe	H	67	6	20 ^b	11:1	3.4:1
2	4.L2	OMe	CN	43	5	35	8.6:1	1.2:1
3	3.L1	<i>t</i> -Bu	H	44	21	26 ^b	2.1:1	1.7:1
4	4.L3	<i>t</i> -Bu	CN	49	6	30	8.2:1	1.6:1
5	4.L1	Me	H	41	22	26 ^b	1.9:1	1.6:1
6	3.L23	Me	CN	45	5	32	9.0:1	1.4:1
7	3.L12	H	H	38	25	16 ^b	1.5:1	2.4:1
8	4.L4	H	CN	53	3	26	18:1	2.0:1
9	3.L9	CF ₃	H	13	31	6 ^b	0.42:1	2.2:1
10	4.L5	CF ₃	CN	65	4	12	16:1	5.4:1

^aReactions were set up following General Procedure C outlined in Section 5.1.3.1.3. Yields and selectivity were determined by GC-FID. ^b3.6 was not observed until 3.1a was completely consumed.

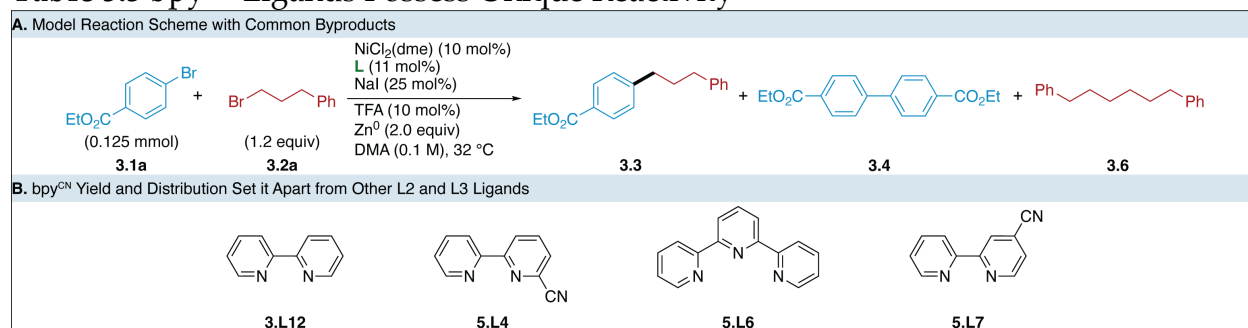
Additional analysis of reaction outcomes and rates confirmed the shift in the correlation of the reaction yield and electron-density of the bipyridine ligands. Further analysis of the rate of consumption of 3.1a showed that there was no electronic trend— $\rho = -0.075$ —observed for bpy^{CN} ligands.¹⁰⁷ This contrasts strongly with bpy ligands, where the same trend is observed as in Chapter 3, electron-poor bpy ligands rapidly dimerize 3.1a, leading to catalyst turnover and subsequently higher rates of consumption. A contrasting trend is observed in the rate of consumption of 3.2a, where more electron-rich ligands consistently consume the bromoalkene more rapidly. This effect is stronger for bpy^{CN} ligands, where electron-rich entries rapidly form the alkyl homodimer. This trend informs the observed yields for bpy^{CN} ligands—electron-poor examples provide higher selectivity for 3.3 over 3.6, leading to higher yields.

Scheme 5.1 Electronic Trends for bpy and bpy^{CN} Ligands^a



^aReactions were set up following General Procedure C outlined in Section 5.1.3.1.3.. Concentrations of all reagents were determined by GC-FID. Rates were determined from 0–30 min when the reaction rate was linear. For reactions that were complete in under 30 min, the rate was estimated from 0–15 min.

Selectivity for **3.6** over **3.4** as the major byproduct of the model system is unusual for bpy ligands. However, the rapid activation of alkyl electrophiles is commonly observed for L3 ligands such as tpy or bpp derivatives.⁴⁸ As such, we hypothesized that the pendent nitrile group in bpy^{CN} ligands may act as an additional, weak donor, changing the denticity of these ligands. Indeed, when compared to canonical L2 and L3 ligands, bpy^{CN} **5.L4** provides side product distributions and rates of formation more similar to tpy **5.L6** rather than bpy **3.L12**. This result suggested that bpy^{CN} is in fact tridentate. However, when we evaluated 2,2'-bipyrdine-4-carbonitrile **5.L7**, we found little change in yield or selectivity compared to the 6-carbonitrile analogue. This result suggests that bpy^{CN} ligands provide reactivity distinct from similar pyridine-based L2 and L3 ligands.

Table 5.3 bpy^{CN} Ligands Possess Unique Reactivity^a

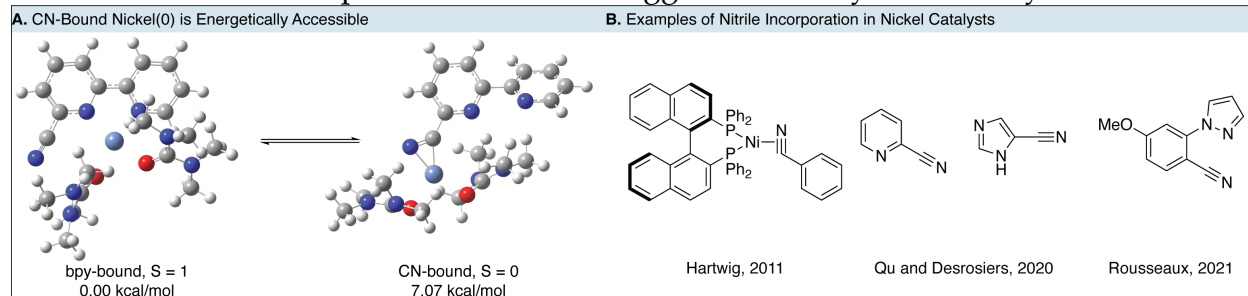
Entry	Ligand	3.3 (%)	3.4 (%)	3.6 (%)
1	3.L12	38	25	16 ^b
2	5.L4	55	3	26
3	5.L6	32	5	23
4	5.L7	55	12	20

^aReactions were set up following General Procedure C outlined in Section 5.1.3.1.3. Yields and selectivity were determined by GC-FID. ^b3.6 was not observed until 3.1a was completely consumed.

Our current hypothesis is that dynamic interchange of the binding mode of bpy^{CN} ligands enables a shift in the operative mechanism in the model XEC reaction. Given the results in Table 5.2 and Table 5.3, it is evident that the position of the nitrile functionality plays little role in the selectivity of reactions. This can indicate either rapid, dynamic interchange in binding modes, or that the ligand exclusively binds to the nitrile. Binding of aryl nitrile ligands to nickel is common in a number of fields. Hartwig and coworkers have shown that use of a benzonitrile supporting ligand can stabilize low-valent nickel compounds, enabling improved reaction outcomes.^{108,109} More recently, researchers at Boehringer Ingelheim published the use of pyridine-2-carbonitrile or 1-*H*-imidazole-5-carbonitrile as ligands in the XEC of aryl halides with alkyl bromides.⁴⁹ While they did not pursue further studies into the binding or reactivity of these ligands, these results suggest that these ligands may be more broadly applicable in XEC. Finally, Rousseaux and co-workers designed ligands with pendant benzonitrile functionalities that promote reductive elimination of sterically crowded C–C bonds in the Kumada cross-coupling of tertiary nucleophiles.¹¹⁰ These reports suggest that the benefits of bpy^{CN} ligands may be

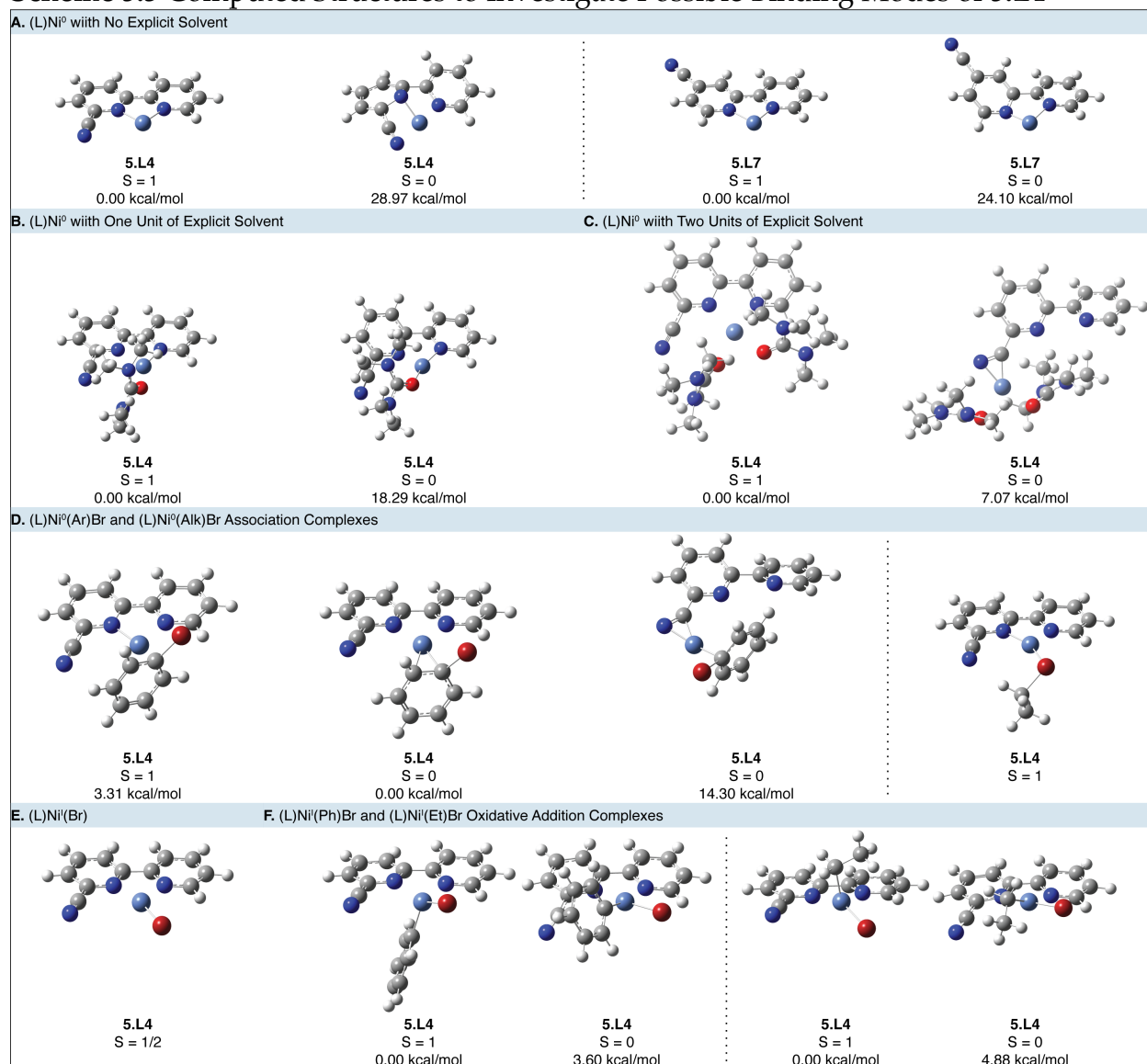
broad, but do not provide a path to rationalize full exchange of binding modes between a bifunctional molecule.

Scheme 5.2 Initial Computational Studies Suggest Flexibility in Denticity



We are currently utilizing DFT to investigate the thermodynamics of different binding modes of bpy^{CN} **5.L4** to nickel in a variety of oxidation states. While still incomplete, these studies suggest that both bpy-bound and CN-bound modes are accessible. We began by investigating the binding of both **5.L4** and **5.L7** to nickel(0) in the absence of additional supporting ligands. In accordance with previous finding, the singlet nickel(0) displayed significant distortion and was much higher in energy than the triplet geometry. We were unable to find a low energy, CN-bond isomer of either of these complexes. We hypothesized that the additional stability afforded by the bidentate bpy-bound isomer prevented the formation of a 12-electron complex. To further match experimental conditions, which include a Lewis basic DMA solvent, we added two equivalents of *N,N,N',N'*-tetramethylurea (TMU) as a symmetric, less conformationally labile solvent equivalent. Upon addition of two explicit solvent ligands to our calculations, we were able to identify a minimum in which the bpy ligand completely deligated, and the nickel(0) center—supported by the donation of the lone pairs of the two oxygens on the solvent ligands—bound exclusively to the nitrile group. While higher in energy than the equivalent bpy-bound triplet geometry, the low calculated relative energy (7.07 kcal/mol) suggests that this geometry catalytically accessible.

Scheme 5.3 Computed Structures to Investigate Possible Binding Modes of 5.L4



Notably, the energy gap between triplet bpy-bound, and singlet CN-bound geometries expanded when the two solvent ligands were exchanged for π -bound bromobenzene. In fact, the singlet, bpy-bound geometry was found to be the lowest energy isomer. Additional optimized geometries and energies—relative only to the other geometries and multiplicities of complexes containing the same molecules—are presented in Scheme 5.3. Some notable structures and multiplicities, such as CN-bound, $\text{bpy}^{\text{CN}}\text{Ni}^0(\text{BrEt})$ have not yet been found. While this may be due to a shallow energy well,

further work may help inform a revised mechanistic picture for XEC catalyzed by these new ligands. Our computational work is ongoing and will continue to center around the thermodynamics of ligand binding modes. We expect that these studies, supplemented by spectroscopic analysis of discrete complexes, stoichiometric reactions to evaluate catalyst selectivity, and nitrogen knockout experiments will better establish the binding and reactivity of these ligands and enable the further development of alkyl-first XEC.

5.1.3 Experimental

5.1.3.1 General Information

5.1.3.1.1 Reagents

Metals and Catalysts

Nickel(II) chloride dimethoxyethane, NiCl₂(dme), was purchased from Sigma-Aldrich. Zinc flake (-325 mesh) was purchased from Alfa Aesar. Tetrakis(triphenylphosphine)palladium(0) was purchased from Oakwood Products. All metals and catalysts were stored in a nitrogen-filled glovebox and used without additional purification.

Ligands

2,2'-Bipyridine was purchased from Sigma-Aldrich. 4,4'-dimethoxy-2,2'-bipyridine was purchased from Ambeed or Sigma-Aldrich. 4,4'-Bis(trifluoromethyl)-2,2'-bipyridine was purchased from Ambeed. 4,4'-Di-*tert*-butyl-2,2'-bipyridine was purchased from TCI.^H

^H These experiments were performed prior to the observation that **3.L1** purchased from different suppliers yielded different selectivity. It is unclear if the impurity was carried through the generation of **4.L3**.

2,2':6',2''-Terpyridine was purchased from Strem. Ligands were stored and handled in a nitrogen-filled glovebox and used without further purification.

Substrates

Ethyl 4-bromobenzoate was purchased from Oakwood. 1-Bromo-3-phenylpropane was purchased from TCI America. Unless otherwise specified, all substrates were purchased from commercial sources, stored on the benchtop, and used without further purification.

Solvents

Anhydrous *N,N*-Dimethylacetamide (DMA) was purchased from Sigma-Aldrich and stored in a nitrogen-filled glovebox.

Other Reagents

Sodium iodide and trifluoroacetic acid (TFA) were purchased from Sigma-Aldrich. 4,4''-Dimethyl-1,1'-biphenyl was purchased from Thermo Fisher Scientific. Other reagents, substrates, and solvents were purchased from commercial sources, stored on the benchtop, and used without further purification unless otherwise specified.

5.1.3.1.2 Methods

NMR Spectroscopy

^1H , ^{13}C , and ^{19}F NMR spectra were acquired on 400 and 500 MHz Bruker Avance III NMR instruments. NMR chemical shifts are reported in ppm. ^1H chemical shifts are referenced to tetramethylsilane (TMS) in CDCl_3 ($\delta = 0.00$ ppm). ^{13}C and ^{19}F chemical shifts were absolute referenced to the accompanying ^1H spectrum. Coupling constants (J) are reported in Hertz.

High Resolution Mass Spectrometry

Mass spectrometry data was collected on a Thermo Scientific Q Exactive Plus Hybrid Quadrupole-Orbitrap via flow injection with electrospray ionization by the Paul Bender Chemical Instrumentation Center facility at the University of Wisconsin-Madison.

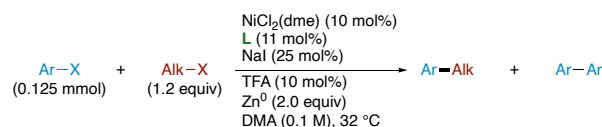
Gas Chromatography

GC analyses were performed on an Agilent 7890A GC equipped with dual DB-5 columns (20 m × 180 μm × 0.18 μm), dual FID detectors, and H₂ as the carrier gas. A sample volume of 1 μL was injected at a temperature of 300 °C and a 100:1 split ratio. The initial inlet pressure was 20.3 psi but varied as the column flow was held constant at 1.8 mL/min for the duration of the run. The initial oven temperature of 50 °C was held for 0.46 min followed by a temperature ramp of 65 °C/min up to 300 °C. The total run time was 5.0 min and the FID temperature was 325 °C.

Flash Chromatography

Flash chromatography was performed on a Teledyne ISCO Rf-200 (detection at 254 and 280 nm) equipped with an 80 g Teledyne ISCO Redisep Rf Gold silica gel column (20–40 μm particle size) or on a Biotage Isolera One (detection at 210 nm and 400 nm) equipped with a 25 g KPsil column (40–63 μm particle size). Products were visualized by UV.

5.1.3.1.3 General Procedure C: Evaluation of Ligands in 1-Dram Vials



Stock solutions were prepared in a nitrogen-filled glovebox. A stock solution of nickel(II) chloride dimethoxyethane (274.6 mg, 1.250 mmol) in DMA was prepared in an oven-

dried 25 mL volumetric flask. This solution was stored in a sealed 20 mL vial in the glovebox and stirred immediately prior to use. A stock solution of 4,4'-dimethylbiphenyl (1500.0 mg, 8.2300 mmol), aryl halide (12.500 mmol), and alkyl halide (15.000 mmol) in DMA was prepared in an oven-dried 25 mL volumetric flask. This solution was stored in a sealed 20 mL vial in the glovebox and stirred immediately prior to use. Additionally, separate stock solutions of sodium iodide (183.6 mg, 1.225 mmol) and TFA (57.0 mg, 0.500 mmol) in DMA were prepared in oven-dried 5 mL volumetric flasks. These solutions were prepared fresh each time reactions were performed.

In a nitrogen-filled glovebox, an oven-dried 1 dram vial equipped with a PTFE-coated stir bar was charged with the ligand (0.014 mmol, 0.11 equiv), nickel(II) chloride dimethoxyethane (2.70 mg, 0.0125 mmol, 0.100 equiv, in 250 μ L DMA), and DMA (500 μ L). The vial was then sealed with a phenolic screw cap bearing a PTFE-backed silicone septum and placed on a stir plate, where it was stirred (1000 rpm) at 30 °C for 30 min. After this time, the cap was removed and sodium iodide (4.70 mg, 0.0313 mmol, 0.250 equiv, in 125 μ L of DMA) was added, followed by a mixture of: aryl halide (0.125 mmol, 1.00 equiv); alkyl halide (0.150 mmol, 1.20 equiv); and 4,4'-dimethylbiphenyl (as an internal standard; 15.0 mg, 0.0823 mmol, 0.658 equiv, in 250 μ L of DMA). Zinc flake (16.4 mg, 0.250 mmol, 2.00 equiv) was added to the vial. The contents of the vial were briefly swirled to incorporate the zinc and TFA (1.40 mg, 0.0125 mmol, 0.100 equiv, in 125 μ L of DMA) was added. The vial was resealed with the screw cap and placed on a pre-heated stir plate, where it was stirred (1000 rpm) at 32 °C.

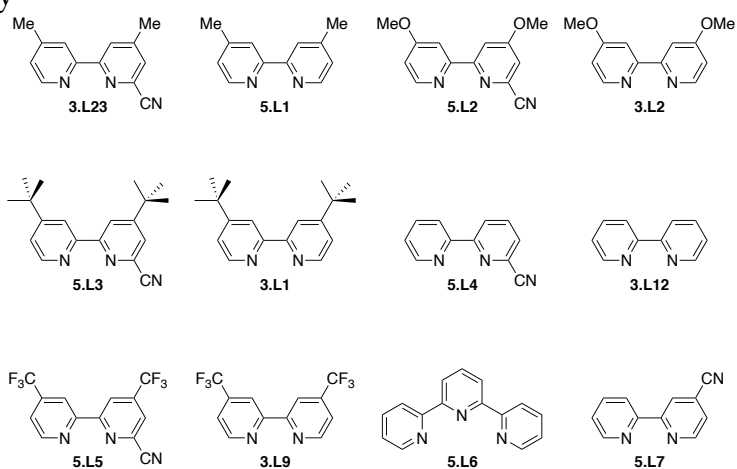
Aliquots were taken at 0, 15, 30, 45, 60, 75, 90, 120, and 180 min to determine the concentrations of the product and side products, and at 24 h to establish the final yield. The aliquot (20 μ L) was obtained by removing the screw cap and sampling the stirring

reaction with an autopipette. The aliquot was diluted into 1000 μL of ethyl acetate, removed from the glovebox, and quenched with 1 mL of deionized water. The organic layer was then passed through a short (1.5 cm in a pipette) silica plug and analyzed by GC-FID. Concentrations of the reactants, desired product, and side products were determined as calibrated ratios of the area of the analyte peak compared to the area of the internal standard peak.

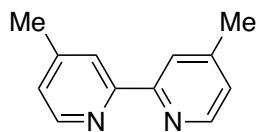
5.1.3.2 Ligand Key and Preparation

5.1.3.2.1 Ligand Key

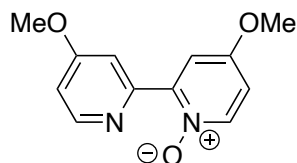
Figure 5.1 Ligand Key



5.1.3.2.2 Preparation of Ligands

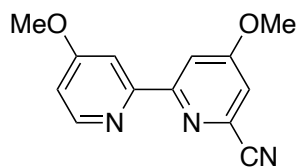


4,4'-dimethyl-2,2'-bipyridine (5.L1) was obtained as a byproduct of the oxidative coupling of 4-methylpyridine to form 4,4',4''-trimethyl-2,2':6',2''-terpyridine. For an analogous procedure, see the preparation of **3.L14**. Characterization data match those of commercial samples.



4,4'-dimethoxy-[2,2'-bipyridine] 1-oxide (5.L2a) was prepared by modification of the literature procedure.¹⁷

A 100 mL round-bottom flask equipped with a PTFE-coated stir bar was charged with 4,4'-dimethoxy-2,2'-bipyridine (2162.4 mg, 10.000 mmol, 1.0000 equiv). The flask was placed in a water bath and TFA (6.5 mL) was added. Hydrogen peroxide (30 wt%, 15.000 mmol, 1.5000 equiv, 1610.0 μ L) was added in a steady stream. The resulting solution was left to stir at rt overnight. Additional aliquots of hydrogen peroxide (30 wt%, 5.000 mmol, 0.5000 equiv, 537.0 μ L) were added daily until the starting material was completely consumed as determined by SFC-MS. The reaction was then diluted with chloroform (20 mL) and neutralized via the addition of 6 M NaOH. The biphasic mixture was transferred to a separatory funnel, and the organic layer isolated. The organic layer was washed with 6 M NaOH (2 \times 10 mL), dried over MgSO₄, filtered, and the filtrate was concentrated to yield a mixture of the starting material and desired product. The product was used without further characterization or purification.



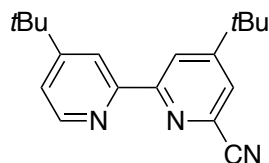
4,4'-di-methoxy-[2,2'-bipyridine]-6-carbonitrile (5.L2) was prepared by modification of the literature procedure.¹⁷

A flame-dried 50 mL round-bottom flask equipped with a PTFE-coated stir bar was charged with 4,4'-di-methoxy-[2,2'-bipyridine]-1-oxide (464.5 mg, 2.000 mmol, 1.000 equiv). The flask was sealed with a rubber septum and purged with nitrogen for 5 min. Under positive pressure of nitrogen, anhydrous DCM (5 mL) was added to the flask. The reaction was then cooled to 0 °C and trimethylsilyl cyanide (992.1 mg, 10.00 mmol, 5.000 equiv, 1251 μ L) was slowly added over the course of 5 min via syringe. Afterwards, benzoyl chloride (562.3 mg, 4.000 mmol, 2.000 equiv, 465.0 μ L) was added dropwise over the course of 5 min. The reaction mixture was allowed to warm to rt while stirring for 24 h. After stirring, a 10% solution of NaHCO₃ in H₂O was slowly added until gas evolution ceased, and the resulting biphasic mixture was stirred at rt for 24 h. The mixture was poured into a separatory funnel and the organic layer was set aside. The aqueous layer was extracted with DCM (2 \times 10 mL), and the combined organic layers were dried over MgSO₄, filtered, and concentrated. The resulting residue was purified by column chromatography (40 g of silica gel, 35% EtOAc/hexanes for 1 CV, then 35–60% EtOAc/hexanes across 25 CV) to yield the product (192.2 mg, 0.7972 mmol, 40%) as a light pink solid.

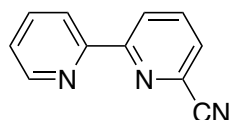
¹H NMR (500 MHz, CDCl₃) δ 8.47 (d, J = 5.6 Hz, 1H), 8.20 (d, J = 2.4 Hz, 1H), 8.02 (d, J = 2.6 Hz, 1H), 7.23 (d, J = 2.4 Hz, 1H), 6.89 (dd, J = 5.7, 2.6 Hz, 1H), 4.00 (s, 3H), 3.97 (s, 3H).

¹³C{¹H} NMR (126 MHz, CDCl₃) δ 166.9, 166.8, 159.3, 155.9, 150.2, 133.9, 117.4, 116.4, 111.9, 108.7, 106.7, 56.0, 55.5.

HRMS-ESI (m/z): [M+H]⁺ calcd for C₁₃H₁₂N₃O₂⁺, 242.0924; found, 242.0924.



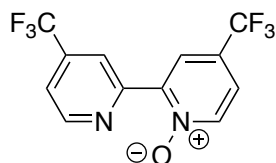
4,4'-di-tert-butyl-[2,2'-bipyridine]-6-carbonitrile (5.L3) was synthesized according to the literature procedure and characterization data matched those reported in the literature.¹⁷



2,2'-bipyridine-6-carbonitrile (5.L4) was synthesized by a former lab member and characterization data matched those reported in the literature.

¹H NMR (500 MHz, CDCl₃) δ 8.70 (dd, *J* = 1.8, 0.9 Hz, 1H), 8.68 (dd, *J* = 8.2, 1.1 Hz, 1H), 8.47 (dt, *J* = 8.1, 1.1 Hz, 1H), 7.95 (t, *J* = 7.9 Hz, 1H), 7.86 (td, *J* = 7.8, 1.8 Hz, 1H), 7.70 (dd, *J* = 7.6, 1.1 Hz, 1H), 7.38 (ddd, *J* = 7.6, 4.8, 1.2 Hz, 1H).

¹³C{¹H} NMR (126 MHz, CDCl₃) δ 157.7, 154.0, 149.3, 137.9, 137.2, 133.2, 128.1, 124.8, 124.2, 121.6, 117.4.



4,4'-bis(trifluoromethyl)-[2,2'-bipyridine] 1-oxide (5.L5a)

To a 50 mL round-bottom flask equipped with a PTFE-coated stir bar was charged with 4,4'-bis-(trifluoromethyl)-2,2'-bipyridine (1460.9 mg, 5.0000 mmol, 1.0000 equiv). The flask was submerged in a water bath and TFA (3.25 mL) was added. While stirring, hydrogen peroxide was added in a steady stream (30 wt%, 7.500 mmol, 1.500 equiv, 850.3

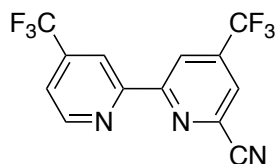
μL). The resulting solution was left to stir at rt overnight. The reaction was then diluted with chloroform (10 mL) and neutralized via the slow addition of 6 M NaOH. The mixture was then transferred to a separatory funnel and the organic layer isolated. The organic layer was then washed with 6 M NaOH (2×5 mL), dried over MgSO_4 , filtered, and concentrated. The resulting residue was purified by column chromatography (ISCO, 40 g silica, 1 CV hexanes, then 0–40% acetone/hexanes across 25 CV) to yield the desired product (271.9 mg, 0.8823 mmol, 18% yield) as a white solid. The remaining mass balance was recovered as the equivalent 1,1'-dioxide.

$^1\text{H NMR}$ (500 MHz, CDCl_3) δ 9.36 – 9.31 (m, 1H), 8.94 (d, $J = 5.0$ Hz, 1H), 8.63 (d, $J = 2.2$ Hz, 1H), 8.40 (d, $J = 6.8$ Hz, 0H), 7.63 (dd, $J = 5.0, 0.9$ Hz, 1H), 7.52 (dd, $J = 6.8, 2.8$ Hz, 1H).

$^{13}\text{C}\{^1\text{H}\}$ NMR (126 MHz, CDCl_3) δ 150.2, 149.5, 146.4, 141.6, 139.1 (q, $J = 34.4$ Hz), 126.9 (q, $J = 35.6$ Hz), 125.0 (q, $J = 4.0$ Hz), 122.6 (q, $J = 273.6$ Hz), 122.5 (q, $J = 272.1$ Hz), 122.0 (q, $J = 3.5$ Hz), 121.1 (q, $J = 3.8$ Hz), 120.6 (q, $J = 3.5$ Hz).

$^{19}\text{F}\{^1\text{H}\}$ NMR (377 MHz, CDCl_3) δ -63.61, -64.69.

HRMS-ESI (m/z): $[\text{M}+\text{H}]^+$ calcd for $\text{C}_{12}\text{H}_7\text{F}_6\text{N}_2\text{O}^+$, 309.0457; found, 309.0451.



4,4'-bis-(trifluoromethyl)-[2,2'-bipyridine]-6-carbonitrile (5.L5) was prepared by modification of the literature procedure.¹⁷

A flame-dried 50 mL round-bottom flask equipped with a PTFE-coated stir bar was charged with 4,4'-bis-(trifluoromethyl)-[2,2'-bipyridine]-1-oxide (154.1 mg, 0.5000 mmol, 1.000 equiv). The flask was sealed with a rubber septum and purged with nitrogen for 5

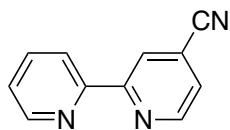
min. Under positive pressure of nitrogen, anhydrous DCM (3 mL) was added to the flask. The reaction was then cooled to 0 °C and trimethylsilyl cyanide (248.0 mg, 2.500 mmol, 5.000 equiv, 312.8 μ L) was slowly added over the course of 5 min. Following this, benzoyl chloride (140.6 mg, 1.000 mmol, 2.000 equiv, 116.2 μ L) was added dropwise over the course of 5 min. The reaction mixture was allowed to warm to rt while stirring for 24 h. After this time, a 10% solution of NaHCO₃ in H₂O was slowly added until gas evolution stopped, and the resulting biphasic mixture was stirred at rt for 24 h. The mixture was then poured into a separatory funnel and the organic layer set aside. The aqueous layer was extracted with DCM (2 \times 10 mL), and the combined organic layers were dried over MgSO₄, filtered, and concentrated. The resulting residue was purified by column chromatography (40 g of silica gel, hexanes for 1 CV, then 0–20% EtOAc/hexanes across 15 CV) to yield the product (147.4 mg, 0.4670 mmol, 93%) as a white solid.

¹H NMR (500 MHz, CDCl₃) δ 8.98 (d, *J* = 0.8 Hz, 1H), 8.92 (d, *J* = 5.0 Hz, 2H), 8.74 (d, *J* = 0.9 Hz, 1H), 7.96 (d, *J* = 1.4 Hz, 1H), 7.67 (dd, *J* = 4.6, 1.4 Hz, 2H).

¹³C{¹H} NMR (126 MHz, CDCl₃) δ 157.9, 154.0, 150.6, 141.2 (q, *J* = 35.4 Hz), 140.1 (q, *J* = 34.7 Hz), 134.5, 124.3 (q, *J* = 3.5 Hz), 122.6 (q, *J* = 273.6 Hz), 121.8 (q, *J* = 274.1 Hz), 121.1 (q, *J* = 3.5 Hz), 120.5 (q, *J* = 3.6 Hz), 117.7 (q, *J* = 3.7 Hz), 116.0.

¹⁹F{¹H} NMR (377 MHz, CDCl₃) δ -64.79, -64.85.

HRMS-ESI (*m/z*): [M+H]⁺ calcd for C₁₃H₆F₆N₃⁺, 318.0460; found, 318.0455.



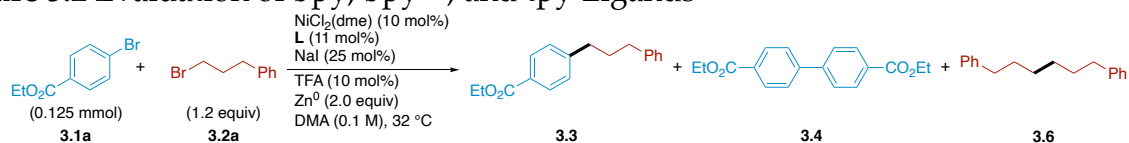
2,2'-bipyridine-4-carbonitrile (5.L7)

In a nitrogen-filled glovebox, an oven-dried 50 mL two-neck flask equipped with a PTFE-coated stir bar was charged with tetrakis(triphenylphosphine)palladium(0) (138.7 mg, 0.1200 mmol, 0.06000 equiv) and 2-bromoisonicotinonitrile (366.0 mg, 2.000 mmol, 1.000 equiv). The flask was sealed with a rubber septum and removed from the glovebox. The flask was equipped with a condenser via the top neck and the flask was purged with nitrogen. Anhydrous toluene (20 mL) and 2-(tributylstannyl)pyridine (809.9 mg, 2.200 mmol, 1.100 equiv, 712.3 μ L) were added, then the contents were heated to reflux and stirred for 4 days. After stirring, the reaction mixture was allowed to cool to rt and was filtered through a plug of Celite pre-wetted with DCM, and the filter cake was washed with DCM (3 \times 25 mL). The filtrate was concentrated, and the resulting residue was purified by column chromatography to yield the product (200.7 mg, 1.108 mmol, 55%) as a white solid.

$^1\text{H NMR}$ (500 MHz, CDCl_3) δ 8.84 (dd, $J = 4.9, 0.9$ Hz, 1H), 8.73 – 8.69 (overlapping signals, 2H), 8.43 (dt, $J = 8.0, 1.1$ Hz, 1H), 7.86 (td, $J = 7.8, 1.8$ Hz, 1H), 7.52 (dd, $J = 5.0, 1.6$ Hz, 1H), 7.38 (ddd, $J = 7.5, 4.8, 1.2$ Hz, 1H).

$^{13}\text{C}\{^1\text{H}\}$ NMR (126 MHz, CDCl_3) δ 157.6, 154.1, 150.0, 149.5, 137.2, 124.8, 124.7, 123.0, 121.4, 121.3, 116.7.

5.1.3.3 Results of Ligand Screens

Figure 5.2 Evaluation of bpy, bpy^{CN}, and tpy Ligands^a

Entry	Ligand	3.3 (%)	3.4 (%)	3.6 (%)
1	3.L2	67	6	20 ^b
2	3.L1	44	21	26 ^b
3	5.L1	41	22	26 ^b
4	3.L12	38	25	16 ^b
5	3.L9	13	31	6 ^b
6	5.L2	43	5	35
7	5.L3	49	6	30
8	3.L23	45	5	32
9	5.L4	53	3	26
10	5.L5	65	4	12
11	5.L6	32	5	23
12	5.L7	55	12	20

^aReactions were assembled in a nitrogen filled glovebox according to General Procedure C with ethyl 4-bromobenzoate and 1-bromo-3-phenylpropane. Yields and selectivity were determined by GC-FID. ^b3.6 was not observed until after complete consumption of 3.1a.

5.1.3.4 General Computational Method

Please refer to the general information in Section 3.4.1, the general procedure in Section 3.4.3.1, and the computational details in Section 3.4.5. All procedures are as referenced unless otherwise specified. All energies are provided in kcal/mol and are normalized relative to the lowest-energy isomer.

5.1.3.5 Computational Results

Optimized geometries and energies can be found in Scheme 5.3.

5.2 Initial Studies on the Impact of Ligand Structure in Decarbonylative Cross-Electrophile Coupling

5.2.1 Introduction

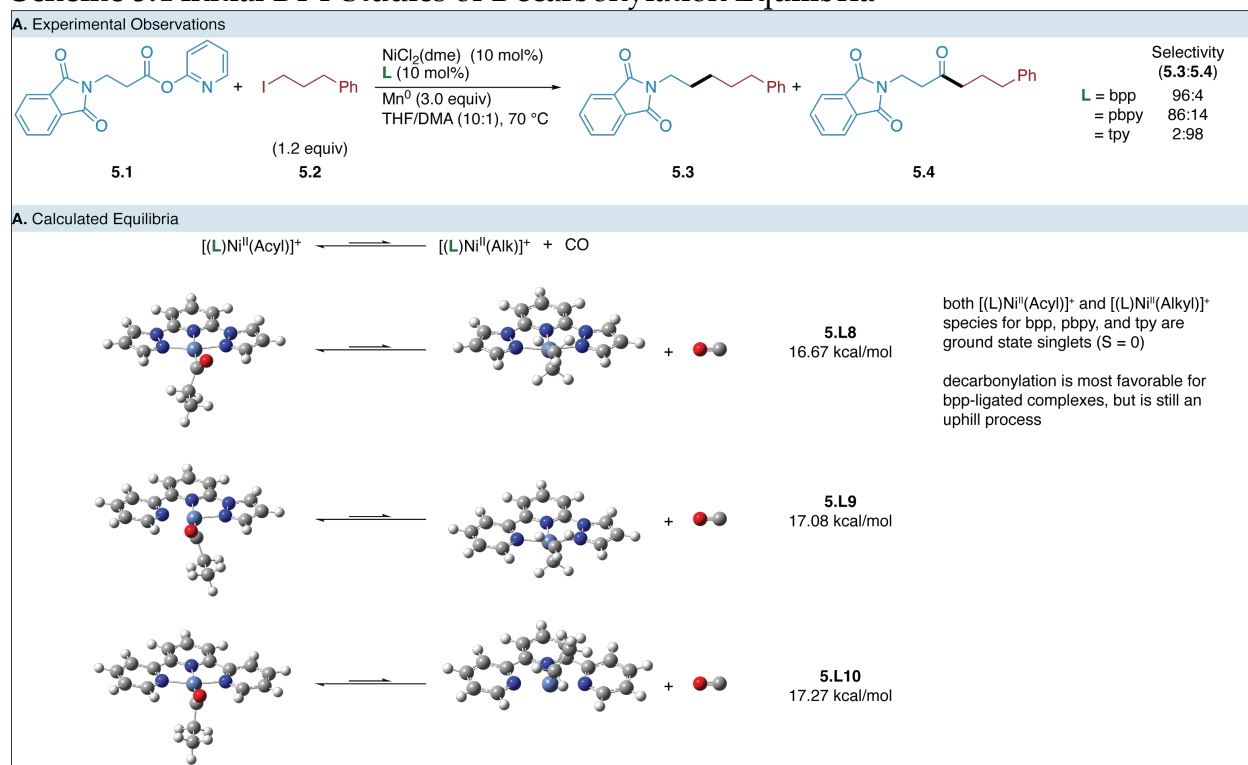
Decarbonylative XEC offers an attractive method to generate alkylnickel species via a two-electron pathway. This approach offers a direct translation of successful strategies for C(sp²)-C(sp³) XEC to C(sp³)-C(sp³) bond formation while avoiding non-selective radical-radical couplings, or the in situ generation of alkyl nucleophiles. Recently, our group and others have published methods for the decarbonylative XEC of benzoic acid derivatives and alkyl electrophiles.^{111,112} Unpublished work in the group has worked to translate this chemistry to alkanolic acid derivatives, enabling a general two- and one-electron C(sp³)-C(sp³) XEC. Over the course of these studies, distinct trends were observed relating the ligand identity with the proportion of alkyl-alkyl cross-coupled product, and acyl-alkyl product. This ketone derivative results from inefficient CO extrusion from the intermediate (L)Ni^{II}(Acyl)X complex. As decarbonylation, and CO extrusion have been shown to be reversible, we hypothesized that a brief computational campaign investigating the thermodynamic equilibrium between acylnickel and alkylnickel may help rationalize the effect of ligand structure on the reaction outcome.

5.2.2 Results

We investigated the equilibrium between [(L)Ni^{II}(Acyl)]⁺ and [(L)Ni^{II}(Alk)]⁺ for three ligands, bpp, 6-pyrrazol-1-yl-2,2'-bipyridine, and tpy. Experiments had demonstrated that amongst this series, the proportion of alkyl-alkyl to acyl-alkyl cross-coupled product decreased. First, we established that all catalytically relevant species assume a singlet multiplicity in the ground state (Scheme 5.4). We then went on to

investigate the thermodynamic equilibrium for each ligand. Indeed, in accordance with the experimental observations, the equilibrium with bpp as the ligand favored the $[(L)Ni^{II}(Alk)]^+$ complex the most. Notably, decarbonylation and CO extrusion from the $[(L)Ni^{II}(Acyl)]^+$ complex was not favorable with any of the studied ligands. This may inform the high temperatures and large reaction headspace necessary to drive the equilibrium and acquire reasonable amounts of alkyl-alkyl cross-coupled product. However, the relatively small differences in energy do not account for the large differences in selectivity for the desired product over the equivalent ketone. It is currently unclear if this is due to chelation effects in the experimental substrate, or other unaccounted for factors. One possibility is that the reaction proceeds through an intermediate reduction from $[(L)Ni^{II}(Acyl)]^+$ to $(L)Ni^I(Acyl)$ intermediate. Given recent work by Doyle and Sigman which specifically highlights the stability of nickel(I) complexes using these ligands, it would be beneficial to also investigate the equilibrium between $(L)Ni^I(Acyl)$ and $(L)Ni^I(Alkyl)$.³⁸ If the energetic differences are exacerbated in this lower oxidation state, this may inform further experimental mechanistic study.

Scheme 5.4 Initial DFT Studies of Decarbonylation Equilibria



5.2.3 Discussion and Future Work

Further studies into this critical equilibrium is warranted. Informed by electrochemical work, we will investigate the decarbonylation of $(\text{L})\text{Ni}^{\text{I}}(\text{Acyl})$ complexes to determine if computational values better match experimental observations. DFT-optimized structures and energies cannot easily mirror the dynamic exchange of CO from the nickel center to the reaction solvent, and into the reaction headspace, they do support experimental observations. Further, given the observed trend, it is possible that a statistical model may be developed to relate molecular descriptors of either the acylnickel or alkylnickel complex with the observed selectivity for alkyl-alkyl or acyl-alkyl XEC. This model can then be utilized to design and validate improved ligands for this coupling via virtual screening.

5.2.4 Experimental

5.2.4.1 General Computational Method

All computations were performed using the Gaussian 16, Rev. C.01 suite using defaults unless noted otherwise.⁵¹ Optimized structures are visualized using GaussView 6.0.10.⁵² The “ultrafine” integration grid setting was used in all computations. Each structure was calculated by performing geometry optimization with the unrestricted M06 functional⁵⁴ and the cc-pVDZ basis set,^{55,56} as well as the LANL2DZ effective core potential⁵⁷ for Ni. The frequency keyword “noraman” was used in all frequency calculations to increase computational efficiency. Gas phase single point energies were obtained using M06/cc-pVTZ, SDD(Ni).⁵⁸ Corrections for the solvation energies were obtained from the difference between single points with the SMD continuum solvation method for THF (tetrahydrofuran)⁵⁹ and a gas phase single point, both using M06/cc-pVTZ,SDD(Ni). Conformers of higher energy were accounted for in all cases and are not included in the discussion. Stationary points were characterized as ground states by the absence of negative eigenvalues (zero imaginary frequencies) in frequency analysis at the same level of theory as the geometry optimization. All energies are provided in kcal/mol.

References

- (1) Ananikov, V. P. Nickel: The “Spirited Horse” of Transition Metal Catalysis. *ACS Catal.* **2015**, *5* (3), 1964–1971. <https://doi.org/10.1021/acscatal.5b00072>.
- (2) Beutner, G. L.; Simmons, E. M.; Ayers, S.; Bemis, C. Y.; Goldfogel, M. J.; Joe, C. L.; Marshall, J.; Wisniewski, S. R. A Process Chemistry Benchmark for Sp^2 – Sp^3 Cross Couplings. *J. Org. Chem.* **2021**, *86* (15), 10380–10396. <https://doi.org/10.1021/acs.joc.1c01073>.
- (3) Weix, D. J. Methods and Mechanisms for Cross-Electrophile Coupling of Csp^2 Halides with Alkyl Electrophiles. *Acc. Chem. Res.* **2015**, *48* (6), 1767–1775. <https://doi.org/10.1021/acs.accounts.5b00057>.
- (4) Rudolph, A.; Lautens, M. Secondary Alkyl Halides in Transition-Metal-Catalyzed Cross-Coupling Reactions. *Angew. Chem. Int. Ed.* **2009**, *48* (15), 2656–2670. <https://doi.org/10.1002/anie.200803611>.
- (5) Ni, S.; Zhang, W.; Mei, H.; Han, J.; Pan, Y. Ni-Catalyzed Reductive Cross-Coupling of Amides with Aryl Iodide Electrophiles via C–N Bond Activation. *Org. Lett.* **2017**, *19* (10), 2536–2539. <https://doi.org/10.1021/acs.orglett.7b00831>.
- (6) Biswas, S.; Weix, D. J. Mechanism and Selectivity in Nickel-Catalyzed Cross-Electrophile Coupling of Aryl Halides with Alkyl Halides. *J. Am. Chem. Soc.* **2013**, *135* (43), 16192–16197. <https://doi.org/10.1021/ja407589e>.
- (7) Chen, T. Q.; MacMillan, D. W. C. A Metallaphotoredox Strategy for the Cross-Electrophile Coupling of α -Chloro Carbonyls with Aryl Halides. *Angew. Chem.* **2019**, *131* (41), 14726–14730. <https://doi.org/10.1002/ange.201909072>.
- (8) Wang, J.; Hoerrner, M. E.; Watson, M. P.; Weix, D. J. Nickel-Catalyzed Synthesis of Dialkyl Ketones from the Coupling of N-Alkyl Pyridinium Salts with Activated Carboxylic Acids. *Angew. Chem. Int. Ed.* **2020**, *59* (32), 13484–13489. <https://doi.org/10.1002/anie.202002271>.
- (9) Shrestha, R.; Weix, D. J. Reductive Conjugate Addition of Haloalkanes to Enones To Form Silyl Enol Ethers. *Org. Lett.* **2011**, *13* (10), 2766–2769. <https://doi.org/10.1021/ol200881v>.
- (10) Kang, K.; Weix, D. J. Nickel-Catalyzed $C(Sp^3)$ – $C(Sp^3)$ Cross-Electrophile Coupling of In Situ Generated NHP Esters with Unactivated Alkyl Bromides. *Org. Lett.* **2022**, *24* (15), 2853–2857. <https://doi.org/10.1021/acs.orglett.2c00805>.
- (11) Baker, K. M.; Bercher, O. P.; Twitty, J. C.; Mortimer, T.; Watson, M. P. 2,6-Bis(Pyrazol-1-yl)Pyridine (1-Bpp) as a General Ligand for the Negishi Alkylation of Alkylpyridinium Salts. *J. Org. Chem.* **2023**, *acs.joc.3c00665*. <https://doi.org/10.1021/acs.joc.3c00665>.
- (12) Joshi-Pangu, A.; Ganesh, M.; Biscoe, M. R. Nickel-Catalyzed Negishi Cross-Coupling Reactions of Secondary Alkylzinc Halides and Aryl Iodides. *Org. Lett.* **2011**, *13* (5), 1218–1221. <https://doi.org/10.1021/ol200098d>.
- (13) Winter, A.; Schubert, U. S. Metal-Terpyridine Complexes in Catalytic Application – A Spotlight on the Last Decade. *ChemCatChem* **2020**, *12* (11), 2890–2941. <https://doi.org/10.1002/cctc.201902290>.
- (14) Hansen, E. C.; Pedro, D. J.; Wotal, A. C.; Gower, N. J.; Nelson, J. D.; Caron, S.; Weix, D. J. New Ligands for Nickel Catalysis from Diverse Pharmaceutical Heterocycle Libraries. *Nat. Chem.* **2016**, *8* (12), 1126–1130. <https://doi.org/10.1038/nchem.2587>.

- (15) Hansen, E. C.; Li, C.; Yang, S.; Pedro, D.; Weix, D. J. Coupling of Challenging Heteroaryl Halides with Alkyl Halides via Nickel-Catalyzed Cross-Electrophile Coupling. *J. Org. Chem.* **2017**, *82* (14), 7085–7092. <https://doi.org/10.1021/acs.joc.7b01334>.
- (16) Aguirre, A. L.; Loud, N. L.; Johnson, K. A.; Weix, D. J.; Wang, Y. ChemBead Enabled High-Throughput Cross-Electrophile Coupling Reveals a New Complementary Ligand. *Chem. Eur. J.* **2021**, *27* (51), 12981–12986. <https://doi.org/10.1002/chem.202102347>.
- (17) Chi, B. K.; Widness, J. K.; Gilbert, M. M.; Salgueiro, D. C.; Garcia, K. J.; Weix, D. J. In-Situ Bromination Enables Formal Cross-Electrophile Coupling of Alcohols with Aryl and Alkenyl Halides. *ACS Catal.* **2022**, *12* (1), 580–586. <https://doi.org/10.1021/acscatal.1c05208>.
- (18) Fu, J.; Lundy, W.; Chowdhury, R.; Twitty, J. C.; Dinh, L. P.; Sampson, J.; Lam, Y.; Sevov, C. S.; Watson, M. P.; Kalyani, D. Nickel-Catalyzed Electroreductive Coupling of Alkylpyridinium Salts and Aryl Halides. *ACS Catal.* **2023**, *13* (14), 9336–9345. <https://doi.org/10.1021/acscatal.3c01939>.
- (19) Hammett, L. P. Some Relations between Reaction Rates and Equilibrium Constants. *Chem. Rev.* **1935**, *17* (1), 125–136. <https://doi.org/10.1021/cr60056a010>.
- (20) Taft, R. W. Linear Free Energy Relationships from Rates of Esterification and Hydrolysis of Aliphatic and Ortho-Substituted Benzoate Esters. *J. Am. Chem. Soc.* **1952**, *74* (11), 2729–2732. <https://doi.org/10.1021/ja01131a010>.
- (21) Charton, M. Steric Effects. I. Esterification and Acid-Catalyzed Hydrolysis of Esters. *J. Am. Chem. Soc.* **1975**, *97* (6), 1552–1556. <https://doi.org/10.1021/ja00839a047>.
- (22) Verloop, A.; Hoogenstraaten, W.; Tipker, J. Development and Application of New Steric Substituent Parameters in Drug Design. In *Drug Design*; Elsevier, 1976; pp 165–207. <https://doi.org/10.1016/B978-0-12-060307-7.50010-9>.
- (23) Hillier, A. C.; Sommer, W. J.; Yong, B. S.; Petersen, J. L.; Cavallo, L.; Nolan, S. P. A Combined Experimental and Theoretical Study Examining the Binding of N - Heterocyclic Carbenes (NHC) to the Cp^{*}RuCl (Cp^{*} = η⁵-C₅Me₅) Moiety: Insight into Stereoelectronic Differences between Unsaturated and Saturated NHC Ligands. *Organometallics* **2003**, *22* (21), 4322–4326. <https://doi.org/10.1021/om034016k>.
- (24) Van Leeuwen, P. W. N. M.; Kamer, P. C. J.; Reek, J. N. H.; Dierkes, P. Ligand Bite Angle Effects in Metal-Catalyzed C–C Bond Formation. *Chem. Rev.* **2000**, *100* (8), 2741–2770. <https://doi.org/10.1021/cr9902704>.
- (25) Williams, W. L.; Zeng, L.; Gensch, T.; Sigman, M. S.; Doyle, A. G.; Anslyn, E. V. The Evolution of Data-Driven Modeling in Organic Chemistry. *ACS Cent. Sci.* **2021**, *7* (10), 1622–1637. <https://doi.org/10.1021/acscentsci.1c00535>.
- (26) Santiago, C. B.; Guo, J.-Y.; Sigman, M. S. Predictive and Mechanistic Multivariate Linear Regression Models for Reaction Development. *Chem. Sci.* **2018**, *9* (9), 2398–2412. <https://doi.org/10.1039/C7SC04679K>.
- (27) Tolman, C. A. Steric Effects of Phosphorus Ligands in Organometallic Chemistry and Homogeneous Catalysis. *Chem. Rev.* **1977**, *77* (3), 313–348. <https://doi.org/10.1021/cr60307a002>.
- (28) Fey, N.; Tsipis, A. C.; Harris, S. E.; Harvey, J. N.; Orpen, A. G.; Mansson, R. A. Development of a Ligand Knowledge Base, Part 1: Computational Descriptors for Phosphorus Donor Ligands. *Chem. Eur. J.* **2006**, *12* (1), 291–302. <https://doi.org/10.1002/chem.200500891>.

- (29) Crawford, J. M.; Gensch, T.; Sigman, M. S.; Elward, J. M.; Steves, J. E. Impact of Phosphine Featurization Methods in Process Development. *Org. Process Res. Dev.* **2022**, *26* (4), 1115–1123. <https://doi.org/10.1021/acs.oprd.1c00357>.
- (30) Wu, K.; Doyle, A. G. Parameterization of Phosphine Ligands Demonstrates Enhancement of Nickel Catalysis via Remote Steric Effects. *Nature Chem* **2017**, *9* (8), 779–784. <https://doi.org/10.1038/nchem.2741>.
- (31) Newman-Stonebraker, S. H.; Smith, S. R.; Borowski, J. E.; Peters, E.; Gensch, T.; Johnson, H. C.; Sigman, M. S.; Doyle, A. G. Univariate Classification of Phosphine Ligation State and Reactivity in Cross-Coupling Catalysis. *Science* **2021**, *374* (6565), 301–308. <https://doi.org/10.1126/science.abj4213>.
- (32) Gensch, T.; dos Passos Gomes, G.; Friederich, P.; Peters, E.; Gaudin, T.; Pollice, R.; Jorner, K.; Nigam, A.; Lindner-D'Addario, M.; Sigman, M. S.; Aspuru-Guzik, A. A Comprehensive Discovery Platform for Organophosphorus Ligands for Catalysis. *J. Am. Chem. Soc.* **2022**, *144* (3), 1205–1217. <https://doi.org/10.1021/jacs.1c09718>.
- (33) *Phosphine Predictor* | *Sigma-Aldrich*. <https://www.sigmaaldrich.com/deepweb/assets/sigmaaldrich/product/documents/377/478/phosphine-predictor-br80087en-ms.pdf> (accessed 2023-07-08).
- (34) Zhang, C.; Santiago, C. B.; Crawford, J. M.; Sigman, M. S. Enantioselective Dehydrogenative Heck Arylations of Trisubstituted Alkenes with Indoles to Construct Quaternary Stereocenters. *J. Am. Chem. Soc.* **2015**, *137* (50), 15668–15671. <https://doi.org/10.1021/jacs.5b11335>.
- (35) Guo, J.-Y.; Minko, Y.; Santiago, C. B.; Sigman, M. S. Developing Comprehensive Computational Parameter Sets To Describe the Performance of Pyridine-Oxazoline and Related Ligands. *ACS Catal.* **2017**, *7* (6), 4144–4151. <https://doi.org/10.1021/acscatal.7b00739>.
- (36) Woods, B. P.; Orlandi, M.; Huang, C.-Y.; Sigman, M. S.; Doyle, A. G. Nickel-Catalyzed Enantioselective Reductive Cross-Coupling of Styrenyl Aziridines. *J. Am. Chem. Soc.* **2017**, *139* (16), 5688–5691. <https://doi.org/10.1021/jacs.7b03448>.
- (37) Lau, S. H.; Borden, M. A.; Steiman, T. J.; Wang, L. S.; Parasram, M.; Doyle, A. G. Ni/Photoredox-Catalyzed Enantioselective Cross-Electrophile Coupling of Styrene Oxides with Aryl Iodides. *J. Am. Chem. Soc.* **2021**, *143* (38), 15873–15881. <https://doi.org/10.1021/jacs.1c08105>.
- (38) Tang, T.; Hazra, A.; Min, D. S.; Williams, W. L.; Jones, E.; Doyle, A. G.; Sigman, M. S. Interrogating the Mechanistic Features of Ni(I)-Mediated Aryl Iodide Oxidative Addition Using Electroanalytical and Statistical Modeling Techniques. *J. Am. Chem. Soc.* **2023**, *jacs.3c01726*. <https://doi.org/10.1021/jacs.3c01726>.
- (39) Shi, R.; Zhang, Z.; Hu, X. Nickamine and Analogous Nickel Pincer Catalysts for Cross-Coupling of Alkyl Halides and Hydrosilylation of Alkenes. *Acc. Chem. Res.* **2019**, *52* (5), 1471–1483. <https://doi.org/10.1021/acs.accounts.9b00118>.
- (40) Primer, D. N.; Molander, G. A. Enabling the Cross-Coupling of Tertiary Organoboron Nucleophiles through Radical-Mediated Alkyl Transfer. *J. Am. Chem. Soc.* **2017**, *139* (29), 9847–9850. <https://doi.org/10.1021/jacs.7b06288>.
- (41) Wang, H.; Han, W.; Noble, A.; Aggarwal, V. K. Dual Nickel/Photoredox-Catalyzed Site-Selective Cross-Coupling of 1,2-Bis-Boronic Esters Enabled by 1,2-Boron Shifts. *Angew Chem Int Ed* **2022**, *61* (34). <https://doi.org/10.1002/anie.202207988>.
- (42) Yuan, M.; Song, Z.; Badir, S. O.; Molander, G. A.; Gutierrez, O. On the Nature of C(Sp³)–C(Sp²) Bond Formation in Nickel-Catalyzed Tertiary Radical Cross-

- Couplings: A Case Study of Ni/Photoredox Catalytic Cross-Coupling of Alkyl Radicals and Aryl Halides. *J. Am. Chem. Soc.* **2020**, *142* (15), 7225–7234. <https://doi.org/10.1021/jacs.0c02355>.
- (43) Chen, T.; Zhang, H.; Mykhailiuk, P. K.; Merchant, R. R.; Smith, C. A.; Qin, T.; Baran, P. S. Quaternary Centers by Nickel-Catalyzed Cross-Coupling of Tertiary Carboxylic Acids and (Hetero)Aryl Zinc Reagents. *Angew. Chem. Int. Ed.* **2019**, *58* (8), 2454–2458. <https://doi.org/10.1002/anie.201814524>.
- (44) Gilbert, M. M.; Trenerry, M. J.; Longley, V. R.; Berry, J. F.; Weix, D. J. Ligand-Metal Cooperation Enables C-C Activation Cross-Coupling Reactivity of Cyclopropyl Ketones. *ChemRxiv* **2021**. <https://doi.org/10.33774/chemrxiv-2021-hjdbr>.
- (45) Wang, J.; Cary, B. P.; Beyer, P. D.; Gellman, S. H.; Weix, D. J. Ketones from Nickel-Catalyzed Decarboxylative, Non-Symmetric Cross-Electrophile Coupling of Carboxylic Acid Esters. *Angew. Chem. Int. Ed.* **2019**, *58* (35), 12081–12085. <https://doi.org/10.1002/anie.201906000>.
- (46) Gilbert, M.; Trenerry, M.; Longley, V.; Castro, A.; Berry, J.; Weix, D. *Ligand-Metal Cooperation Enables Net C–C Activation Cross-Coupling Reactivity of Cyclopropyl Ketones*; preprint; Chemistry, 2023. <https://doi.org/10.26434/chemrxiv-2021-hjdbr-v3>.
- (47) Perkins, R. J.; Hughes, A. J.; Weix, D. J.; Hansen, E. C. Metal-Reductant-Free Electrochemical Nickel-Catalyzed Couplings of Aryl and Alkyl Bromides in Acetonitrile. *Org. Process Res. Dev.* **2019**, *23* (8), 1746–1751. <https://doi.org/10.1021/acs.oprd.9b00232>.
- (48) Franke, M. C.; Longley, V. R.; Rafiee, M.; Stahl, S. S.; Hansen, E. C.; Weix, D. J. Zinc-Free, Scalable Reductive Cross-Electrophile Coupling Driven by Electrochemistry in an Undivided Cell. *ACS Catal.* **2022**, *12* (20), 12617–12626. <https://doi.org/10.1021/acscatal.2c03033>.
- (49) Biswas, S.; Qu, B.; Desrosiers, J.-N.; Choi, Y.; Haddad, N.; Yee, N. K.; Song, J. J.; Senanayake, C. H. Nickel-Catalyzed Cross-Electrophile Reductive Couplings of Neopentyl Bromides with Aryl Bromides. *J. Org. Chem.* **2020**, *85* (12), 8214–8220. <https://doi.org/10.1021/acs.joc.0c00549>.
- (50) Lustosa, D. M.; Milo, A. Mechanistic Inference from Statistical Models at Different Data-Size Regimes. *ACS Catal.* **2022**, *12* (13), 7886–7906. <https://doi.org/10.1021/acscatal.2c01741>.
- (51) Frisch, M. J.; Trucks, G. W.; Schlegel, H. B.; Scuseria, G. E.; Robb, M. A.; Cheeseman, J. R.; Scalmani, G.; Barone, V.; Petersson, G. A.; Nakatsuji, H.; Li, X.; Caricato, M.; Marenich, A. V.; Bloino, J.; Janesko, B. G.; Gomperts, R.; Mennucci, B.; Hratchian, H. P.; Ortiz, J. V.; Izmaylov, A. F.; Sonnenberg, J. L.; Williams; Ding, F.; Lipparini, F.; Egidi, F.; Goings, J.; Peng, B.; Petrone, A.; Henderson, T.; Ranasinghe, D.; Zakrzewski, V. G.; Gao, J.; Rega, N.; Zheng, G.; Liang, W.; Hada, M.; Ehara, M.; Toyota, K.; Fukuda, R.; Hasegawa, J.; Ishida, M.; Nakajima, T.; Honda, Y.; Kitao, O.; Nakai, H.; Vreven, T.; Throssell, K.; Montgomery Jr., J. A.; Peralta, J. E.; Ogliaro, F.; Bearpark, M. J.; Heyd, J. J.; Brothers, E. N.; Kudin, K. N.; Staroverov, V. N.; Keith, T. A.; Kobayashi, R.; Normand, J.; Raghavachari, K.; Rendell, A. P.; Burant, J. C.; Iyengar, S. S.; Tomasi, J.; Cossi, M.; Millam, J. M.; Klene, M.; Adamo, C.; Cammi, R.; Ochterski, J. W.; Martin, R. L.; Morokuma, K.; Farkas, O.; Foresman, J. B.; Fox, D. J. *Gaussian 16 Rev. C.01*, 2016.
- (52) Dennington, R.; Keith, T. A.; Millam, J. M. *GaussView*, 2016.
- (53) Glendening, E. D.; Badenhoop, J. K.; Reed, A. E.; Carpenter, J. E.; Bohmann, J. A.; Morales, C. M.; Karafiloglou, P.; Landis, C. R.; Weinhold, F. *NBO 7.0.10*, 2018.

- (54) Zhao, Y.; Truhlar, D. G. The M06 Suite of Density Functionals for Main Group Thermochemistry, Thermochemical Kinetics, Noncovalent Interactions, Excited States, and Transition Elements: Two New Functionals and Systematic Testing of Four M06-Class Functionals and 12 Other Functionals. *Theor. Chem. Acc.* **2008**, *120* (1), 215–241. <https://doi.org/10.1007/s00214-007-0310-x>.
- (55) Wilson, A. K.; Woon, D. E.; Peterson, K. A.; Dunning, T. H. Gaussian Basis Sets for Use in Correlated Molecular Calculations. IX. The Atoms Gallium through Krypton. *J. Chem. Phys.* **1999**, *110*, 7667–7676. <https://doi.org/10.1063/1.478678>.
- (56) Dunning, T. H., Jr. Gaussian Basis Sets for Use in Correlated Molecular Calculations. I. The Atoms Boron through Neon and Hydrogen. *J. Chem. Phys.* **1989**, *90* (2), 1007–1023. <https://doi.org/10.1063/1.456153>.
- (57) Hay, P. J.; Wadt, W. R. Ab Initio Effective Core Potentials for Molecular Calculations. Potentials for the Transition Metal Atoms Sc to Hg. *J. Chem. Phys.* **1985**, *82* (1), 270–283. <https://doi.org/10.1063/1.448799>.
- (58) Dolg, M.; Wedig, U.; Stoll, H.; Preuss, H. Energy-adjusted Ab Initio Pseudopotentials for the First Row Transition Elements. *J. Chem. Phys.* **1987**, *86* (2), 866–872. <https://doi.org/10.1063/1.452288>.
- (59) Marenich, A. V.; Cramer, C. J.; Truhlar, D. G. Universal Solvation Model Based on Solute Electron Density and on a Continuum Model of the Solvent Defined by the Bulk Dielectric Constant and Atomic Surface Tensions. *J. Phys. Chem. B.* **2009**, *113* (18), 6378–6396. <https://doi.org/10.1021/jp810292n>.
- (60) Greaves, M. E.; Johnson Humphrey, E. L. B.; Nelson, D. J. Reactions of Nickel(0) with Organochlorides, Organobromides, and Organoiodides: Mechanisms and Structure/Reactivity Relationships. *Catal. Sci. Technol.* **2021**, *11* (9), 2980–2996. <https://doi.org/10.1039/D1CY00374G>.
- (61) Thane, T. A.; Jarvo, E. R. Ligand-Based Control of Nickel Catalysts: Switching Chemoselectivity from One-Electron to Two-Electron Pathways in Competing Reactions of 4-Halotetrahydropyrans. *Org. Lett.* **2022**, *24* (28), 5003–5008. <https://doi.org/10.1021/acs.orglett.2c01335>.
- (62) Haibach, M. C.; Ickes, A. R.; Wilders, A. M.; Shekhar, S. Recent Advances in Nonprecious Metal Catalysis. *Org. Process Res. Dev.* **2020**, *24* (11), 2428–2444. <https://doi.org/10.1021/acs.oprd.0c00367>.
- (63) Hamby, T. B.; LaLama, M. J.; Sevov, C. S. Controlling Ni Redox States by Dynamic Ligand Exchange for Electroreductive Csp³–Csp² Coupling. *Science* **2022**, *376* (6591), 410–416. <https://doi.org/10.1126/science.abo0039>.
- (64) Richmond, E.; Moran, J. Recent Advances in Nickel Catalysis Enabled by Stoichiometric Metallic Reducing Agents. *Synthesis* **2018**, *50* (03), 499–513. <https://doi.org/10.1055/s-0036-1591853>.
- (65) Chan, A. Y.; Perry, I. B.; Bissonnette, N. B.; Buksh, B. F.; Edwards, G. A.; Frye, L. I.; Garry, O. L.; Lavagnino, M. N.; Li, B. X.; Liang, Y.; Mao, E.; Millet, A.; Oakley, J. V.; Reed, N. L.; Sakai, H. A.; Seath, C. P.; MacMillan, D. W. C. Metallaphotoredox: The Merger of Photoredox and Transition Metal Catalysis. *Chem. Rev.* **2022**, *122* (2), 1485–1542. <https://doi.org/10.1021/acs.chemrev.1c00383>.
- (66) Jutand, A. Contribution of Electrochemistry to Organometallic Catalysis. *Chem. Rev.* **2008**, *108* (7), 2300–2347. <https://doi.org/10.1021/cr068072h>.
- (67) Jose, J.; Diana, E. J.; Kanchana, U. S.; Mathew, T. V. Recent Advances in the Nickel-catalysed Electrochemical Coupling Reactions with a Focus on the Type of Bond

- Formed. *Asian J Org Chem* **2023**, *12* (2), e202200593 1-20. <https://doi.org/10.1002/ajoc.202200593>.
- (68) Franke, M. C.; Weix, D. J. Recent Advances in Electrochemical, Ni-Catalyzed C–C Bond Formation. *Israel Journal of Chemistry* **2023**, e202300089. <https://doi.org/10.1002/ijch.202300089>.
- (69) Lovering, F.; Bikker, J.; Humblet, C. Escape from Flatland: Increasing Saturation as an Approach to Improving Clinical Success. *J. Med. Chem.* **2009**, *52* (21), 6752–6756. <https://doi.org/10.1021/jm901241e>.
- (70) Lovering, F. Escape from Flatland 2: Complexity and Promiscuity. *Med. Chem. Commun.* **2013**, *4* (3), 515. <https://doi.org/10.1039/c2md20347b>.
- (71) Lin, Q.; Spielvogel, E. H.; Diao, T. Carbon-Centered Radical Capture at Nickel(II) Complexes: Spectroscopic Evidence, Rates, and Selectivity. *Chem* **2023**, *9* (5), 1295–1308. <https://doi.org/10.1016/j.chempr.2023.02.010>.
- (72) Prieto Kullmer, C. N.; Kautzky, J. A.; Krska, S. W.; Nowak, T.; Dreher, S. D.; MacMillan, D. W. C. Accelerating Reaction Generality and Mechanistic Insight through Additive Mapping. *Science* **2022**, *376* (6592), 532–539. <https://doi.org/10.1126/science.abn1885>.
- (73) Wang, X.; Wang, S.; Xue, W.; Gong, H. Nickel-Catalyzed Reductive Coupling of Aryl Bromides with Tertiary Alkyl Halides. *J. Am. Chem. Soc.* **2015**, *137* (36), 11562–11565. <https://doi.org/10.1021/jacs.5b06255>.
- (74) Kim, Y.; Iwai, T.; Fujii, S.; Ueno, K.; Sawamura, M. Dumbbell-Shaped 2,2'-Bipyridines: Controlled Metal Monochelation and Application to Ni-Catalyzed Cross-Couplings. *Chem. Eur. J.* **2021**, *27* (7), 2289–2293. <https://doi.org/10.1002/chem.202004053>.
- (75) Isbrandt, E. S.; Sullivan, R. J.; Newman, S. G. High Throughput Strategies for the Discovery and Optimization of Catalytic Reactions. *Angew. Chem. Int. Ed.* **2019**, *58* (22), 7180–7191. <https://doi.org/10.1002/anie.201812534>.
- (76) Zhao, S.; Gensch, T.; Murray, B.; Niemeyer, Z. L.; Sigman, M. S.; Biscoe, M. R. Enantiodivergent Pd-Catalyzed C–C Bond Formation Enabled through Ligand Parameterization. *Science* **2018**, *362* (6415), 670–674. <https://doi.org/10.1126/science.aat2299>.
- (77) Dunning, T. H. Gaussian Basis Sets for Use in Correlated Molecular Calculations. I. The Atoms Boron through Neon and Hydrogen. *J. Chem. Phys.* **1989**, *90*, 1007–1023. <https://doi.org/10.1063/1.456153>.
- (78) Qi, Y.-Q.; Liu, S.; Xu, Y.; Li, Y.; Su, T.; Ni, H.-L.; Gao, Y.; Yu, W.; Cao, P.; Hu, P.; Zhao, K.-Q.; Wang, B.-Q.; Chen, B. Nickel-Catalyzed Three-Component Cross-Electrophile Coupling of 1,3-Dienes with Aldehydes and Aryl Bromides. *Org. Lett.* **2022**, *24* (28), 5023–5028. <https://doi.org/10.1021/acs.orglett.2c01648>.
- (79) Janssen-Müller, D.; Sahoo, B.; Sun, S.; Martin, R. Tackling Remote sp^3 C–H Functionalization via Ni-Catalyzed “Chain-walking” Reactions. *Isr. J. Chem.* **2020**, *60* (3–4), 195–206. <https://doi.org/10.1002/ijch.201900072>.
- (80) Truesdell, B. L.; Hamby, T. B.; Sevov, C. S. General $C(sp^2)$ – $C(sp^3)$ Cross-Electrophile Coupling Reactions Enabled by Overcharge Protection of Homogeneous Electrocatalysts. *J. Am. Chem. Soc.* **2020**, *142* (12), 5884–5893. <https://doi.org/10.1021/jacs.0c01475>.
- (81) Yamamoto, T.; Wakabayashi, S.; Osakada, K. Mechanism of C–C Coupling Reactions of Aromatic Halides, Promoted by Ni(COD)₂ in the Presence of 2,2'-

- Bipyridine and PPh₃, to Give Biaryls. *J. Organomet. Chem.* **1992**, 428 (1–2), 223–237. [https://doi.org/10.1016/0022-328X\(92\)83232-7](https://doi.org/10.1016/0022-328X(92)83232-7).
- (82) Piszal, P. E.; Orzolek, B. J.; Olszewski, A. K.; Rotella, M. E.; Spiewak, A. M.; Kozlowski, M. C.; Weix, D. J. Protodemetalation of (Bipyridyl)Ni(II)–Aryl Complexes Shows Evidence for Five-, Six-, and Seven-Membered Cyclic Pathways. *J. Am. Chem. Soc.* **2023**, jacs.3c00618. <https://doi.org/10.1021/jacs.3c00618>.
- (83) Ting, S. I.; Williams, W. L.; Doyle, A. G. Oxidative Addition of Aryl Halides to a Ni(I)-Bipyridine Complex. *J. Am. Chem. Soc.* **2022**, 144 (12), 5575–5582. <https://doi.org/10.1021/jacs.2c00462>.
- (84) Kim, S.; Goldfogel, M. J.; Gilbert, M. M.; Weix, D. J. Nickel-Catalyzed Cross-Electrophile Coupling of Aryl Chlorides with Primary Alkyl Chlorides. *J. Am. Chem. Soc.* **2020**, 142 (22), 9902–9907. <https://doi.org/10.1021/jacs.0c02673>.
- (85) Sakai, H. A.; Liu, W.; Le, C. “Chip”; MacMillan, D. W. C. Cross-Electrophile Coupling of Unactivated Alkyl Chlorides. *J. Am. Chem. Soc.* **2020**, 142 (27), 11691–11697. <https://doi.org/10.1021/jacs.0c04812>.
- (86) Liao, J.; Basch, C. H.; Hoerrner, M. E.; Talley, M. R.; Boscoe, B. P.; Tucker, J. W.; Garnsey, M. R.; Watson, M. P. Deaminative Reductive Cross-Electrophile Couplings of Alkylpyridinium Salts and Aryl Bromides. *Org. Lett.* **2019**, 21 (8), 2941–2946. <https://doi.org/10.1021/acs.orglett.9b01014>.
- (87) Gavryushin, A.; Kofink, C.; Manolikakes, G.; Knochel, P. An Efficient Negishi Cross-Coupling Reaction Catalyzed by Nickel(II) and Diethyl Phosphite. *Tetrahedron* **2006**, 62 (32), 7521–7533. <https://doi.org/10.1016/j.tet.2006.03.123>.
- (88) Buonomo, J. A.; Everson, D. A.; Weix, D. J. Substituted 2,2'-Bipyridines by Nickel Catalysis: 4,4'-Di-Tert-Butyl-2,2'-Bipyridine. *Synthesis* **2013**, 45 (22), 3099–3102. <https://doi.org/10.1055/s-0033-1338520>.
- (89) Hue, R. J.; Vatassery, R.; Mann, K. R.; Gladfelter, W. L. Zinc Oxide Nanocrystal Quenching of Emission from Electron-Rich Ruthenium-Bipyridine Complexes. *Dalton Trans.* **2015**, 44 (10), 4630–4639. <https://doi.org/10.1039/C4DT03272A>.
- (90) Wang, H.-Y.; Tang, J.-W.; Peng, P.; Yan, H.-J.; Zhang, F.-L.; Chen, S.-X. Development of a Novel Chemoenzymatic Process for (S)-1-(Pyridin-4-yl)-1,3-Propanediol. *Org. Process Res. Dev.* **2020**, 24 (12), 2890–2897. <https://doi.org/10.1021/acs.oprd.0c00403>.
- (91) Duric, S.; Tzschucke, C. C. Synthesis of Unsymmetrically Substituted Bipyridines by Palladium-Catalyzed Direct C–H Arylation of Pyridine N -Oxides. *Org. Lett.* **2011**, 13 (9), 2310–2313. <https://doi.org/10.1021/ol200565u>.
- (92) Johnson, K. A.; Biswas, S.; Weix, D. J. Cross-Electrophile Coupling of Vinyl Halides with Alkyl Halides. *Chem. Eur. J.* **2016**, 22 (22), 7399–7402. <https://doi.org/10.1002/chem.201601320>.
- (93) Tcyrulnikov, S.; Cai, Q.; Twitty, J. C.; Xu, J.; Atifi, A.; Bercher, O. P.; Yap, G. P. A.; Rosenthal, J.; Watson, M. P.; Kozlowski, M. C. Dissection of Alkylpyridinium Structures to Understand Deamination Reactions. *ACS Catal.* **2021**, 11 (14), 8456–8466. <https://doi.org/10.1021/acscatal.1c01860>.
- (94) Parr, R. G.; Gadre, S. R.; Bartolotti, L. J. Local Density Functional Theory of Atoms and Molecules. *Proc. Natl. Acad. Sci. U.S.A.* **1979**, 76 (6), 2522–2526. <https://doi.org/10.1073/pnas.76.6.2522>.
- (95) Parr, R. G.; Szentpály, L. V.; Liu, S. Electrophilicity Index. *J. Am. Chem. Soc.* **1999**, 121 (9), 1922–1924. <https://doi.org/10.1021/ja983494x>.

- (96) O'Boyle, N. M.; Banck, M.; James, C. A.; Morley, C.; Vandermeersch, T.; Hutchison, G. R. Open Babel: An Open Chemical Toolbox. *J. Cheminform.* **2011**, *3* (1), 33. <https://doi.org/10.1186/1758-2946-3-33>.
- (97) The Open Babel Package, v. 3.0.0, 2019. <https://github.com/openbabel/openbabel>.
- (98) Guilian Luchini; Patterson, T.; Paton, R. DBSTEP: Release 1.0, 2021. <https://doi.org/10.5281/ZENODO.4702097>.
- (99) Larsen, M. A.; Oeschger, R. J.; Hartwig, J. F. Effect of Ligand Structure on the Electron Density and Activity of Iridium Catalysts for the Borylation of Alkanes. *ACS Catal.* **2020**, *10* (5), 3415–3424. <https://doi.org/10.1021/acscatal.0c00152>.
- (100) Tanaka, T.; Yazaki, R.; Ohshima, T. Chemoselective Catalytic α -Oxidation of Carboxylic Acids: Iron/Alkali Metal Cooperative Redox Active Catalysis. *J. Am. Chem. Soc.* **2020**, *142* (9), 4517–4524. <https://doi.org/10.1021/jacs.0c00727>.
- (101) Qiu, H.; Shuai, B.; Wang, Y.-Z.; Liu, D.; Chen, Y.-G.; Gao, P.-S.; Ma, H.-X.; Chen, S.; Mei, T.-S. Enantioselective Ni-Catalyzed Electrochemical Synthesis of Biaryl Atropisomers. *J. Am. Chem. Soc.* **2020**, *142* (22), 9872–9878. <https://doi.org/10.1021/jacs.9b13117>.
- (102) Zhang, L.; Wang, X.; Pu, M.; Chen, C.; Yang, P.; Wu, Y.-D.; Chi, Y. R.; Zhou, J. S. Nickel-Catalyzed Enantioselective Reductive Arylation and Heteroarylation of Aldimines via an Elementary 1,4-Addition. *J. Am. Chem. Soc.* **2023**, *jacs.3c00548*. <https://doi.org/10.1021/jacs.3c00548>.
- (103) Zhang, L.; Zhao, M.; Pu, M.; Ma, Z.; Zhou, J.; Chen, C.; Wu, Y.-D.; Chi, Y. R.; Zhou, J. S. Nickel-Catalyzed Enantioselective Reductive Conjugate Arylation and Heteroarylation via an Elementary Mechanism of 1,4-Addition. *J. Am. Chem. Soc.* **2022**, *144* (44), 20249–20257. <https://doi.org/10.1021/jacs.2c05678>.
- (104) Wagner, C. L.; Herrera, G.; Lin, Q.; Hu, C. T.; Diao, T. Redox Activity of Pyridine-Oxazoline Ligands in the Stabilization of Low-Valent Organonickel Radical Complexes. *J. Am. Chem. Soc.* **2021**, *143* (14), 5295–5300. <https://doi.org/10.1021/jacs.1c00440>.
- (105) Poremba, K. E.; Dibrell, S. E.; Reisman, S. E. Nickel-Catalyzed Enantioselective Reductive Cross-Coupling Reactions. *ACS Catal.* **2020**, *10* (15), 8237–8246. <https://doi.org/10.1021/acscatal.0c01842>.
- (106) Lachaize, S.; Gallegos, D. C.; Antonio, J. J.; Atesin, A. C.; Atesin, T. A.; Jones, W. D. Ortho-Fluoro Effect on the C–C Bond Activation of Benzonitrile Using Zerovalent Nickel. *Organometallics* **2023**, *42* (15), 2134–2147. <https://doi.org/10.1021/acs.organomet.3c00275>.
- (107) Hansch, Corwin.; Leo, A.; Taft, R. W. A Survey of Hammett Substituent Constants and Resonance and Field Parameters. *Chem. Rev.* **1991**, *91* (2), 165–195. <https://doi.org/10.1021/cr00002a004>.
- (108) Ge, S.; Hartwig, J. F. Nickel-Catalyzed Asymmetric α -Arylation and Heteroarylation of Ketones with Chloroarenes: Effect of Halide on Selectivity, Oxidation State, and Room-Temperature Reactions. *J. Am. Chem. Soc.* **2011**, *133* (41), 16330–16333. <https://doi.org/10.1021/ja2082087>.
- (109) Ge, S.; Green, R. A.; Hartwig, J. F. Controlling First-Row Catalysts: Amination of Aryl and Heteroaryl Chlorides and Bromides with Primary Aliphatic Amines Catalyzed by a BINAP-Ligated Single-Component Ni(0) Complex. *J. Am. Chem. Soc.* **2014**, *136* (4), 1617–1627. <https://doi.org/10.1021/ja411911s>.
- (110) Mills, L. R.; Edjoc, R. K.; Rousseaux, S. A. L. Design of an Electron-Withdrawing Benzonitrile Ligand for Ni-Catalyzed Cross-Coupling Involving Tertiary

- Nucleophiles. *J. Am. Chem. Soc.* **2021**, *143* (27), 10422–10428. <https://doi.org/10.1021/jacs.1c05281>.
- (111) Wang, J.; Eehalt, L. E.; Huang, Z.; Beleh, O. M.; Guzei, I. A.; Weix, D. J. Formation of C(Sp²)-C(Sp³) Bonds Instead of Amide C-N Bonds from Carboxylic Acid and Amine Substrate Pools by Decarbonylative Cross-Electrophile Coupling. *J. Am. Chem. Soc.* **2023**, *145* (18), 9951–9958. <https://doi.org/10.1021/jacs.2c11552>.
- (112) Douthwaite, J. L.; Zhao, R.; Shim, E.; Mahjour, B.; Zimmerman, P. M.; Cernak, T. Formal Cross-Coupling of Amines and Carboxylic Acids to Form Sp³-Sp² Carbon-Carbon Bonds. *J. Am. Chem. Soc.* **2023**, *145* (20), 10930–10937. <https://doi.org/10.1021/jacs.2c11563>.